

NOVEL RECONFIGURABLE DELTA ROBOT
DUAL-FUNCTIONING AS
ADAPTIVE LANDING GEAR AND MANIPULATOR

MORITZ ARNS

A THESIS SUBMITTED TO THE FACULTY OF GRADUATE STUDIES IN PARTIAL
FULFILLMENT OF THE REQUIREMENTS FOR THE DEGREE OF
MASTERS OF APPLIED SCIENCES

GRADUATE PROGRAM IN MECHANICAL ENGINEERING
YORK UNIVERSITY TORONTO, ONTARIO

APRIL 2019

© MORITZ ARNS, 2019

Abstract

In this work a novel dual-functioning rotorcraft undercarriage is developed. The design is a re-configurable delta robot which allows for transformation between Adaptive Landing Gear for vertical take-off and landing and 3DOF Aerial Manipulation mode. To re-configure between operation modes without reaching singularities, a guideline to find a singularity-free geometry is presented. An adaptive landing control was developed and validated on a test-stand. For the 3DOF manipulation of the delta-structure, a third-order smooth trajectory was presented and integrated. The prototype, also depicted in the accompanying video, is then presented in free flight experiments demonstrating the advantages of the dual-functioning system.

Acknowledgment

To my fiancée and my family.

Glossary

ABS Acrylonitrile Butadiene Styrene. 43

ARM Advanced RISC Machines. 67

DARPA Defense Advanced Research Projects Agency. 6

DC Direct Current. 67

DOF Degrees-of-free-dome number of independent parameters that define its configuration. ii

ETH Eidgenössische Technische Hochschule. 6

KUKA Keller und Knappich Augsburg. 89

LIPO lithium polymer battery. 67

MAR Mission adaptive rotor. 6

MBZIRC Mohamed Bin Zayed International Robotics Challenge. 1

NASA National Aeronautics and Space Administration. 5

PCB Printed circuit board. 69

UAV Unmanned aerial vehicle (an aircraft piloted by remote control or onboard computers).. 1

USB Universal Serial Bus. 67

Contents

Abstract	ii
Acknowledgment	iii
Glossary	iv
Contents	v
List of Tables	viii
List of Figures	ix
1 Introduction	1
1.1 Goal of Research	2
1.2 Requirements	2
1.3 Thesis Organization	4
2 Literature Review and Concept	5
2.1 Adaptive Landing Gear	5
2.2 Aerial Manipulation Systems	6
2.3 Concept of Dual-Functioning System	8
3 Mechanical Design	10
3.1 Defining Basic Dimensions - Integration into Rotorcraft Design	10
3.2 Delta Robot Kinematics	11
3.2.1 Forward Kinematics	14
3.2.2 Inverse Kinematics	16
3.2.3 Jacobian Matrices	17
3.2.4 Singularities	19
3.3 Workspace	22
3.3.1 Reduced Total Orientation Workspace	22
3.3.2 Generic Geometry	23
3.3.3 Evaluation of Workspace from Generic Geometry	25
3.4 Singularity free Workspace for Reconfiguration	26
3.4.1 Evaluation of Workspace from Reconfigurable Geometry	28
3.5 Tripod Landing Gear Kinematics	30
3.5.1 Forward Kinematic of Landing Mode	31
3.5.2 Inverse Kinematic of Landing Mode	32
3.5.3 Conclusions Tripod Landing Gear Kinematics	34
3.6 Reconfiguration of Mechanism	36
3.6.1 Compact Flight Mode as Reconfiguration Position	36
3.6.2 Landing Mode	37
3.6.3 Leaving Landing Mode	38
3.6.4 Manipulation Mode	39
3.6.5 Leaving Manipulation Mode	40
3.6.6 Conclusion of Novel Reconfigurable Delta Robot Mechanism	40
3.7 Finite Element Analysis	41

3.7.1	Stress Analysis Manipulation Mode	41
3.7.2	Stress Analysis Landing Mode	42
3.7.3	Conclusion Finite Element Analysis	43
4	Control	44
4.1	Trajectory generation for Manipulation Mode	44
4.1.1	Path Specification	44
4.1.2	Generation of Third-order position trajectory	45
4.1.3	Inverse Kinematics to joint space	51
4.1.4	Conclusion of Trajectory generation for Manipulation Mode	53
4.2	Adaptive Landing	55
4.2.1	Adaptive Landing Sequence	55
4.2.2	Calculation of Landing Angle for Safe Graded Landing	57
4.2.3	Motor Control for Adaptive Landing	58
4.2.4	Reaction Torque on the Rotorcraft during Adaptive Landing	61
4.2.5	Energy absorption during rough landing	65
4.2.6	Conclusion on Adaptive Landing	66
5	Prototype Development and Construction	67
5.1	Electrical Components and Circuit Design	67
5.1.1	Teensey 3.2 microcontroller	67
5.1.2	Dynamixel AX 12A Motor	68
5.1.3	Circuitry design	69
5.2	Mechanical Components	69
5.2.1	Tactile Sensors	70
5.2.2	Prismatic Arms	72
5.2.3	Centre Locking Mechanism	73
5.2.4	Completed design integrated into rotorcraft	75
5.2.5	Functional extension of Prototype	79
5.2.6	Conclusion Extension of System	81
6	Platform Evaluation	82
6.1	Interaction Forces during Adaptive Landing	82
6.1.1	Conclusion Adaptive Landing Control on test-stand	85
6.2	Free Flight Experiments	86
6.3	Conclusion of Free Flight Experiments	87
6.4	Comprehensive comparison of State-of-the-Art Systems and Manipulander	89
6.4.1	Aerial Manipulators	89
6.4.2	Adaptive Landing Gears	92
6.4.3	Conclusion of Comprehensive Comparison	93
7	Application	95
7.1	Search and Rescue	95
7.2	Military and Law Enforcement	96
7.3	Mining	97
7.4	Space	98
7.5	Delivery	98

8 Conclusion	100
8.1 Research Contributions:	101
9 Future Work	103
9.1 Reliability	103
9.2 Dynamic Control of Manipulation Mode	103
9.3 Development of a standard Adaptive Landing Control benchmark	103
9.4 Dynamic control of Adaptive Landing	104
9.5 Weight optimization and scaling	105
References	106
A Appendices	114
A.1 Schematics of Circuitry	114
A.2 QR code to video demo of free-flight experiments	115

List of Tables

1	Requirements overview	3
2	Dimensions of generic, non optimized geometry	23
3	Dimensions of Manipulander depending on rotorcraft geometry. Length a is retracted.	28
4	Basic dimensions of Landing Gear configuration - Centroid P of moving platform is mechanically locked 80 mm centrally below the Base platform. Shown in Figure 11 .	34

List of Figures

1	DJI Matrice 100 dimensions of Mainbody ($m = 210$ mm) and Rotorcraft Wheelbase ($w = 650$ mm). (from[1])	10
2	Manipulander dimensions in relation to Rotorcraft.	11
3	3D visualization of Delta Concept.	12
4	Detailed description of joints and angles. (Similar in [2])	13
5	Line symmetric schematic of geometry for forward kinematics.	15
6	Delta robot with non-optimized geometry.	24
7	Tripod reconfiguration during flight & adaption to uneven surfaces for landing.	24
8	Reduced Total Orientation Workspace calculations with non-optimized geometry ($a = b$).	26
9	Line symmetric schematic of optimization of geometry. (left with singularity, right without singularity)	27
10	Optimized continuous workspace with $b = 300$; $b > b^*$	29
11	Line symmetric illustration of kinematics when reconfigured to Landing Mode.	31
12	Reconfiguration of Mechanism between Manipulator and Landing Gear.	36
13	Compact Flight Mode for energy saving and reconfiguration of mechanism.	37
14	Flowchart describing the conversion to Landing Mode	38
15	Adaptation to uneven surfaces in Tripod Landing Configuration.	38
16	Manipulation Mode as Delta Mechanism allowing 3DOF.	39
17	Von Mises Stress Analysis of Mechanism in Manipulation mode.	42
18	Von Mises Stress Analysis of Mechanism in Landing mode.	43
19	Flow chart of trajectory generation.	45
20	Manipulander performing point to point trajectory from point A to B.	46
21	Angles of actuators during trajectory from point A to B.	48
22	Illustration of array s which holds the segment length of each step.	49
23	Comparison of the segment length to moving platform velocity and acceleration between point A and B.	50
24	Illustrating trajectory generation with unit vector and step length s(i) along the path.	51
25	Angles of actuators during trajectory from point A to B with added positions at beginning and end.	53
26	Angular velocity of actuators during trajectory from point A to B. Beginning and end shows unsteady behaviour due to the manipulation of the angle array.	54
27	Angular acceleration of actuators during trajectory from point A to B.	55
28	Flowchart describing the Safe Guarded Landing sequence.	56
29	Determination of Surface plane and Landing Angle α	57
30	Motor Control for Self-leveled Landing.	59
31	Torque limit calculations. Landing leg in the position which provides the smallest force at B_i	60
32	Resulting forces on rotorcraft during touchdown of the first two landing legs.	62
33	Torques on rotorcraft platform during adaptive landing. On the left side is a spatial overview of the motors on the platform while the right side shows the torque-vector summation.	63
34	Electrical Hardware Architecture and Bus interfaces.	68
35	Electric circuitry on PCB Board	69
36	3D rendering of PCB board	70
37	Tactile overview	71

38	Tactile before and after landing	72
39	Locking mechanism of Prismatic legs	72
40	Centre locking mechanism to secure moving platform in Compact mode.	74
41	Mechanism in Compact flight mode transporting package.	75
42	Mechanism in Manipulation mode picking up package.	76
43	Landing on even ground with cargo attached to moving platform.	77
44	Mechanism landing on uneven ground.	78
45	Functional extension allows to use cable and winch for transforming the mechanism to pick up and deliver cargo without landing.	79
46	Detailed view of probe deploy and locking mechanism.	80
47	Manipulander attached to Forklift, illustrating setup for Trail 3 with two different heights.	83
48	Experimental Results of Direction of Torque on Platform and Total Torque on Platform during four different landing trails.	84
49	Experimental Results of Force in Z-Axis on Platform and Direction of Torque on Platform during four different landing trails.	85
50	Prototype demonstrating different operation modes	87
51	Comparison between different aerial manipulation solutions.	90
52	Comparison between different adaptive landing gear solutions.	93
53	Manipulander providing medical kit to insured hiker.	96
54	Sleeping drone collecting surveillance information, and disarming suspicious objects.	97
55	Manipulander deploys sensor elements in mining pit, and can land for change of equipment in the mining field.	97
56	Artist's conception of the autonomous, drone-like Mars Helicopter, which will be sent to Mars along with the 2020 rover. (from [3])	98
57	Mock image illustrating Manipulander in fictional Mars mission. (changed from [4])	99
58	Manipulander delivers package to the doorstep.	99
59	Electrical Hardware Architecture and Bus interfaces.	114
60	QR code to address of free-flight demo video "Delta Manipulander - 3DOF Manipulation and Adaptive Landing in One System" : https://youtu.be/aWPeTaXtEIE . .	115

1 Introduction

Human beings have always dreamt about flying. Since it became a reality over a century ago, people have been developing new and diverse flight machines. These machines can be broadly categorized into rotorcrafts and fixed-wing aircraft: the helicopter and airplane respectively being the best known. Rotorcrafts can hover as well as take-off and land vertically, which allows them to operate and land in narrow spaces. One of the most serious disadvantages of the vertical takeoff and landing of rotorcrafts is the requirement of a flat area for safe landing. Organisations such as Militaries, Search and Rescue, and Logistics have recently shown an interest in using rotorcrafts in more diverse landscapes including natural-disaster zones or rural areas where landing is challenging, or prepared landing sites are time consuming to locate [5]. Extremely high safety standards in manned rotorcrafts prevented the inherently complex adaptive landing gears from being adopted. Nowadays, however, this technology can be employed in unmanned aircrafts (UAVs) since they allow for higher risk-taking [6]. The functionality of adaptive landing gears is a proven concept and can at least be dated back at least into the 70s when a modification of an air/oil strut landing gear for helicopters was patented which allows the rotorcraft to land on a slope [7]. Even today, the inefficient hovering of rotorcraft makes the increase in weight of an actuated landing gear a challenge for the mostly battery powered unmanned vertical lander [8]. In contrast to the landing gear where simple light weight options are primarily adopted, added weight and complexity are essential to a different field of UAV research. Research in aerial manipulation tries to manipulate objects from a flying platform but this requires the rotorcraft to lift the inherently heavy and complex robotic arm. Nonetheless, some researchers see that the use of aerial manipulators is just the natural next step for ground-bound robots [9] enabling applications like inspection, delivery, construction, maintenance, and even flying additive manufacturing [10]. A big financial supporter is the MBZIRC competition [11] which has twice awarded a five million dollar prize for the best unmanned aerial vehicle (UAV) to perform in a

variety of scenarios with physical interaction such as aerial manipulations. Fueled by the increased commercial interest, this paper develops a novel dual-functioning system on the base of the delta robot platform by utilizing the existing components of adaptive landing gears and extending them for 3DOF manipulation functions. The new system would offer a better feature-to-complexity ratio, making it a competitive system for a new range of applications.

1.1 Goal of Research

The goal is to design a dual-functioning landing gear system that will increase the usability without substantially increased weight and complexity compared to exclusive Adaptive Landing Gear Systems. The system needs to combine the functions of an adaptive landing gear and a 3DOF Manipulator while being able to be integrated into an existing rotorcraft. The design should be derived from the delta-robot structure, facilitating its excellent capabilities for aerial manipulation.

1.2 Requirements

This section describes the objective of this project. For a successful design process, it is necessary to describe the scope and requirements of the system. The desired system will meet all conditions shown in Table 1 integrated into a novel dual-functioning system based on a delta robot. Table presents the requirements for the Manipulator and the Adaptive Landing Gear separately. The primary function of the system is to find a dual-functioning system that can reconfigure itself between adaptive landing gear and robotic manipulator. As a base requirement the system should be derived from the delta-robot structure. Overall should the design be integrated into the DJI Matrice 100 UAV design which is limiting weight and spatial dimensions. As mentioned in the introduction, in order to be a competitive solution, the design should not increase its complexity compared to common adaptive landing gear solutions. A very common requirement in aeronautics

Requirements	
Overall:	
<i>Primary</i>	
Mechanism based on Delta-robot structure	✓
Reconfiguration between Adaptive Landing Gear & Manipulator	✓
Integrated into DJI Matrice 100 UAV	✓
<i>Secondary</i>	
Simplistic and robust design	✓
Low energy consumption	✓
Use in Indoor environment	✓
Manipulator:	
<i>Primary</i>	
3DOF X,Y,Z Cartesian coordinate system	✓
<i>Secondary</i>	
Fast and precise	✓
Low moving masses	✓
Adaptive Landing Gear:	
<i>Primary</i>	
Retractable Landing Gear	✓
Adaptive Landing Gear	✓
<i>Secondary</i>	
Warning of unsafe landing	✓
No energy consumption when landed	✓

Table 1: Requirements overview

is the low energy consumption since the battery capacity is always a crucial factor. Further it should be mentioned that the system will be designed for the pure indoor use, so external influences such as wind or rain are excluded from this investigation. The Manipulator should have as a primary requirement 3DOF in the X, Y, Z -Cartesian coordinate system. As secondary requirement for the manipulation are fast and precise actuation of the robotic manipulator which will allow for a great range of application. Also, low moving masses are crucial to keep the rotorcraft stable during motions of the moving platform and will increase the precision of the system while reducing the energy consumption. The Adaptive Landing Gear should be primarily be able to be retracted allowing for better aerodynamic performance. As a secondary requirement the robotic landing gear is supposed to adopt to uneven surfaces, which will enable it to operate in rough terrains. Furthermore, when the landing surface is too steep the system should be able to detect this situation

and stop the landing sequence. When landed the mechanism should be able to self-lock disabling all active components on the mechanism stopping the system to drain power from the battery.

1.3 Thesis Organization

The remaining of this thesis is organized as follows. Chapter 2 reviews background of Adaptive Landing Gears, Aerial Manipulation Systems and Re-configurable mechanism. Then it will introduce the Concept of the developed mechanism. Chapter 3 presents the Mechanical Design starting with the general constraints based on the rotorcraft's dimensions. This includes a mechanical investigation of the delta robot's kinematics and workspace. Further introducing the reconfiguration of the mechanism and proving the structural integrity with a Finite Element Analysis. Chapter 4 outlines the control of the Manipulation mode and the Self-Leveled Landing. While focusing on the reaction torque on the rotorcraft and the ability to convert impact energy into electric energy. In Chapter 5 the construction and the development process are outlined. Electric and mechanical components are described in detail. Chapter 6 shows experiments on the build prototype. Measurements on the Interaction forces during adaptive landing are presented. Further a comprehensive comparison to existing of Aerial Manipulators and Adaptive Landing gears systems is given. A fully functioning prototype tested in free flight experiments where it demonstrates all operation modes. In Chapter 7 are possible applications for the mechanism presented. The last Chapter summarizes the outcomes and presents possible directions of future work.

2 Literature Review and Concept

Since this work is designing a new concept of fusing Adaptive Landing Gears with Aerial Manipulators, the Literature review is split in two sections. At first the history of landing gears is explained and current research in building Adaptive Landing Gears is discussed and evaluated. The next section discusses different approaches of aerial manipulations and explains the concept of how a dual-functioning system is created.

2.1 Adaptive Landing Gear

For landing, conventional rotorcrafts use simple skids or fixed wheel designs as landing gear. For better aerodynamics, engineers have further enhanced those mechanisms by adding retractable landing gears. The ability to conceal the landing apparatus first appeared in racing air-crafts in the 1920s [12] and was 1965 adopted to rotorcrafts and first seen in the Bell 209 prototype helicopter. However, these machines are limited by the fact that they require a level plane to take off and land. To protect the rotorcrafts from static or dynamic rollover, research focuses on adaptive landing gears. In 1977 a modification of an air/oil strut landing gear for helicopters was patented which allows to land on a slope [7]. The system requires only simple changes to the landing gear but was to the knowledge of the author never deployed on a rotorcraft. Later in 1990 as mentioned in the Introduction 1 a tripod landing gear was proposed to do coring exploration on the moon. Since we all know that to the current date there has been no coring exploration on moon, this concept may hold potential to get recycled for a new system used in modern rotorcraft systems. In 2010 the interested of the military turned towards adaptive landing gears to stabilize its ducted fan hovercrafts and field a patent which uses a lightweight spring loaded vertical legs [13]. Another passive adaptive landing gear was presented by NASA in [14] which would allow lunar modules to land on slopes of up to 12°. When DARPA then funded a grant to develop an adaptive landing

gear MAR in 2013 research on Adaptive landing gear got more active. The result was a four legged robotic landing gear that is able to land on uneven surfaces and retract its legs as retractable landing gear [15]. In [16] a dynamic model was presented to control an adaptive landing gear depending on different landing condition which can be easily adopted for different systems. Another research built a functioning model of a “DroneGear” which allows to compensate for uneven surfaces using an optical torque sensor which also protects the multirotor from rollover and allows to absorb impact energy [17] which is similar to the results shown in the previously presented DARPA mechanism [18]. Another recent patent [19] shows a mechanism used to allow UAV to land on house roofs allowing for surveillance missions. Not just the military has shown interest in these mechanism Amazon has filed a patent for its package delivery system that could allow their rotorcraft to deliver packages even on uneven surfaces [20]. And University ETH Zurich has built in 2017 an almost full sized helicopter with adaptive landing gear for search and rescue missions in the mountains [21],[22]. The presented research progress and the higher frequency of publications in the recent years clearly shows, that there is an emerging interested in operating rotorcrafts as well as space probes in areas without per-paired landing sites.

2.2 Aerial Manipulation Systems

In this paragraph we talk about different approaches to manipulate objects form a rotorcraft. The ability to perform object manipulations from a flight vehicle enables a range of applications for rotorcrafts and research has already investigated in this area. A comprehensive overview of the systems is given in [23]. The report shows that between 2008 to September 2017, outlining an increasing interest in this technology. Similar to ground bound robots the robotic mechanism used for aerial manipulation can be generally categorized into parallel and serial robots.

Serial Mechanism:

Serial robots have an open kinematic chain where the actuators are on the joints forming a series of articulated linkages where the end forms the robot end-effector. A first example where one of this classic robotic mechanism was fitted to a UAV was in 2013 shown in [24] where a two-DOF robotic arm was mounted below a rotorcraft. An adaptive sliding mode controller was designed and showed promising results in order to conduct autonomous pick up of objects. In [25] was a similar two-DOF mechanism used but uses an Integral Backstepping controller which outperforms the common PID controller in aerial manipulation applications. A 7-DOF serial robotic arm was fitted to a rotorcraft which demonstrated a great range of motion. However, due to the fact that the serial manipulators protruded from the rotorcrafts, the considerable change of centre of gravity interfered with the rotorcraft's flight [26]. Another interesting approach is shown in [27] where a serial arm was fitted under the rotorcraft which would allow to grasp larger objects. A similar approach takes this idea even further and uses a dual serial arm as gripper but also uses it as a landing gear where the rotorcraft perches bird like onto a cylindrical object like a pipe or branch [28]. To reach objects in great depth [29] presents an origami inspired robotic arm to reach very far straight below the UAV. The opposite approach is taken in [30] where the gripper is fitted right onto the lower side of the rotorcraft to minimize dynamic load disturbances. Also, interesting approach was taken in [31] where a hybrid system composed of drone and snake robot was created. Two snake robots are integrated into the rotorcraft and the tails of the snakes are used as four contact points of the landing gear. When landed the snakes are disconnected from the rotorcraft and operate independently.

Parallel Mechanism:

A parallel robot is not as frequently seen in the application of aerial manipulating even-though their structure holds potential advantages for this field. A parallel manipulator can be defined as a closed-loop mechanism composed of an end-effector having n degrees of freedom and a fixed base,

linked together by at least two independent kinematic chains [32]. This allows for high accuracy and actuation speed but generally reduces the workspace compared to serial arm robots. A three-DOF planar parallel mechanism was attached to a drone in [33] to perform light inspections. It has a large workspace horizontally extending in-front of the rotorcraft. The parallel design allows for high dexterity and maximum singularity-free workspace. A classic parallel mechanism are the delta robots attached to UAVs shown in [34] and [35]. The classic parallel kinematics allows for fast and precise three-DOF which is demonstrated with a feedforward control. In [36] was a "H-Delta" a novel five-DOF delta derivative attached to a rotorcraft. A six-DOF parallel mechanism was shown on a rotorcraft in [37] which allowed to stabilize the endeffector during crosswinds in a predefined position. This mechanism also folds the mechanism upwards much like a retractable landing gear for better flight capabilities. An application for aerial manipulation is shown by a company [38] where they use a delta robot on a rotorcraft to disarm landmines. In normal ground bound applications, the less frequent use of parallel robots can be concluded to: "...parallel robots offer potential advantages compared with serial, with higher overall stiffness, higher precision, low inertia, and higher operating speeds and accelerations. However, these advantages could be easily relativized by reduced workspace, difficult mechanical design, and more complex kinematics and control algorithms." [39] Deployed on a rotorcraft, parallel manipulators can compensate for their small workspace and suddenly become an attractive system for aerial applications. Utilizing their lower moving masses, higher precision and end-effector bandwidth, makes them, in the authors' view, a better fit for aerial manipulations compared to serial manipulators.

2.3 Concept of Dual-Functioning System

After review of the literature and previous works a new concept is presented that combines landing gear and aerial manipulation. For the adaptive landing gear, it was required to be retractable while

having an overall robust and simplistic design. The new landing gear is inspired by the tripod landing gear from NASA for lunar coring explorations. It has a tripod geometry which convinces with its simple but functional structure. For the aerial manipulations a general best suited system seems to have not been found yet. Researcher use serial as well as parallel mechanism for equal tasks. But the analysis of the literature review shows that parallel mechanism seems to be better suited for this application. Their key advantages of high-performance manipulation while reduced disruption of the flight performance of the rotor-craft give parallel structures a general advantage over serial structures since the rotorcraft can compensate their limited workspace. Therefore, this research will advocate for the implementation of delta structures in aerial manipulation which hopefully helps parallel-structures to more popularity in aeronautics. Hence, a dual-functioning system that can operate as adaptive landing gear and aerial manipulator in form of a novel re-configurable delta robot was designed. The base of inspiration was a tripod landing gear and a delta-robot manipulator. The three arms of the delta robot will be transformed into landing legs creating a re-configurable mechanism which can switch between manipulation and adaptive landing gear. Researcher have already developed re-configurable delta mechanism to adjust workspace and payload-capacity [40], but no work has been found to reconfigure it into a landing gear structure or similar. This novel dual-functioning system has the advantage of giving the flight vehicle an increase in flexibility by combining a tripod landing gear and a delta robot. Unlike the previous systems, the reconfiguration of a delta robot allows for the efficient integration of both functions (Landing Gear and Aerial Manipulation) in one system while keeping the overall weight low. In the following this re-configurable system is referred to as "Manipulander" which is a portmanteau for Manipulator and Landing Gear.

3 Mechanical Design

3.1 Defining Basic Dimensions - Integration into Rotorcraft Design

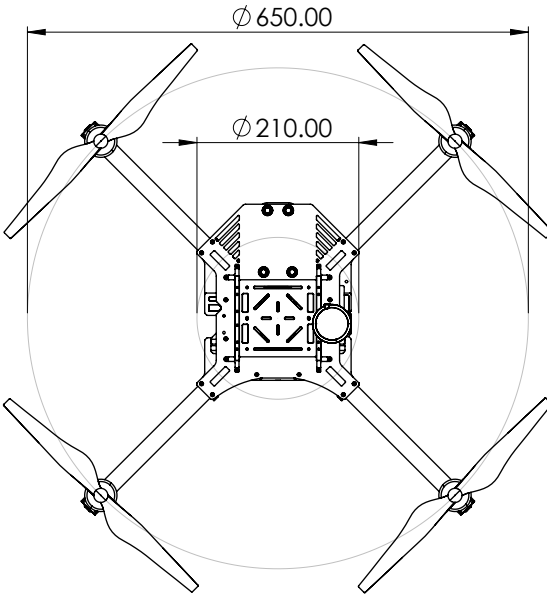


Figure 1: DJI Matrice 100 dimensions of Mainbody ($m = 210$ mm) and Rotorcraft Wheelbase ($w = 650$ mm). (from[1])

To find the optimum design of the Manipulander dimensions it is essential to consider the integration of the Manipulander into the rotorcraft. In this example we are considering a UAV rotorcraft from DJI, a popular drone manufacturer. The DJI Matrice 100 is a typical example of a quadcopter shown in Figure 1. The total weight of UAV is 2431 g where it can carry payloads of up to 1200 g. It consists out of a main body which hosts energy control and communication and four rotor blades which are equally distributed around the main body to generate thrust. The Manipulander replaces the position of the standard landing gear central below the rotorcrafts main body. To find the best dimensions for the Manipulander one must consider the main objectives of a rotorcraft. The Manipulander should be compact, nor should it add too much weight to the system. On the other side allows a bigger Manipulander for a greater workspace and better landing capabilities. In the following we introduce some design guidelines on how to incorporate the Manipulander design into

a generic rotorcraft. These design guidelines are then presented at the example of the DJI Matrice 100 rotorcraft. Figure 2 shows a schematic illustration of the integration of a Manipulander with a rotorcraft. The base platform of the Manipulander is chosen to be the same diameter r as the main body of the rotorcraft. This allows for the most stable attachment to the rotorcraft design. The length of limb a of the rotorcraft is defined by the wheelbase of the rotorcraft. When the first limb a is in complete horizontal position ($\theta_{1i} = 0^\circ$) it should not reach outside of the rotorcraft wheelbase. This ensures that the flight vehicle is still compact during flight while allowing for best landing and manipulation performance. Those relatively simple considerations allow to define length r & a of the Manipulander platform.

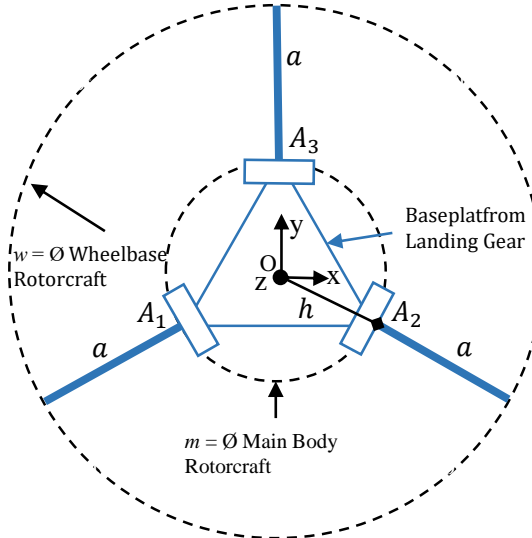


Figure 2: Manipulander dimensions in relation to Rotorcraft.

3.2 Delta Robot Kinematics

In this section a schematic illustration is used to analyze the kinematics of the 3-DOF delta mechanism which is in this research used for manipulation and later reconfiguration into a landing gear system. The moving platform can only perform three transnational motions in x y and z. Illustration 3 below shows the geometric configuration of the delta mechanism. The two main components

are the Base Platform and the Moving Platform. The Base Platform would later be attached to the bottom of the rotor-craft and is the reference frame of the coordinate system O . For manipulation the delta mechanism has three actuated joints at A_i which are equally distributed over the plane by the constant parameter ϕ_i . It is worth mentioning that different actuation joints are possible but this configuration allows to hold all actuators close to the rotor-craft which enables better flight performance as described in section 2.3. The actuated joint A_i then nests a second coordinate system x_i, y_i, z_i which is shifted from O by \overline{OA} . For convenient calculation the orientation of the $z_i - axis$ is parallel to the $z - axis$, and $y_i - axis$ is parallel to the revolving joint axis at A_i accommodating Θ_{1i} .

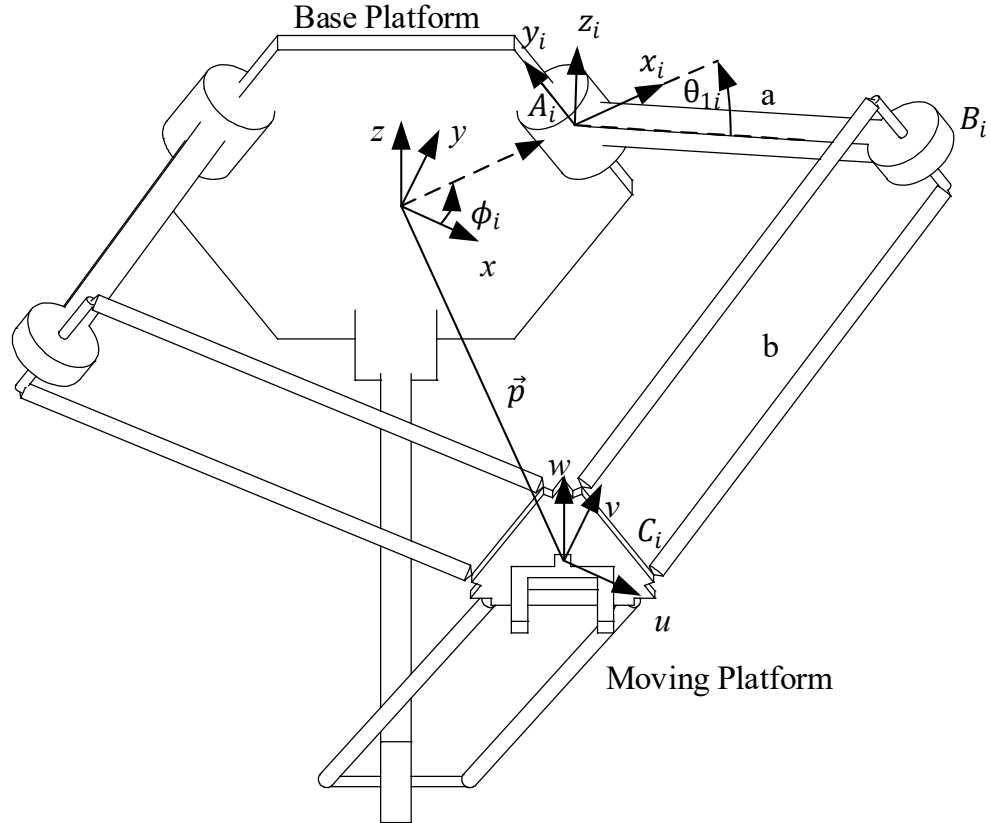


Figure 3: 3D visualization of Delta Concept.

The connection from B_i to C_i is formed by a parallel four bar mechanism which contains four ball joints. It forms the angles Θ_{2i} & Θ_{3i} shown in Figure 4. The length of the mechanism can be

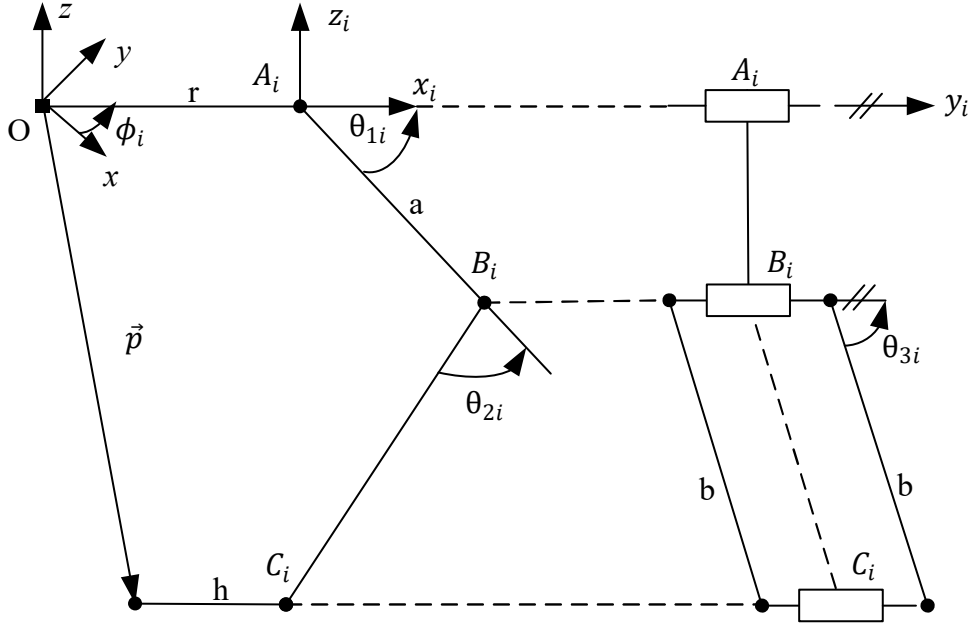


Figure 4: Detailed description of joints and angles. (Similar in [2])

described as r which is the distance to the centroid and can be seen as \overline{OA} as well as \overline{AB} which describes the length of the first leg a . \overline{BC} is the length of the four bar mechanism b . The point C connects to the centroid of the moving platform over the length h . The centroid of the moving platform is described by the position vector \vec{p} . For further investigation of the mechanism the loop-closure equation for each limb is:

$$\overline{A_iB_i} + \overline{B_iC_i} = \overline{OP} + \overline{PC_i} - \overline{OA_i} \quad (1)$$

$$a \begin{bmatrix} c\Theta_{1i} \\ 0 \\ s\Theta_{1i} \end{bmatrix} + b \begin{bmatrix} s\Theta_{3i}c(\Theta_{1i} + \Theta_{2i}) \\ c\Theta_{3i} \\ s\Theta_{3i}s(\Theta_{1i} + \Theta_{2i}) \end{bmatrix} = \begin{bmatrix} C_{xi} \\ C_{yi} \\ C_{zi} \end{bmatrix} \quad (2)$$

$$\begin{bmatrix} C_{xi} \\ C_{yi} \\ C_{zi} \end{bmatrix} = \begin{bmatrix} c\phi_i & s\phi_i & 0 \\ -s\phi_i & c\phi_i & 0 \\ 0 & 0 & 1 \end{bmatrix} \begin{bmatrix} p_x \\ p_y \\ p_z \end{bmatrix} + \begin{bmatrix} h - r \\ 0 \\ 0 \end{bmatrix} \quad (3)$$

To compute the workspace of a mechanism it is necessary to solve the inverse kinematics. The delta concept is a well-studied mechanism and a solution for inverse kinematics is found in [2].

3.2.1 Forward Kinematics

For the calculation of the position of the centroid P of the moving platform, in the cartesian coordinate system (x, y, z) , depending on the actuation angles $\theta_{1i}, \theta_{2i}, \theta_{3i}$, it is required to solve the problem of the forward kinematics. Due to the pure translational nature of the 3DOF mechanism the moving platform is always planar. We consider a virtual point K_i which is on a parallel plane to the moving platform and is shifted by length h from point B_i . Hence, limb b can be virtually shifted to the centroid and connects to P . Introducing spheres nesting at K_i with the radius of limb length b it is possible to determine the position of the moving platform depending on the actuation angles. The intersection points of the spheres represent the possible platform position. The open loop vector equation 4 is used to determine the position of K_i in the original coordinate system. The intersection points of the three spheres are calculated from the spherical equations 6.

$$K_i = \overline{OA_i} + \overline{A_iB_i} + \overline{B_iK_i} \quad (4)$$

$$\begin{bmatrix} K_{xi} \\ K_{yi} \\ K_{zi} \end{bmatrix} = \begin{bmatrix} -c\phi_i & s\phi_i & 0 \\ -s\phi_i & -c\phi_i & 0 \\ 0 & 0 & 1 \end{bmatrix} \cdot \left\{ r \begin{bmatrix} 1 \\ 0 \\ 0 \end{bmatrix} + a \begin{bmatrix} \cos(\theta_{1i}) \\ 0 \\ -\sin(\theta_{1i}) \end{bmatrix} + h \begin{bmatrix} -1 \\ 0 \\ 0 \end{bmatrix} \right\} \quad (5)$$

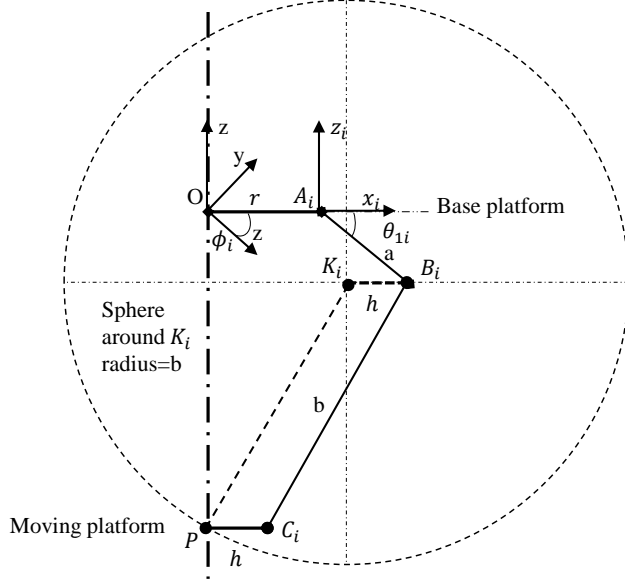


Figure 5: Line symmetric schematic of geometry for forward kinematics.

The analytic equation $(x - x_1)^2 + (y - y_1)^2 + (z - z_1)^2 = r^2$ describes a sphere with center (x_1, y_1, z_1) and radius r . Three sphere equations are introduced nesting at K_i and radius b shown in equation 6. Solving the non-linear equation system for P results three different scenarios. No solution when the platform is out of reach. One solution if there is only one possible configuration for the mechanism. Or two solutions when two different configurations for the mechanism exist. For the last case it is necessary to consider a known initial position of the mechanism to determine which of the configuration is possible at this instance.

$$\begin{aligned}
 (P_x - K_{x1})^2 + (P_y - K_{y1})^2 + (P_z - K_{z1})^2 &= b^2 \\
 (P_x - K_{x1})^2 + (P_y - K_{y2})^2 + (P_z - K_{z2})^2 &= b^2 \\
 (P_x - K_{x1})^2 + (P_y - K_{y3})^2 + (P_z - K_{z3})^2 &= b^2
 \end{aligned} \tag{6}$$

3.2.2 Inverse Kinematics

The Inverse Kinematics describes the relation of the moving platform position \vec{p} in relation to the joint angles of the motors at the base platform. This description is later used to realize a position control of the moving platform. The input is the desired goal position \vec{p} of the moving platform while the output is the angle position for the active joints Θ_{1i} . This allows an easy position control of the mechanism as well as workspace analysis, which are described in the next section. To isolate Θ_{1i} we leave only one term on the left side of 2 and squaring all components in the matrix.

$$\begin{bmatrix} b^2 s^2 \Theta_{3i} c^2 (\Theta_{1i} + \Theta_{2i}) \\ b^2 c^2 \Theta_{3i} c \\ b^2 s \Theta_{3i} s^2 (\Theta_{1i} + \Theta_{2i}) \end{bmatrix} = \begin{bmatrix} (C_{xi0} - ac\Theta_{1i})^2 \\ C_{yi}^2 \\ (C_{zi} - as\Theta_{1i})^2 \end{bmatrix} \quad (7)$$

When subtracting row 1 from row 3 it is now possible to eliminate part of the equation due to the Trigonometric Identities $\sin^2 + \cos^2 = 1$. Resulting in the following equations.

$$\begin{bmatrix} b^2 s^2 \Theta_{3i} c^2 (\Theta_{1i} + \Theta_{2i}) \\ b^2 c^2 \Theta_{3i} c \\ b^2 s^2 \Theta_{3i} \cdot (s^2(\Theta_{1i} + \Theta_{2i}) + c^2(\Theta_{1i} + \Theta_{2i})) \end{bmatrix} = \begin{bmatrix} (C_{xi0} - ac\Theta_{1i})^2 \\ C_{yi}^2 \\ (C_{zi} - as\Theta_{1i})^2 \end{bmatrix} \quad (8)$$

Subtracting now row 2 from row 3 in 8 leaves us with an expression only depending on the variable Θ_{1i} .

$$b^2 = (C_{xi} - ac\theta_{1i})^2 + (C_{zi} - as\theta_{1i})^2 + C_{yi}^2 \quad (9)$$

Due to the complex \sin and \cos expressions in the equation a control in real time with this expression

is not possible. Therefore, the equation was further simplified using the Weierstrass substitutions.

$$\sin(\theta) = \frac{2t}{1+t^2} \quad (10)$$

$$\cos(\theta) = \frac{1-t^2}{1+t^2} \quad (11)$$

This results in the following expression which can be executed in real time with low processing power.

$$b^2 = (C_{xi} - a \cdot \frac{1-t^2}{1+t^2})^2 + (C_{zi} - a \cdot \frac{2t}{1+t^2})^2 + C_{yi}^2 \quad (12)$$

3.2.3 Jacobian Matrices

For the analysis of the mechanism it is necessary to derive a connection between the angular speed of the actuators and the resulting velocities of the moving platform. This is done by deriving the close-loop equation with respect to time [41]. Therefore, the close loop equation 3.2 is rewritten in vector components. Since the delta robot is extensively studied robot those derivation have been already shown in [42].

$$\vec{p} + \vec{r}_i = \vec{h}_i + \vec{a}_i + \vec{b}_i \quad (13)$$

Differentiating this equation with respect to time will give us the Jacobin equation. To simplify the equation we consider that the velocity of any point at the base platform as well as the moving platform is the same. Therefore, we can derive the expression of the velocity of the moving platform as:

$$\begin{aligned} \dot{\vec{r}}_i &= 0 \\ \dot{\vec{h}}_i &= 0 \\ \dot{\vec{p}} &= \vec{v} = \dot{\vec{a}}_i + \dot{\vec{b}}_i \end{aligned} \quad (14)$$

Now $\dot{\vec{a}_i}$ & $\dot{\vec{b}_i}$ can be rewritten in form of angular velocities. Which allow then to make the equation only depending on ω_{ai} .

$$\vec{v} = \omega_{ai} \times \vec{a}_i + \omega_{bi} \times \vec{b}_i \quad (15)$$

$$\vec{v} = \omega_{ai} \times \vec{a}_i + \omega_{bi} \times \vec{b}_i \quad (16)$$

We need to get rid of the dependency of ω_{bi} since it is would mean dependency of θ_{2i} and θ_{3i} . Therefore we multiply everything with \hat{b}_i and obtain a triple product with identical vectors.

$$\hat{b}_i \cdot [\vec{v} = \omega_{ai} \times \vec{a}_i + \omega_{bi} \times \vec{b}_i] \quad (17)$$

$$\hat{b}_i \cdot \vec{v} = \hat{b}_i \cdot \omega_{ai} \times \vec{a}_i \quad (18)$$

This results to the compound form of:

$$\begin{aligned} \hat{b}_i \cdot \vec{v} &= [s\Theta_{3i}c(\Theta_{1i} + \Theta_{2i})] [v_x c\phi_i + v_y s\phi_i] \\ &+ c\Theta_{3i} [-v_x s\phi_i + v_y c\phi_i] \\ &+ [s\Theta_{3i}s(\Theta_{1i} + \Theta_{2i})] v_z = J_{ix}v_x + J_{iy}v_y + J_{iz}v_y \end{aligned} \quad (19)$$

And this can be written as:

$$\begin{bmatrix} J_{ix} \\ J_{iy} \\ J_{iz} \end{bmatrix} = \begin{bmatrix} s\Theta_{3i}c(\Theta_{1i} + \Theta_{2i})c\phi_i - c\Theta_{3i}s\phi_i \\ s\Theta_{3i}c(\Theta_{1i} + \Theta_{2i})s\phi_i + c\Theta_{3i}c\phi_i \\ s\Theta_{3i}s(\Theta_{1i} + \Theta_{2i}) \end{bmatrix} \quad (20)$$

And the Jacobin J_p can be written as:

$$J_p = \begin{bmatrix} J_{1x} & J_{1y} & J_{1z} \\ J_{2x} & J_{2y} & J_{2z} \\ J_{3x} & J_{3y} & J_{3z} \end{bmatrix} \quad (21)$$

The calculations on the right hand side of equation 18 are as follows. Since $\vec{\omega}_{ai}$ describes the angular velocity around the resolute joint at the coordinate system it can be simply written as $\dot{\Theta}_{1i}$ about the x_i axis.

$$\vec{\omega}_{ai} \times \vec{a}_i = \begin{bmatrix} a_{zi}\dot{\theta}_{1i} \\ 0 \\ -a_{xi}\dot{\theta}_{1i} \end{bmatrix} \quad (22)$$

$$\hat{b}_i \cdot (\vec{\omega}_{ai} \times \vec{a}_i) = as\theta_{2i}s\theta_{3i}\dot{\theta}_{1i} \quad (23)$$

So the so J_θ can be written as:

$$J_\theta = a \cdot \begin{bmatrix} s\theta_{2i}s\theta_{3i} & 0 & 0 \\ 0 & s\theta_{2i}s\theta_{3i} & 0 \\ 0 & 0 & s\theta_{2i}s\theta_{3i} \end{bmatrix} \quad (24)$$

The complete solution can be written as:

$$J_p \vec{v} = J_\theta \dot{\vec{\theta}} \quad (25)$$

3.2.4 Singularities

Form the Jacobi matrices which relate the input speeds with the output speeds we can obtain singular positions of the mechanism. These positions occur when the Jacobi matrices becomes rank

defection. These are usually unwanted configurations since the mechanism losses degrees of freedom. In order to find those positions, there are two different types of singularities for close-loop chains [43].

Inverse kinematic singularities

An inverse kinematics singularity occurs when the inverse Jacobian matrix from equation 25 is zero, hence $\det(J_\theta) = 0$. When this condition is satisfied the mechanism reaches boundary conditions or internal boundary limits. Typically, these positions represent locations where the velocity is directed outside the workspace and result therefore in no movement.

$$\theta_{2i} = 0 \text{ or } \pi \quad \text{for any of the } i \quad (26)$$

or

$$\theta_{3i} = 0 \text{ or } \pi \quad \text{for any of the } i \quad (27)$$

Condition 26 describes the position when limb *a* and *b* are parallel. This can mean that the arm is fully extended and the joint is at the pivoting point of going. Or when the leg is fully collapsed and limb *a* lies on limb *b*.

Condition 27 describes the position when the four bar linkage at limb *b* is completely collapsed either to the left $\theta_{3i} = 0$ or to the right side $\theta_{3i} = \pi$. In this position the moving platform is in a pivoting position and losses a degree of freedom.

Direct kinematic singularities

Direct singularities relate to the Jacobian matrix from equation 21. A singularity occurs when the determinant of the matrix equals zero. Condition 28 implies that the third column of J_p is zero.

Also Condition 29 eliminates the third column.

$$\theta_{3i} = 0 \text{ or } \pi \quad \text{for any of the } i \quad (28)$$

or

$$\theta_{1i} + \theta_{2i} = 0 \text{ or } \pi \quad \text{for any of the } i \quad (29)$$

Condition 27 is identical to Condition 28. While Condition 29 describes a singularity plane within the workspace. The mechanism gets into this singularity when limb b is horizontal. This Singularity is also further investigated in the Section 3.4.

3.3 Workspace

“The workspace of robot manipulator is defined as the set of points that can be reached by its end-effector.”[44] In this paper we refer to the “end-effector” as “moving platform”, more specifically the center-point of the moving platform describes the reached position of the mechanism. Restrictions to the motion of the moving platform can result from several factors. There are geometric limits in the reach of the mechanism as well as in the joints of the mechanism. Mechanism can self-collide or encounter singularities within the workspace. Limitations in the actuation can additional reduce the reachable area of the mechanism.[45] In this paper we use the discretization method where a regular grid with nodes around the mechanism is tested whether each node is in reach of the mechanism or not. Therefore, the calculation of the inverse kinematic from 3.2.2 is used to determine the joint angles of the mechanism ($\theta_{1i}, \theta_{2i}, \theta_{3i}$) at each node. The workspace consists out of nodes with valid joint angles which satisfy all conditions described in section.

3.3.1 Reduced Total Orientation Workspace

Since the delta mechanism does not constitute any rotational motion the calculation of the inverse kinematics results directly in all possible rotation configurations at this position which represents the “reachable workspace”. Since the mechanism suffers from possible self-collisions and has mechanical joint limitations a further investigation is necessary to calculate a reduced total orientation workspace. Figure 4 shows all angles and helps to understand the next assumptions for the mechanism. Due to the mechanical implementation θ_{3i} is not able to reach more than $\pm 20^\circ$ from its centred position. Also, it is not possible to bring the moving platform above the base platform since this would result in a self-collision. Therefore, only negative z values are possible positions. Another restrictions are singularities obtained in section 3.2.4. The extreme positions of complete extension as well as complete contraction needs be avoided and is governed by condition 32. Fur-

ther the singularity plane, shown by equation 33, in the middle of the workspace also represents unconditional positions which needs to be avoided. The singularity on $0 < \theta_{3i} < 180$ is already covered by condition 31 described above.

$$z < 0(\text{self-collision}) \quad (30)$$

$$\theta_{3i} = 90^\circ \pm 20^\circ(\text{joint limitation}) \quad (31)$$

$$0 > \theta_{2i} < 180^\circ(\text{extension and contraction singularity}) \quad (32)$$

$$(\theta_{1i} + \theta_{2i}) = 180^\circ(\text{singularity plane}) \quad (33)$$

The inverse kinematics is calculated and only nodes which full-fill the above-mentioned requirements are stored as valid positions. The resulting area is described as reduced total orientation workspace shown in Figure 8 and 10 (green).

3.3.2 Generic Geometry

The objective of this paper is to develop a delta mechanism geometry which can convert between landing gear and manipulator. The first approach was to pick a delta mechanism which allows to bring the moving platform below the base platform. To obtain this configuration the length ratio between the first limb a and the second limb b is picked to be equal. The configuration of this geometry in manipulation configuration is shown in Figure 6 below.

length	unit in [mm]
r	105
h	35
a	220
b	220

Table 2: Dimensions of generic, non optimized geometry

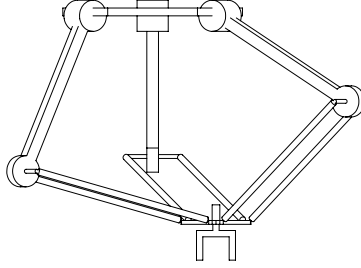


Figure 6: Delta robot with non-optimized geometry.

When the moving platform is then brought closely below the base platform, the mechanism has transformed into landing mode. In landing configuration, the ends of the first limbs a are providing contact points to the ground and establish a tripod geometry. Further the actuation of the first joints θ_{1i} allows height adjustment of the contact points. The capability to adjust three contact points is sufficient to define a plane and therefore, allows to adjust to any landing surface. Further it can be stated that as soon as three points are in contact with the landing surface the position is fully geometrically defined, shown in Figure 3.3.2. This property is used to determine if a stable landing position is reached. To evaluate feasibility and performance of this concept a first workspace

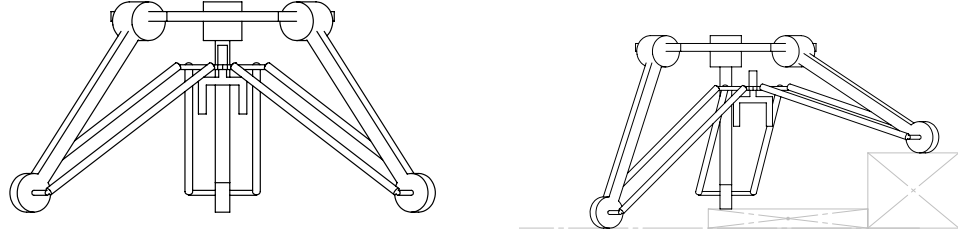


Figure 7: Tripod reconfiguration during flight & adaption to uneven surfaces for landing.

calculation is done. With the use of the described Reduced Total Orientation Workspace all possible positions of the moving platform are calculated. Figure 8 shows the final results. The green area represents the reachable workspace and the anchor-points of the first joints are shown for better special orientation.

3.3.3 Evaluation of Workspace from Generic Geometry

The workspace calculations show that a great range in the z-Axis. The mechanism can reach from 0 mm up to -450 mm below its base platform. Further it is shown that the workspace is limited in the x-, y-Axis. It can only reach about 50 mm in each direction. This is mainly caused by the passive joint limitations θ_{3i} which only ranges between $\pm 20^\circ$. Most notable is the interruption of the workspace between -200 mm and -100 mm. This is caused by the singular position when $(\theta_{1i} + \theta_{2i}) > 180^\circ$.

Since there are no valid position in this range, a transfer of the moving platform from the lower area to the upper area and vice versa is not possible. This represents a major limitation of the dual-function properties of the mechanism. An operation in the landing configuration (moving platform in the upper area) as well as operation in pure manipulation (moving platform in lower area) is possible yet a transfer from one mode to the other mode would require a crossing of a singularity plane. Theoretically it is possible to overcome this singularity by transferring the area with great speed by using the inertia of the moving platform to quickly cross the area-of-no-control [46]. This method of overcoming the singularity has been tested but lacks practical implementation. In the singular position additional rotational motions of the moving platform are possible. When swinging the platform through this area it is possible to reach a different rotational configuration. This event is hard to control and especially during an in-flight situation with unpredictable accelerations in all directions particular hard to manage. Another downside is that once the moving platform is rotated away from its planar position the mechanism can not recover and remains in this unwanted configuration. After conducting several tests this approach has been therefore deemed not to be promising. A more reliable and stable solution needs to be developed to ensure safe transmission between the operation modes.

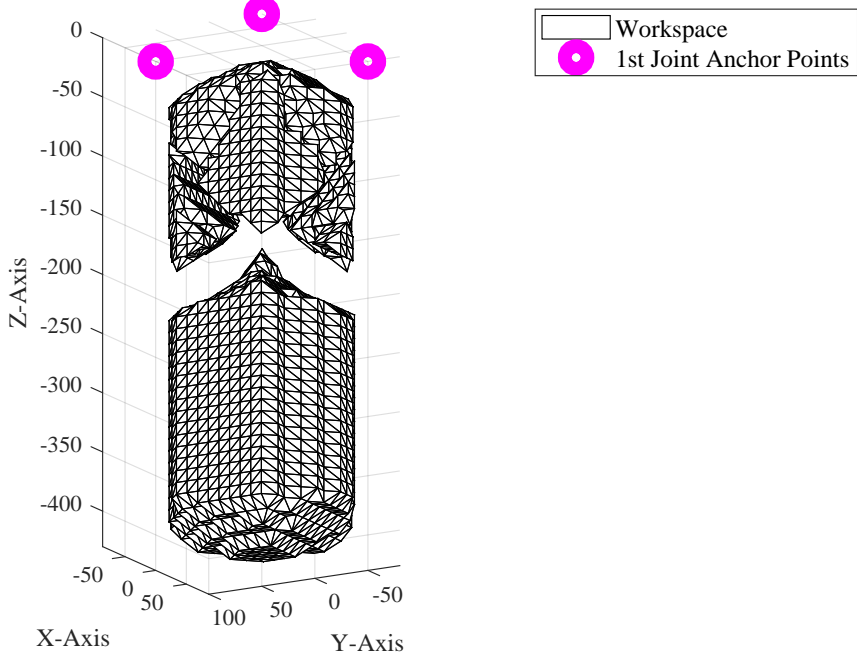


Figure 8: Reduced Total Orientation Workspace calculations with non-optimized geometry ($a = b$).

3.4 Singularity free Workspace for Reconfiguration

In order to allow a safe reconfiguration of the mechanism between manipulation and landing mode, the main objective of the optimization is to eliminate the singularity in the middle of the workspace shown in Figure 8. A geometrical analysis is carried out to understand the relation between the dimensions of the mechanism and the appearance of this crucial singularity. Figure 9 shows a 2D schematic of one leg of the mechanism. The problematic singularity occurs when $(\theta_{1i} + \theta_{2i}) = 180^\circ$ for a better visual description this can be characterized as the pose when limb b is horizontal. Thus, the approach is to mechanically avoid limb b reaching the horizontal configuration. In the left schematic illustration, the condition is shown which describes a possible configuration when b can reach the horizontal position. The geometric condition of this configuration is described as $b \leq b^*$ where $b^* = a + (r - h)$. In the boundary condition of $(b = b^*)$ b would be exactly horizontal when limb a reaches its maximum distance from the origin O . From this observation it can be stated

that for:

$$b > a + r - h \quad (34)$$

the condition $(\theta_{1i} + \theta_{2i}) = 180^\circ$ is geometrically impossible. This condition assigning the mechanism with a non-interrupted workspace.

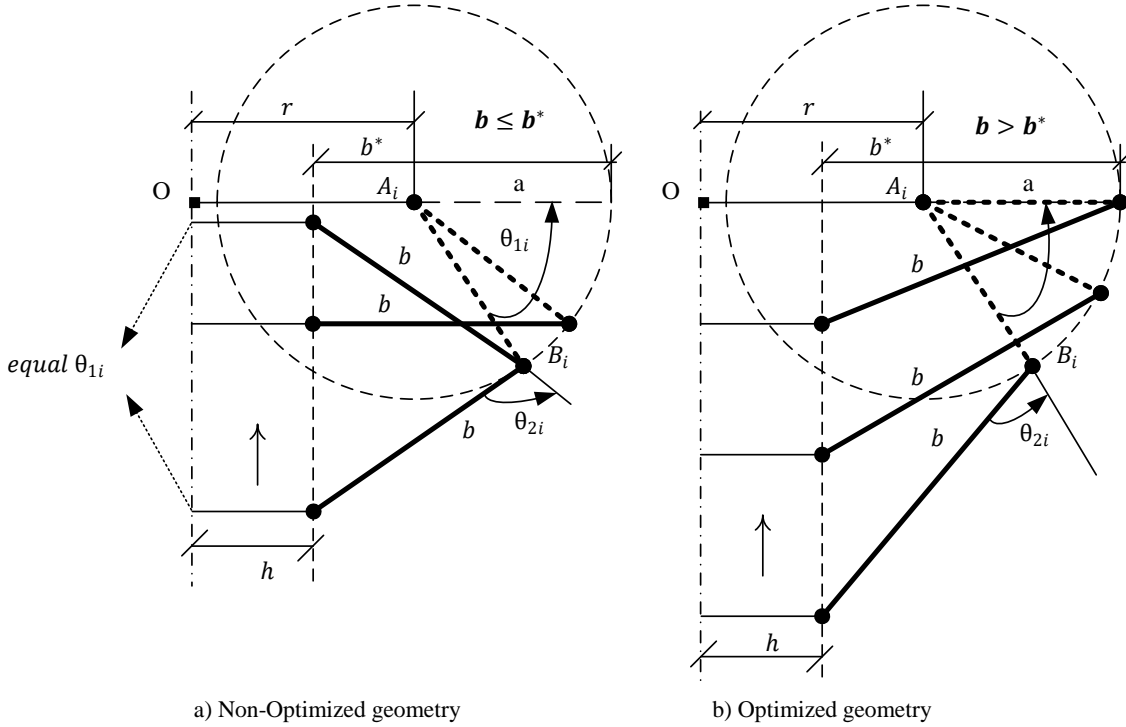


Figure 9: Line symmetric schematic of optimization of geometry. (left with singularity, right without singularity)

The size of the moving platform *r* is typically chosen to be smaller than the base platform. The author recommends a ratio of $r = h/3$ as an educated assumption which has not been further investigated. With the described conditions for the attachment to the flight vehicle it is now possible to fully define all geometries of the Manipulander based on the rotorcraft given. In this paper we present the calculation for the DJI Matrice 100 drone. The only dimensions necessary are the diameter of the wheelbase and the diameter of the main body. Consequently an optimized geometry for the mechanism was developed. For the realization of the dual-functioning of the mechanism limb *a* was picked to optimize the workspace. To satisfy the boundary condition 34 while using

previous dimensions 2, length a was determined to be $b > 290$. To ensure safe operation under all conditions length a is with 300 mm 4% bigger than necessary. Other dimensions remain unchanged. The achieved optimized geometry shown in Figure 16 has a continuous workspace but further changes are necessary to satisfy the dual-functioning capabilities. When the moving platform is brought to the locking position below the base platform, limb a is folded upwards. Hence, without further changes, the ends of limb a are no longer able to function as landing contact points. Later prismatic joints are introduced to extend and retract limb a shown in Section 3.5.1. This additional degree of freedom will only be used to transform the mechanism from a manipulator to a tripod landing gear and remains retracted and locked during manipulation mode. In consequence only the retracted configuration of limb a is considered for the workspace calculation, shown in Figure 10. A guideline to calculate all dimensions depending on the given rotorcraft is presented in Table 3. This calculation refers to a mechanism which is in manipulation mode, hence limb a is retracted. With the guidelines shown in the table it is now easily possible to calculate the basic dimensions of

Rotorcraft DJI Matrice 100	calculation	unit in [mm]
w	-	650
m	-	210
Manipulander	calculation	unit in [mm]
r	$m/2$	105
h	$r/3$	35
a	$w/2-h$	220
b	$>a+r-h$	>290

Table 3: Dimensions of Manipulander depending on rotorcraft geometry. Length a is retracted.

a Manipulander mechanism for any rotorcraft dimensions. The next section presents the workspace calculation of a Manipulander designed with the presented dimensions from Table 3.

3.4.1 Evaluation of Workspace from Reconfigurable Geometry

When the inverse kinematic is calculated with the new geometry and the condition for the Reduced Total Orientation Workspace are applied, we are left with the workspace. The workspace

calculations with the new dimensions are shown in Figure 10. The maximum reach in z is like the workspace of the generic mechanism. The reach in x- and y-axis remains unchanged. But, as predicted, the workspace is continuous, and the lower platform can be navigated below the base platform without crossing a singularity plane. At its centre the mechanism can come close (-80 mm in z) to the upper platform which is used to convert between manipulation mode and landing gear mode. On the top right side next to the workspace calculation is an illustration of the mechanism reaching the upper position where a locking mechanism keeps it in the central position to eliminate all DOFs. The lower illustration shows the mechanism performing normal 3DOF manipulations while the length of limb a remains retracted.

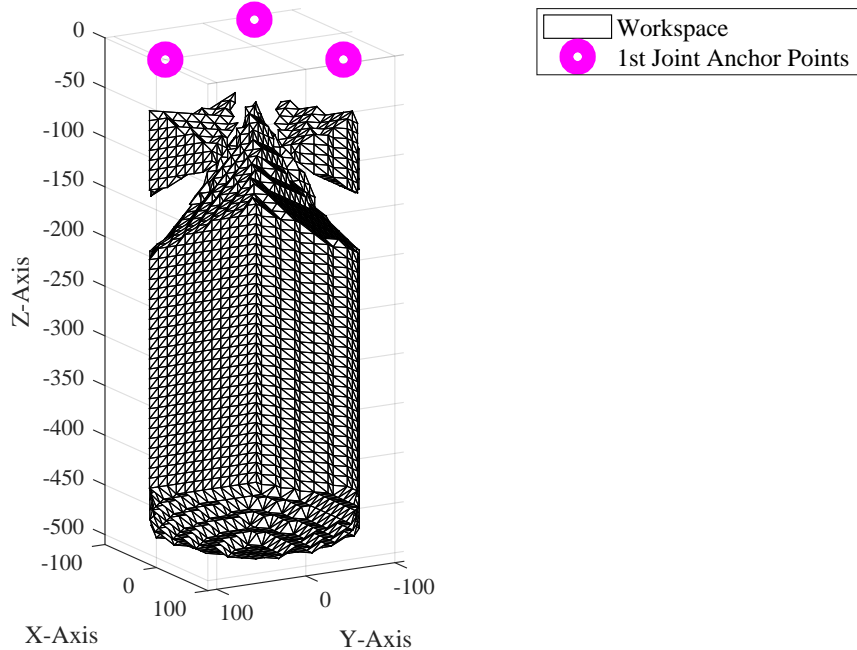


Figure 10: Optimized continuous workspace with $b = 300$; $b > b^*$.

3.5 Tripod Landing Gear Kinematics

The optimized geometry creates a continuous workspace and allows to manipulate the moving platform right below the base platform, but it also changes the geometry in a way that limb a is unable to be utilized as landing leg. An additional passive prismatic joint with a locking mechanism is introduced to limb a . Further a locking mechanism to lock the moving platform below the base platform is added. Unless for the conversion to the Landing Mode, limb a always remains retracted and the prismatic joint is locked. To convert from common delta robot manipulation to Landing Mode the moving platform is brought centrally close to the base platform where the new locking mechanism locks it in place. Once the moving platform is locked, the mechanism loses all DOFs and is fully constrained. Figure 11 shows the kinematics when the mechanism transformation into the landing mode. Since in this configuration C_i is locked the 4-bar parallel mechanism at limb b is replaced with a simple rod connection and the mechanism is treated as planar. With these simplifications it can easily be state that when the prismatic joint in landing mode is locked, the mechanism loses mobility. Once the prismatic joints are unlocked each leg gains an additional DOF, which allows it to rotate clockwise downwards to form the landing legs.

$$M = 3n - \sum_{i=1}^j (3 - f_i) = 3(N - 1 - j) + \sum_{i=1}^j f_i \quad (35)$$

- prismatic joint unlocked: $j = 4, n = 3, M = 1$
- prismatic joint locked: $j = 3, n = 2, M = 0$

Since the motion of this kinematic chain is interdependent the actuation motors for the manipulation at θ_{1i} can also be used to control and sense the legs motion in this landing mode.

3.5.1 Forward Kinematic of Landing Mode

In order to allow for the actuation of the landing leg, it is necessary to investigate the kinematics of this reconfigured mechanism. Especially for the safe guarded landing control in section 4.2 it is required to sense the position of its legs as a function of the encoder at θ_{1i} . The calculation of this forward kinematic is as follows: Since point C_i remains in a defined position it is used as

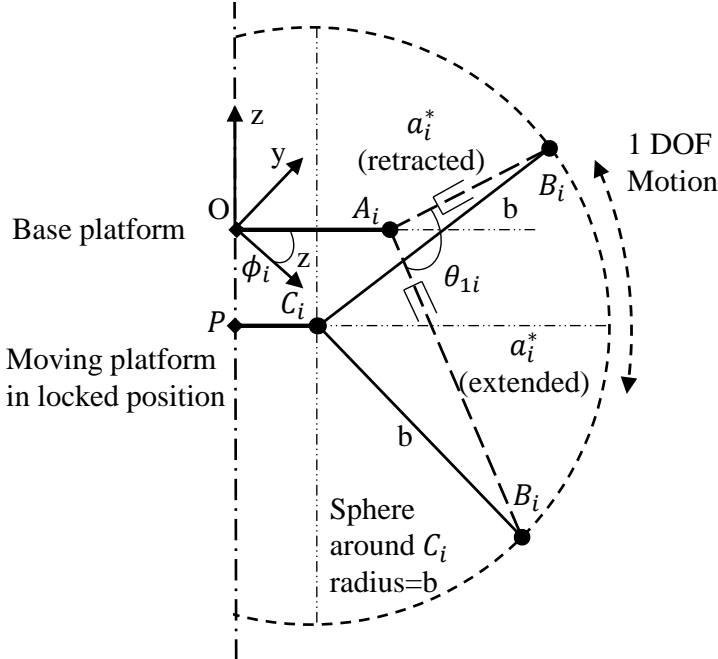


Figure 11: Line symmetric illustration of kinematics when reconfigured to Landing Mode.

centre-point to sweep a sphere with the radius of the fixed length b shown in Figure 11. This sphere represents any possible position of limb b . Since the angle but not the length of limb a is known, it is represented by a ray nesting at A_i and direction from unit vector l (defined by θ_{1i}). The ray is used to intersects the sphere around C_i , shown in equation 36 with the following parameters:

- a_i^* - distance along line to intersection from starting point.
- l_i - unit vector from A_i indicating direction of ray.
- b - radius of sphere

$$\|A_i + a_i \cdot l_i - C_i\|^2 = b^2 \quad (36)$$

Since l represents a unit vector with length one we can simplify to:

$$a_i^* = -(l_i \cdot (O - C_i)) \pm \sqrt{(l_i \cdot (O - C_i))^2 - \|O - C_i\|^2 + b^2} \quad (37)$$

where a_i represents the length of the telescopic limb between A_i and B_i . Which is used to calculate the position of B_{org_i} in the original coordinate system where T_i is the translation matrix.

$$T_i = \begin{bmatrix} -c\phi_i & -s\phi_i & 0 & -(r - h) \\ s\phi_i & -c\phi_i & 0 & 0 \\ 0 & 0 & 1 & 0 \\ 0 & 0 & 0 & 1 \end{bmatrix} \quad (38)$$

$$B_{org_i} = T_i \cdot (A_i + a_i \cdot l_i) \quad (39)$$

3.5.2 Inverse Kinematic of Landing Mode

In this chapter we solve the inverse kinematics when the mechanism is in its landing configuration. For the inverse kinematic is the position of B_i given and we are searching for the corresponding angle θ_{1i} . Since the mechanism of the leg can be seen as a planar mechanism and B_i is only moving on a fixed circle around C_i , there are only a limited amount of valid position for the landing leg and we would have always to use the exact correct coordinates for the inverse kinematics otherwise the calculation would result in an error. Hence, it is not practical to solve the inverse kinematics with a specific XYZ-coordinates of B_{org_i} and we use instead only the Z-coordinate which represents the height of the moving leg B_{iz} in respect of the Base platform. After providing the Z-coordinate the

kinematics will find the only valid point on the landing leg trajectory and return the corresponding angle θ_{1i} and the X,Y-coordinate of the landing point B_{org_i} . The inverse kinematics calculations start at the coordinate system nesting at Point A_i . From here a circle with the radius of b and the centre point at C_i marks all possible points on the trajectory of B_i . To find the right position to the given leg height of B_i we intersect this circle with a horizontal line. The line illustrates all points with the given height of Legend B_i and can be described as $z = B_z$. The quadratic equation below will now result in the unknown x value of B_i . Because of the quadratic nature of this equation it can result real or imaginary values. Imaginary values can be discarded since they represent positions outside of reach of the landing leg. The real values can be distinguished between a single or a double real value which represents one or two intersections points on the circle.

$$(B_{ix} - C_{ix})^2 + (B_{iz} - C_{iz})^2 = b^2 \quad (40)$$

To decide which value to use when the equation results in two values we can easily only use the solution with positive values B_{ix} since negative X-Values would mean that θ_{1i} is extended more than 55° which is mechanically not possible. This can be seen in Figure 11. Now as soon as the given Z-Coordinate results in a valid position all coordinates of B_i are known. (Y-coordinate of the endpoint is in respect of the coordinate system nested at A_i always zero since the landing mechanism can be considered planar) $B_i = (B_{ix}, 0, B_{iz})$. The angle at θ_{1i} can now be calculated as follows:

$$\theta_{1i} = \arctan\left(\frac{B_{iz}}{B_{ix}}\right) \quad (41)$$

With the use of the transformation matrix from equation 38 we can converter the results of B_i in the original coordinate system getting B_{org_i} for each leg.

$$B_{org_i} = T_i \cdot B_i \quad (42)$$

3.5.3 Conclusions Tripod Landing Gear Kinematics

With the complete inverse kinematics, we can calculate the positions of the landing leg. We can now present the basic dimensions of the landing gear in retracted (compact flight mode) and extended (landing mode) position. The Table below shows the basic dimensions. The maximum reach of the landing leg in z direction is from 0 to 260 mm. The angel for the extended configuration is particularly crucial for the landing gear behaviour and stability of the landing position. Due to the limited scope of this project the angle was set as an educated guess to 55°. Which demonstrates as compromise between a bigger clearance below the rotorcraft and stability of the landing position. A bigger angle would, therefore, allow for a better adaption to the landing surface where a smaller angel would decrease the span of the landing gear which leads to a more unstable landing position. To determine the optimal landing angle further investigations are needed. The current configuration will allow the landing gear to compensate for angels of up to 23% or objects with up to 225 mm height considering 35 mm as safety buffer between rotorcraft and ground.

Status of Landing Gear	Dimensions		
Retracted	$\theta_{1i} = 0^\circ$	$a_i^* = 220 \text{ mm}$	$B_{iz} = 0 \text{ mm}$
Extended	$\theta_{1i} = 55^\circ$	$a_i^* = 307 \text{ mm}$	$B_{iz} = 260 \text{ mm}$

Table 4: Basic dimensions of Landing Gear configuration - Centroid P of moving platform is mechanically locked 80 mm centrally below the Base platform. Shown in Figure 11

Additional limitations are to consider when landing on uneven ground. Even if the landing gear

compensates for the slope of the ground it is only practical to compensate for slopes up to a certain steepness. The friction between the ground and the landing gear contact points allow to calculate the maximum angle until the rotorcraft would slide off the slope. A typical friction factor μ_s between rubber and wet asphalt ranges between 0.25 and 0.75 [47]. The following equation let us directly calculate what the maximum slope angle could be before the system would slide off the slope.

$$m \cdot g \cdot \sin \alpha = \mu_s \cdot g \cdot \cos \alpha \quad (43)$$

$$\frac{\sin(\alpha)}{\cos(\alpha)} = \tan(\alpha) \quad (44)$$

$$\arctan(0.25) = 14^\circ \quad (45)$$

So, it becomes evident that the capabilities of the mechanism to compensate for up to 23° are more than sufficient. Depending on the material paring, it would be unsafe to land on slopes with inclines of 23° . We showed that with a material paring of rubber and wet asphalt, a landing would only be possible to an incline of 14° . This shows that the ability to compensate for slopes is more than given with the current mechanism.

3.6 Reconfiguration of Mechanism

This section describes how the mechanism uses reconfiguration to gain dual functioning as Manipulator and Adaptive Landing Gear. The Compact Flight Mode is seen as the default position of the Manipulander since it offers conversion to each configuration. Figure 12 shows how the mechanism can be converted. The compact flight mode is the default position. From here, the mechanism can be converted into Landing Mode or Manipulation Mode. In the following the transformation to the different configuration is described and characteristics of each mode are shown.

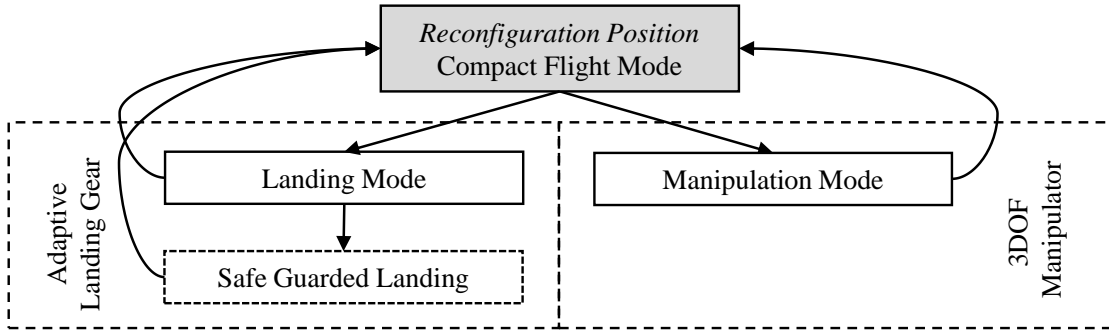


Figure 12: Reconfiguration of Mechanism between Manipulator and Landing Gear.

3.6.1 Compact Flight Mode as Reconfiguration Position

In Compact Flight Mode the legs of the mechanism are fully contracted and the moving platform is in its central locking position below the base platform illustrated in Figure 13. Since the telescopic joints on limb a are locked as well, the mechanism is fully geometrically defined and has zero DOF. Hence, the actuation motors on θ_{1i} can be deactivated. This position represents the default position of the mechanism and allows the direct conversion into 3DOF Manipulator or Adaptive Landing Gear. Using this configuration for flight holds additional advantages, in summary as follows:

- Direct reconfiguration to 3DOF Manipulator or Adaptive Landing Gear
- Lowest energy consumption due to deactivated actuators

- Masses closest to rotor-craft for best maneuverability
- Best aerodynamically characteristics
- Smallest geometrical foot-print

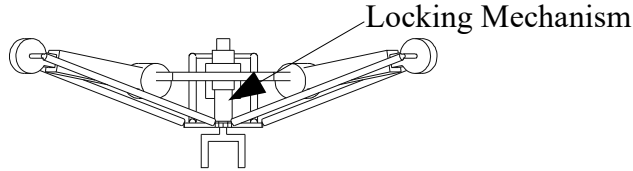


Figure 13: Compact Flight Mode for energy saving and reconfiguration of mechanism.

3.6.2 Landing Mode

From the Compact Flight Mode, the mechanism directly reconfiguration to the Pre-Landing Mode. Since the locking mechanism attached to the base platform ensures that the moving platform stays in this position, by unlocking of the prismatic joint, each leg's kinematic chain develops one DOFs. This enables the extension of the prismatic joints as the leg rotates downwards, driven by the motors at θ_{1i} . This motion stops when the prismatic joint becomes fully extended. In order to ensure that each leg is able to adapt to uneven surfaces, the limbs remain unlocked in this pre-landing stage. Each endpoint of the prismatic limb is a contact point for the landing gear shown in Figure 15. The actuation Motors exert a minimum torque to the legs for better in-flight control of the extremities as well as dampening of the landing impact. The control for the adaptive landing is described in Section 4.2 where the adaption to uneven surfaces is described in detail. The conversion process is illustrated in Flowchart 14 below. The landing gear configuration holds additional advantages, in summery as follows:

- Adoption to uneven surface
- Determining unsafe landing condition

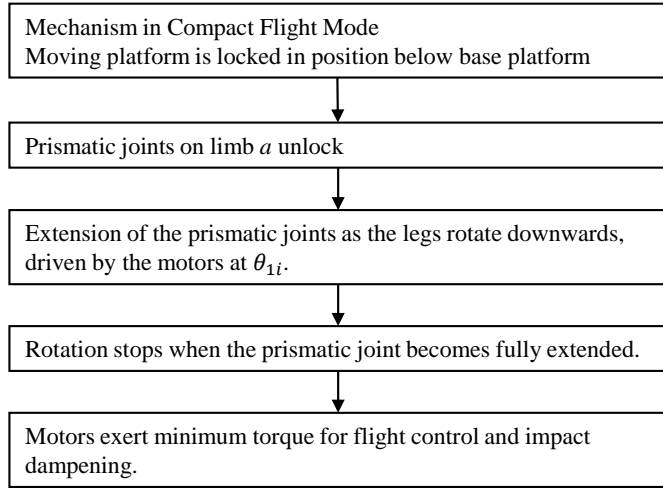


Figure 14: Flowchart describing the conversion to Landing Mode

- Stable tripod geometry
- Lowest energy consumption due to deactivated actuators
- Dampening of legs can be used to absorb impact energy

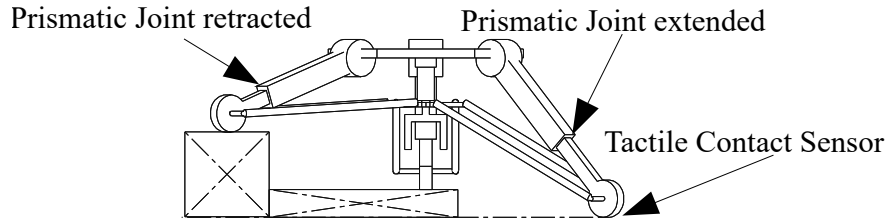


Figure 15: Adaptation to uneven surfaces in Tripod Landing Configuration.

3.6.3 Leaving Landing Mode

After lift-off, once the mechanism is in midair, the conversion from tripod configuration to the manipulating geometry is reversed to what is described above. The prismatic joints unlock, and the motors at θ_{1i} rotate limb *a* while retracting its prismatic joint. In the end position of the prismatic joint, the locking mechanism locks limb *a* from extension and the mechanism is converted back to its Compact Flight Mode, shown in Figure 13.

3.6.4 Manipulation Mode

To bring the mechanism into Manipulation mode, it is necessary to release the moving platform from its looking position. When the platform is released the mechanism gains 3DOF and represents a customary delta mechanism. To maneuver the moving platform to the manipulation position shown in Figure 16 the inverse kinematics described in Section 3.2.2 can be used to determine the actuation angles on θ_{1i} . A position control (Section 4.1) is introduced to allow controlled movements with constant velocity. Due to its parallel design the delta robot holds great advantages for the application attached to a rotor-craft. As all actuators remain during actuation in the same plane very close to the rotor-craft, the delta mechanism has very small moving masses. This minimizes the disturbance of the rotor-craft flight behaviour during manipulation of the moving platform. The delta mechanism holds additional advantages for aerial manipulation, in summary as follows:

- Low moving masses, therefore, less disturbance of rotor-craft flight behaviour.
- Low energy consumption
- Precise manipulation
- High velocity
- Wide reach below rotor-craft for distant manipulation

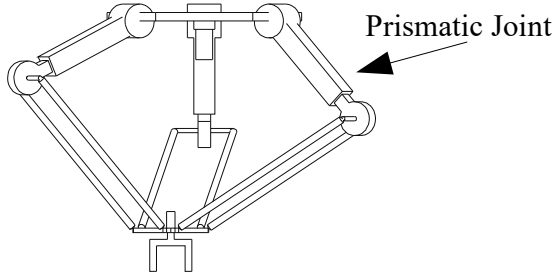


Figure 16: Manipulation Mode as Delta Mechanism allowing 3DOF.

3.6.5 Leaving Manipulation Mode

After manipulation or when an object needs to be transported over longer distances, the mechanism is brought back into its default configuration, the Compact Flight Mode. Due to the continuous workspace, the moving platform can be brought from any position of the workspace below the base platform and be locked in place. When objects need to be transported over long distances this allows for significant energy savings since the actuation motors can be deactivated and the freight is mechanically locked below the base platform. The prototype in Figure 50 and the accompanying video show a cable connecting the moving platform and the base platform. A winch at the base platform is used to help bring the moving platform below the base platform. This serves several purposes: it increases payload and compensates for low accuracy of the prototype when the moving platform is brought to the compact flight position, and in combination with a circular dock below the base platform, it serves as the locking mechanism for the compact flight mode. The winch mechanism is also shown in Section 5.2.3. However, the delta mechanism is able to bring the moving platform into the locking position without the use of a winch.

3.6.6 Conclusion of Novel Reconfigurable Delta Robot Mechanism

In this section a new mechanism was developed which is particular designed for aerial application. The advantages of each operation modes where shown and the configuration strategy between the modes is explained. It integrates a delta manipulator with an adaptive tripod landing gear. The Adaptive Tripod Landing Gear convinces with its compensation for uneven surfaces and a stable geometry while the Manipulation mode can use the advantages of the classic parallel delta manipulator and its high velocities and low moving masses. The reconfiguration position, which is taken during longer flights, holds the assembly without further energy consumption and reduces aerodynamic drag due to the compact configuration.

3.7 Finite Element Analysis

In this section we investigate the structural integrity of the mechanism. The von Mises yield criterion is used to determine critical areas of the mechanical design and possible ways to optimize the design to reduce weight without compromising stability. Van Mises is a computational method which allows to convert principal stresses σ_1, σ_2 into a scalar values σ_v . This allows to compare the computed results to the yield strength σ_y of the specific material [48]. In this very basic stress analysis, we only simulate static structural loads to get a basic understanding about the structural stability and weak-points of the mechanism. Both operation modes, Landing Mode and Manipulation Mode were simulated to investigate the fundamentally different load scenarios of manipulation payload and landing the rotorcraft on an even ground.

3.7.1 Stress Analysis Manipulation Mode

In this scenario we simulate the manipulation of payload. Since the payload is mostly restricted by the lifting capabilities of the rotorcraft, we assume the payload to be 10 N which is equivalent to roughly 1 Kg of payload. A static force of 10 N downwards describes a typical situation where payload is held in the centre of the workspace while no accelerations occur. The Base platform is therefore fixed, and the only force applied to the mechanism is the force caused by the payload vertically downwards towards the ground. In this scenario the maximum stress occurs in the parallel bar linkages between the moving platform and the ends of limb *a* shown in the figure below. Comparing the van Mises stresses to the maximum tensile stress of low quality σ_y ABS polymer at 46 MPa we can see that we archive a safety factor of 27. Hence, we can assume that the static stress in the Manipulation Mode is uncritical and does need to get further investigated.

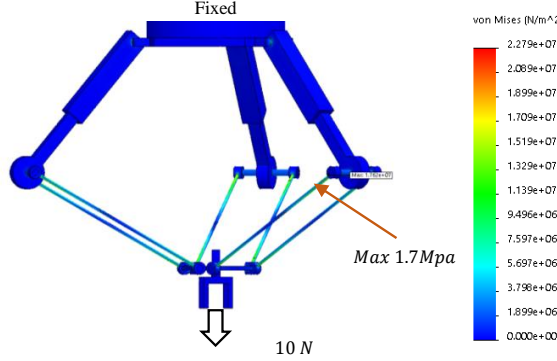


Figure 17: Von Mises Stress Analysis of Mechanism in Manipulation mode.

3.7.2 Stress Analysis Landing Mode

This scenario describes the mechanism during a landing on an even surface. To make a realistic simulation there are some assumptions made. The used DJI 100 Matrice setup has a maximum take-off weight of 3.6Kg. In order to simulate a rougher landing, the occurring forces are calculated as if the platform would fall out of 0.4 m height. One of the interesting features of the adaptive landing gear is that it allows to absorb part of the impact energy since limb a can rotate adjusting the landing leg height. This allows to absorb impact energy with the motors at θ_{i1} . In this calculation this is accounted for by a compression of the landing gear by $d_{comp}=10$ cm. With this assumption we come to an average impact force at the landing gear legs of $F_{ave}=141$ N. Hence, in the simulation we use 50 N at each leg. The simulation is set up such that the Base platform is fixed, and the force is vertically applied at the landing legs. The simulation setup is shown in Figure 18.

$$m = 3.6 \text{ kg}; h = 0.4 \text{ m}; d_{comp} = 0.1 \text{ m}$$

$$E_{pot} = m \cdot g \cdot h$$

$$F_{ave} = \frac{E_{pot}}{d_{comp}}$$

$$F_{ave} = 141N$$

The results of the simulation show the highest stresses in the parallel linkages similar to the

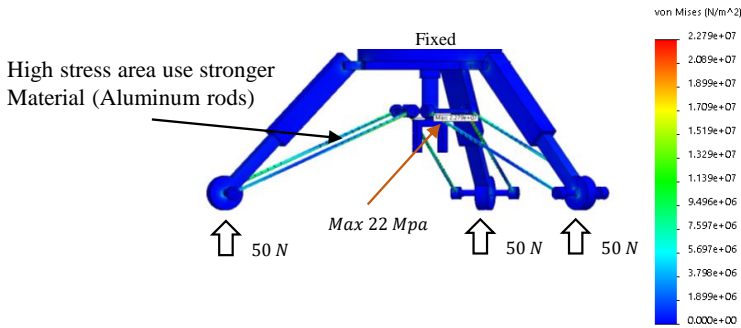


Figure 18: Von Mises Stress Analysis of Mechanism in Landing mode.

results from the simulation of the manipulation mode. But in this scenario the stresses are order of magnitude higher than stresses simulated in the manipulation mode. The maximum von Mise stress is 22 MPa which would only result in a safety factor of 2 if we would use ABS polymer for the parallel linkages. Therefore, it is recommended to use stronger materials like the commonly used 6061 aluminum for those parallel bars. This aluminum has a five times higher yield strength with 120 MPA. This results in a higher safety factor of 5.4 for the mechanism. The later build prototype uses due to the lack of availability of aluminum rods, steel rods as connecting elements which provide even higher strength but add unnecessary weight.

3.7.3 Conclusion Finite Element Analysis

This analytic study shows that the currently designed mechanism provides sufficient structural stability with a safety factor of 5.4 for static loads. Therefore, this mechanism can be used to construct a physical prototype. Since the simulations of the Landing Mode results in order of magnitude higher stresses than the Manipulation Mode further weight optimization only need to consider stresses caused by the landing of the rotorcraft. This is an important advantage since this allows to weight optimize the dual-functioning system as if it would be a regular adaptive landing gear. Simplified it can be stated that the Manipulander does not need a higher structural integrity than regular adaptive landing gears which could bring future designs to similar nimbleness.

4 Control

This Section will give a detailed description of the control of the mechanism both of the adaptive landing and the manipulation mode. In the first section is the motion control of the manipulation mode explained. It covers the trajectory generation and gives an outlook for improvements. In the following is the control of the Landing Mode investigated. While the basic work principle is described, a closer look is given to the Safe Guarded landing feature which prevents the rotorcraft from landing on dangerous slopes. Here are the Reaction Torque on the Rotorcraft during Self-leveled Landing investigated. Further is the ability of the adaptive landing gear to absorb impact energy during rough landing explained and in calculations elaborated.

4.1 Trajectory generation for Manipulation Mode

The trajectory generation is based on an initial path specification which provides the control with initial and goal position in Cartesian coordinates. In the Cartesian space is then a third-order trajectory calculated which ensues smooth transition between positions. All positions on this path (Cartesian space) are then transformed to the joint space using the inverse kinematics from Section 3.2. When all positions lay within the workspace and no unreachable joint positions are detected numerical methods are used to calculate angular velocity and angular acceleration to provide the motor controller with a full set of instructions. This process is shown in Figure 19 which illustrates a flowchart for the trajectory generation. The following paragraph then describes the trajectory generation and explains it on a general example.

4.1.1 Path Specification

The presented trajectory generation is an easy to implement Cartesian-based path-generation for the manipulation mode. The method uses a point to point trajectory where the moving platforms

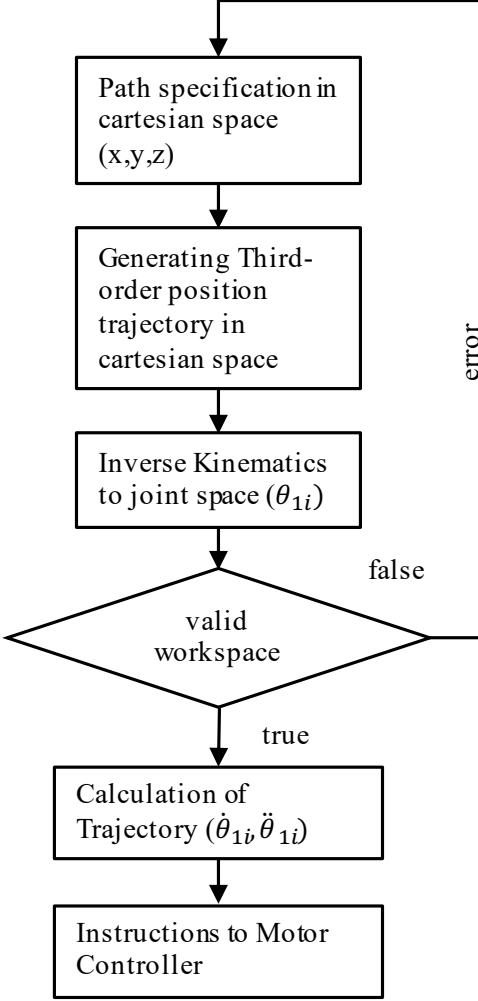


Figure 19: Flow chart of trajectory generation.

is moving along a straight line connecting a starting position A with the goal position B via the shortest path. In the following example we demonstrate the path planning for a motion between start point A [0,0,-100] to the goal position B [30,30,-500]. Figure 20 shows the mechanism performing a Cartesian straight-line motion [49].

4.1.2 Generation of Third-order position trajectory

Smooth motions are essential to reliable robot manipulation. Unsteady trajectories can decrease the system lifetime but mainly lead to a reduction in the accuracy of the manipulator [50]. A third-order trajectory is used which increases precision due to zero velocity endpoints while the moving

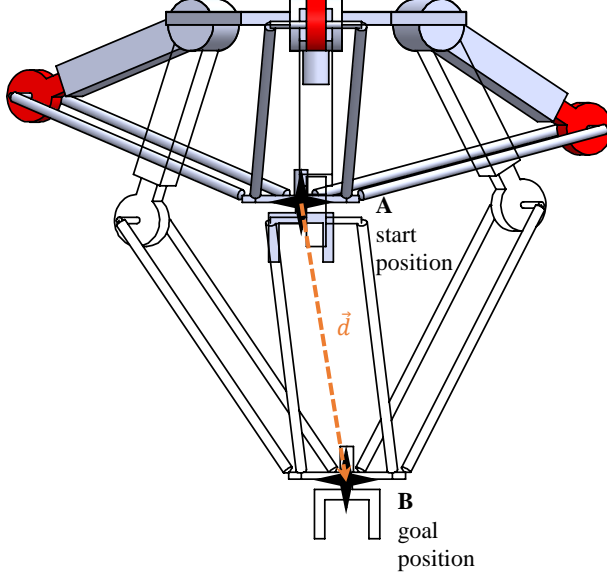


Figure 20: Manipulander performing point to point trajectory from point A to B.

platform accelerates steadily. For the generation of a trajectory an average speed for the moving platform needs to be specified. In this example this parameter is conservatively chosen to be $v_a = 20 \text{ cm/s}$. This reduced limit protects the actuators from reaching their performance limits. The controller is set to operate with only 20 Hz. For the trajectory now several parameters need to be calculated. In a first step vector \vec{d} is calculated, connecting start and endpoint 46. This vector is then used to determine the distance between the points. Using v_a the theoretical time time to reach this position 47 is calculated. Due to the incremental approach of a controller the moving platform likely does not reach exactly the desired position since the controller frequency (20 Hz) limits the positing increments to 0.05s. Nevertheless, results come very close to the desired position. In this example the calculated theoretical time is $t_t = 2.01\text{s}$ while the time to complete the trajectory for the controller will be $t_c = 2.0 \text{ s}$.

$$B - A = \vec{d} \quad (46)$$

$$\frac{|\vec{d}|}{v_a} = t_t = 2.01\text{s} \quad (47)$$

Now that the time to perform the trajectory is known the third-order trajectory can be calculated.

The equation for a third order equation is known as:

$$d(t) = a_3 t^3 + a_2 t^2 + a_1 t + a_0 \quad (48)$$

The function describes the distance d of the moving platform along a straight line in respect to time t . To define this equation, it needs four boundary conditions. In terms of positioning it is known that at time zero the moving platform has not traveled any distance from the starting point, therefore $|\vec{d}| = 0$. At time t_c the moving platform has traveled the full length of vector \vec{d} . Therefore, the condition for the equations are as follows for the start and end position:

$$d(0) = 0 \quad (49)$$

$$d(t_c) = |\vec{d}| \quad (50)$$

When equation 48 is derived in respect to time it leads to the velocity of the moving platform.

Which can be written as follows:

$$\dot{d}(t) = 3a_3 t^2 + 2a_2 t + a_1 \quad (51)$$

The velocity equation allows us to define additional boundary condition describing the end point velocities of the trajectory. In order to precisely reach the endpoints and to generate a smooth transition to the end points we defined the endpoints as zero velocity locations:

$$\dot{d}(0) = 0 \quad (52)$$

$$\dot{d}(t_c) = 0 \quad (53)$$

Now we can define all unknown factors to determine the third-order trajectory path which will perfectly transfer the moving platform between the positions.

$$a_0 = x_A = 0$$

$$a_1 = 0$$

$$a_2 = \frac{3}{t_c^2} (d(t_c) - d(0)) \quad (54)$$

$$a_3 = -\frac{2}{t_c^3} (d(t_c) - d(0))$$

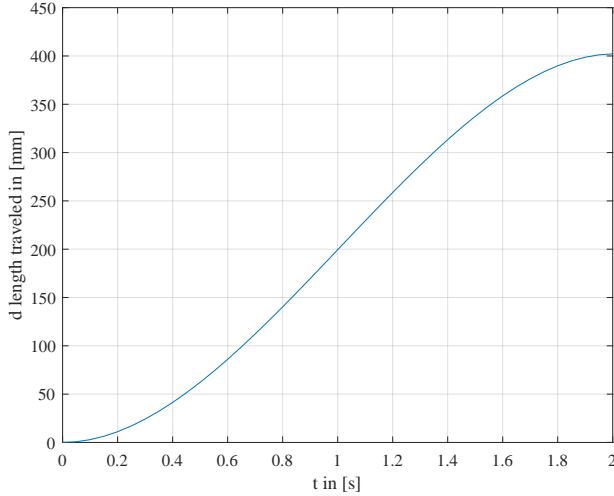


Figure 21: Angles of actuators during trajectory from point A to B.

To create the trajectory, the third-order function $d(t)$ describing the traveled distance, needs to be converted into a trajectory containing Cartesian Space (xyz) information. A numerical approach is used to find this information. Only points within the controller time step are considered, therefore the time points are $\Delta t = 0.05s$ apart leading to $t_c/0.05$ elements for t . At first the difference between

adjoining elements from $d(t)$ are calculated leading to an array of increments $s(i)$ where $i = t - 1$.

$$s(i) = d(i + 1) - d(i) \quad (55)$$

Figure 22 illustrates the length of each segment calculated from the third-order trajectory. A different way to look at this approach is to see the different segment length as the velocity of the moving platform. This is can be compared to Figure 23 where velocity and acceleration were algebraically derived and plotted from the third-order trajectory equation. The velocity and acceleration of the

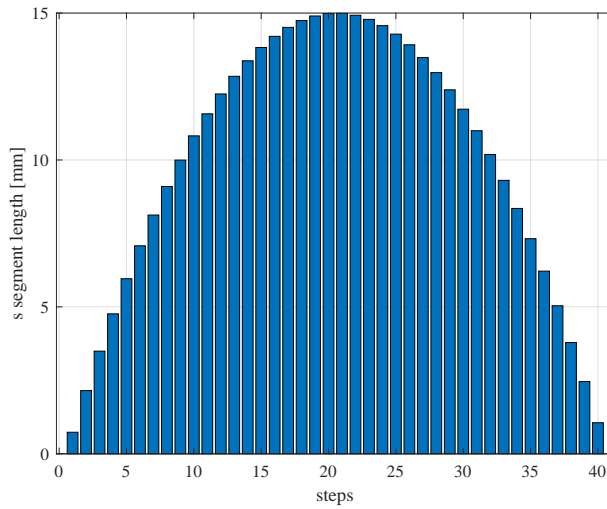


Figure 22: Illustration of array s which holds the segment length of each step.

moving platform can be directly calculated from the position data shown in Figure 23. Since the distance equation is a third-order equation velocity of the moving platform is as expected a quadratic equation while the acceleration is first order equation. This shows that the trajectory provides a very smooth transition of the moving platform since the acceleration is absolutely steady. Further can this information be used for dynamic modelling which is not covered in this thesis. Unfortunately, an easy derivative of the distance equation $d(t)$ is not sufficient for the motors since they can only use information in joint space. To get the joint space information for the motor controller, we need to generate a vector $s(i)$ which contains the distance between each position and when sent to

the controller with the predefined frequency, a trajectory with the acceleration and velocity defined in the third-order equation is formed. Since $s(i)$ describes the section length of each time step along

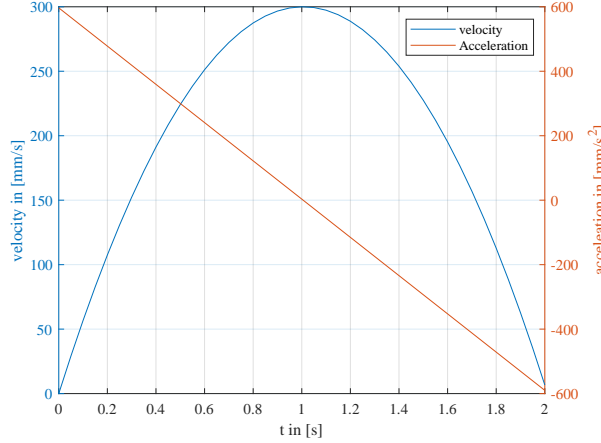


Figure 23: Comparison of the segment length to moving platform velocity and acceleration between point A and B.

the trajectory path. We can calculate the trajectory in form of an array of positions $pos(i)$ (xyz) along the straight path between point A and B. Starting with the initial position A each $pos(i)$ is calculated by multiplying the unit vector \hat{u} with the i th increment of the section length array $s(i)$. Calculating an array of positions describing the third-order trajectory is written as:

$$\hat{u} = \frac{\vec{d}}{|\vec{d}|} ;$$

$$pos(1) = A ; \quad (56)$$

$$pos(i+1) = pos(i) + \hat{u} \cdot s(i) ;$$

This calculation leads to $pos(i)$ 3x(i+1) trajectory array which starts at position A. This trajectory is visualized in Figure 24 where the unit vector \hat{u} is illustrating the distances between each controller step. With the generated position array $pos(i)$ which represents start and end position but also contains the timing, it is now possible to generate the joint positions for $theta_{1i}$ without worrying about a smooth transition between the positions.

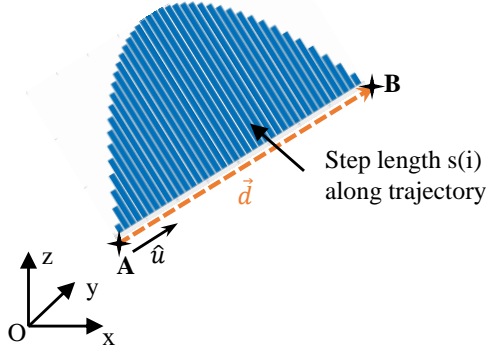


Figure 24: Illustrating trajectory generation with unit vector and step length $s(i)$ along the path.

4.1.3 Inverse Kinematics to joint space

Using the inverse kinematics from Section 3.2.2 we can now generate to array $pos(i)$ a corresponding array of joint angles $\theta(i)$ ($\theta_{11}, \theta_{12}, \theta_{13}$). With the help of the inverse kinematics, it is possible to determine whether the mechanism will cross an unpermitted area like a singularity or try to operate outside the workspace. If points outside the workspace would be in the trajectory an error is send back to the control requesting for a different Start and End point. The generation of the trajectory in joint space the inverse kinematics $inv()$ calculates from each element of the position vector $pos(i)$ from the previous section the corresponding joint angles $\theta(i)$ ($\theta_{11}, \theta_{12}, \theta_{13}$).

$$\begin{aligned}\theta(i) &= inv(pos(i)) ; \\ \dot{\theta}(i) &= \frac{\theta(i) - \theta(i-1)}{\Delta t} ; \\ \ddot{\theta}(i) &= \frac{\dot{\theta}(i) - \dot{\theta}(i-1)}{\Delta t} ;\end{aligned}\tag{57}$$

After all positions are converted into joint space the numerical derivative is used to determine the angular velocity $\dot{\theta}(i)$ while a second derivative determines the angular acceleration $\ddot{\theta}(i)$. This allows us to get all values of the motor controller without use of the Jacobin and the Jacobin Pus. But the method has some limitations. When we use the numerical derivative, the resulting vector is always

1 element shorter than the original vector. This is inherent to the method since only the differences between the positions are calculated and an average rate of change is calculated. This leads to the issue that it is not possible to determine the exact speed at time 0 or the end position of the vector. To overcome this issue of not matching vectors length we insert known positions at the end and the beginning of the vector to match the result to the boundary condition of the trajectory. The angular velocity is requirement to be zero at the start and end position. Therefore, the approach is to add points to the angle array to get a velocity array of the same length with velocity zero at the ends. Since difference between the two points is used to calculate the speed two points with the same position next to each other suggest zero speed between this position. Therefore, the second element of the angle array is overwritten to be the same as the first element. Then the a new element of the same value as the last element is added to the angle array shown in equation 58. This leaves us with us with an $i+1$ long position array. When this array is then derived it will result in an angular velocity array with i elements where the first and the last value is zero.

$$\begin{aligned}\theta(i) &= \text{inv}(\text{Pos}(i)) ; \\ \theta(i + 1) &= \theta(i) \\ \theta(\text{end} + 1) &= \text{inv}(B)\end{aligned}\tag{58}$$

Figure 25 plots the position array $\dot{\theta}(i)$ with $i+1$ elements. The first section of the graph shows the inserted plateau to achieve zero angular velocity at the beginning. Figure 26 show the resulting angular velocity where unsteady behavior at the beginning and the end is visible.

In order to get the angular acceleration, we need to derive the angular velocity vector which results in a $i-1$ long vector. Unfortunately, the value of the angular acceleration at the end is unknown and cannot be easily inserted. Therefore, the most rudimentary approach is taken to just copy the value of the last acceleration and extend the array by one with this value as shown in

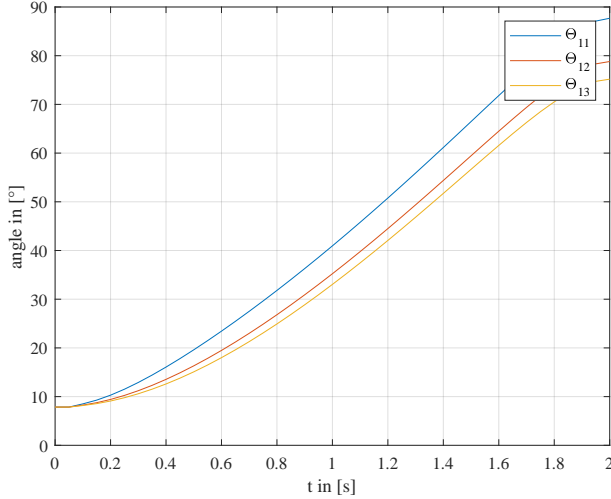


Figure 25: Angles of actuators during trajectory from point A to B with added positions at beginning and end.

equation 59. The resulting of this operation is shown in Figure 26.

$$\ddot{\theta}(end + 1) = \ddot{\theta}(end) ; \quad (59)$$

4.1.4 Conclusion of Trajectory generation for Manipulation Mode

The presented controller for the manipulation mode demonstrates a simple but efficient way to control the moving platform motion. It efficiently calculates a trajectory for point to point straight line motion. Since this implementation only covers a very basic implementations there are a few noticeable limitations.

Limitations:

Due to the numerical generation of the angular velocity and angular acceleration the values at the end positions cannot be determined. This can be seen in the unsteady graphs shown in Figure 26 and 27. Resulting in slight unsteady behaviour of the moving platform at the end and the beginning of each end position. Even-though those irregularities are minor and just last $\Delta t = 0.05s$ it would be easily possible to use post processing like smooth functions to reduce the irregularities. Since

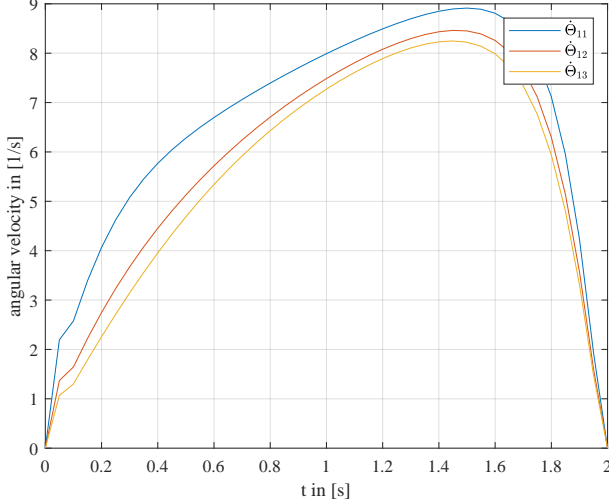


Figure 26: Angular velocity of actuators during trajectory from point A to B. Beginning and end shows unsteady behaviour due to the manipulation of the angle array.

after testing those sudden speed and acceleration changes where due to the inertia of the system not noticeable and the system was running on a simple microcontroller further post processing was not implemented.

Future implementations:

Since the control allows in this state only point to point straight trajectory with constant speed a newer version should allow for more complex path planning. For aerial application the dynamic behavior is especially crucial since it impacts the flight behavior of the rotorcraft. Therefore, it would be necessary to implement a dynamic controller which allows to plan for motions of the moving platform. A base for this work could be found in [51] where a simplification of the dynamic equations of the delta robot are found to perform real time control. Another interesting new aspect for the control of the motion control of the moving platform would be an integration of a path optimizing algorithm. This would also allow to avoid obstacles in the workspace which could be beneficial for the aerial application [52].

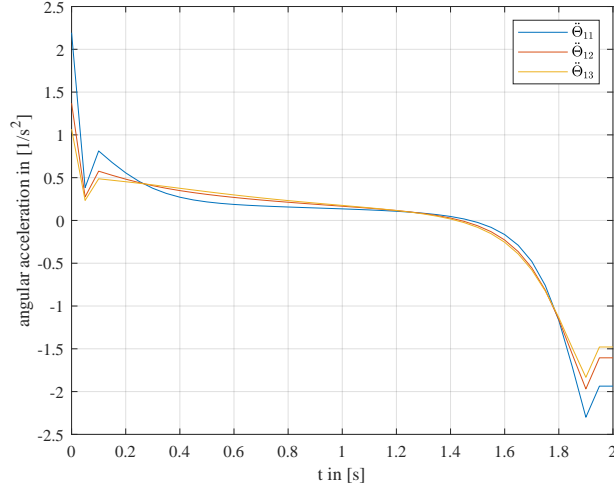


Figure 27: Angular acceleration of actuators during trajectory from point A to B.

4.2 Adaptive Landing

In this section several aspects of the landing mode are investigated. The principle of the adaptive landing is explained in first section while the following section explains the control of the motors and investigates the reaction torque on rotorcraft during the self-leveled landing.

At this stage of the research the rotorcraft controller and the manipulander control operate independently. For the self-leveled landing it requires the flight controller of the rotorcraft to balance the flight vehicle in a horizontal position. The ability to counteract external disturbances differs greatly between rotorcraft type and design of the flight controller. To simplify the problem, it is a main objective to keep the disturbance during landing to a minimum while it is assumed that the rotorcraft is capable of balancing the system during the landing sequence. For later research it is recommended to design a dynamic flight controller incorporating the manipulander control into the rotorcraft.

4.2.1 Adaptive Landing Sequence

For the Adaptive Landing the unlocked prismatic joint allows a rotary motion of limb *a* enabling for independent height adjustment of each leg to accommodate uneven surfaces. While the rotor-

craft is lowering to the ground, it remains in a horizontal position as does the base platform of the mechanism attached to it. Tactile contact sensors at the end of each leg detect ground contact. When a leg touches the ground it, will not lock its position until all three legs have contact as the rotor-craft continues to lower. If for example the ground is perfectly planar, all three legs will touch

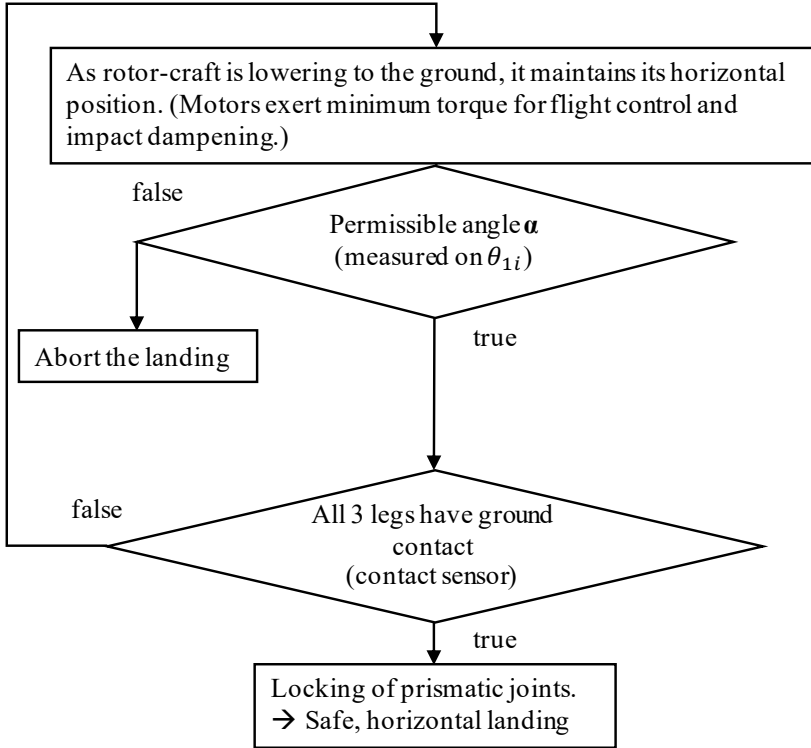


Figure 28: Flowchart describing the Safe Guarded Landing sequence.

down simultaneously and will lock instantly upon contact. This continues until either all three legs have made contact with the ground, thereby locking the legs in position, or until the mechanism reaches an impermissible angle α , meaning the ground is too uneven for safe landing. In this case a signal can be sent to the rotorcraft controller to abort the landing. When the rotorcraft has determined a safe landing position locking of the prismatic joints allows to deactivate all motors for energy preservation. This sequence illustrated in the flowchart in Figure 28 ensures that the rotor-craft remains in a safe, horizontal position even when landing on uneven surfaces. An example of a rotor-craft landing on uneven surface is given in Figure 15.

4.2.2 Calculation of Landing Angle for Safe Graded Landing

For the calculation of the landing angle it is necessary to determine the position of the contact points (B_1, B_2, B_3) shown in Figure 29.

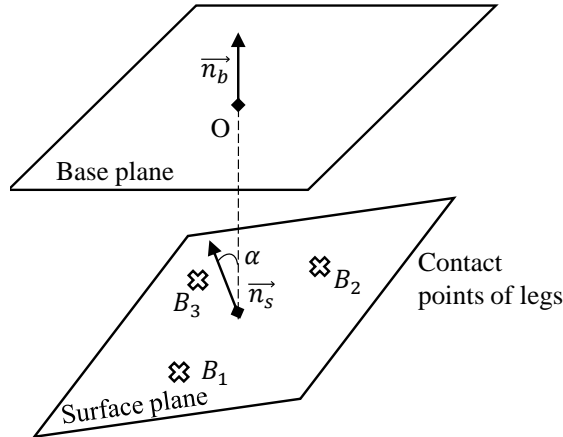


Figure 29: Determination of Surface plane and Landing Angle α .

These three points define geometrically the surface plane which is then used to calculate the slope with respect to the drone base platform. After calculation of the position of the leg ends B_i , using the inverse kinematics from Section 3.2.2, the normal surface vector \vec{n}_s is calculated, characterizing the landing surface. Using the cross product with the base normal vector \vec{n}_b , defined by the z-axis, we receive the Landing Angle α with respect to the rotor-craft, see equation 60.

$$\cos(\alpha) = \frac{|\vec{n}_b \cdot \vec{n}_s|}{\vec{n}_b \cdot \vec{n}_s} \quad (60)$$

The geometry and the physical design allow for a maximum landing angle α of up to 23° . Steeper angles are not desirable since it reduces the ground clearance and incenses the risk of interference of the mechanism with the surface. Steep landing angle also increases the risk that the rotorcraft loses traction on the surfaces and uncontrolled motions on the angled surface become possible. The extreme case of an adoption to a 23° incline can be also compared to the landing of a 225 mm high object. Here one leg would rest on the object while the other two are on a level plane.

4.2.3 Motor Control for Adaptive Landing

To allow the landing legs to adapt to the landing surface a motor control for the main at motor θ_{1i} was developed. The control regulates the leg length as soon as it gets into contact to the landing surface. The main requirements to the control were as follows.

- Fast, responsive and reliable
- Backdrivability to adapt legs length to uneven surfaces
- Energy absorption of landing impact
- Providing sufficient contact force for tactile contact sensors

A control which meets the requirements above is presented in the following paragraph. In Landing Mode the angle θ_{1i} of each leg is set to 55° . This is describing the pre-landing position when the landing gear is fully extended, and this angle is then used as reference for the motors' PID controller. Such that this control tries to maintain this angle during the entire landing sequence. During landing when a leg gets into contact to the ground, it rotates upwards bringing the motor out of its reference position. Thus, the PID control tries to counter this by sending a current counteracting this motion. In the presented control scheme, the maximum torque generated by the motor is limited by a current limiter after the PID control. This causes the motor to generate a constant torque which tries to rotate each leg back into its reference position. To set this torque limit, it is important to keep several aspects in mind. A high torque limit to keep the leg in reference position has the advantage of proficient energy absorption of the landing impact, further ensures it a sufficient contact to the surface for the tactile contact sensors. As a drawback of a high motor torque, destabilizes this interaction to the ground the hovering rotorcraft during the landing sequence. To ensure a planar landing position the rotorcrafts flight controller needs to mitigate this disruption which can potentially bring the rotorcraft off balance. Therefore, it is necessary to

keep the motor torque to a level that allows the contact sensors to provide a sufficient contact force and best possible impact absorption while not disturbing the rotorcrafts flight behaviour. To find the best-balanced maximum motor torque a straight forward approach is presented. The minimum force to trigger the tactical contact sensors at B_i defines the maximum torque τ_{max} on the landing leg. The this force is for the specifically used tactile contact sensor 1N, compare to Section 5.2.1. Hence the motors need to generate a torque which causes at point B_i a force orthogonal to the base platform of 1N in any position of the landing leg. Since the effective length to generate this force changes depending on the angle θ_{1i} the position with the longest extension is used to define τ_{max} ensuring that the resulting force will be $> 1N$, shown in Figure 31. An illustration of the motor controller is given in Figure 30. In Figure 31 the contact force is simplified to be orthogonal to the

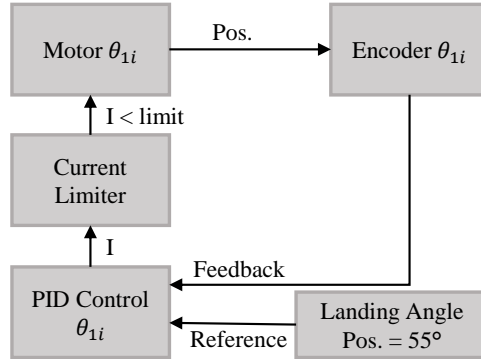


Figure 30: Motor Control for Self-leveled Landing.

base platform at B_i , which allows to assume that the lowest contact force would be generated when link b is horizontal since a_{eff} is here the longest. Hence, when the motor is able to generate 1N at this position, any other position would supply at least this level of contact force. Therefore, the torque limit for the motors τ_{max} is defined by this position. For this the effective length a_{eff} needs to be calculated. Since C_i and B_i have the same Z-Coordinate we can use the inverse kinematic of the landing mode from Section 3.5.2 to calculate the landing angle θ_{1i} belonging to this position of the landing leg. In order to calculate the effective length causing the torque at the motor we use

equation 41 from the forward kinematics to determine length a_i^* . For the given geometric dimensions

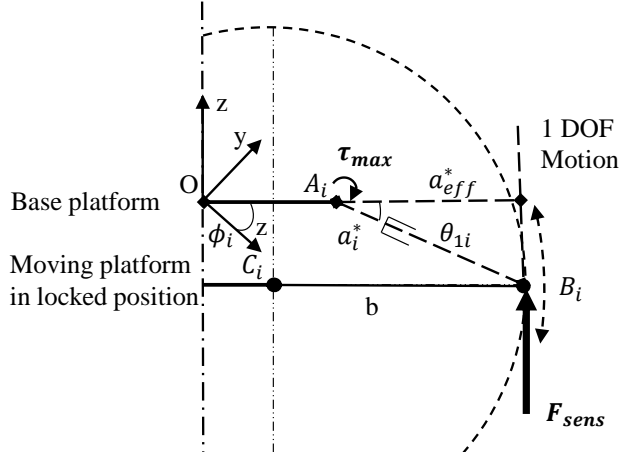


Figure 31: Torque limit calculations. Landing leg in the position which provides the smallest force at B_i .

and the forward kinematics of the landing gear from section 3.4 we calculated an angle of θ_{1i} of 19° which leads to an effective length of $a_{eff}^* = 231 \text{ mm}$. Now simple momentum calculations lead to the maximum contact force of each leg depending on its motor position. Since the resulting force is depending on θ_i and the greatest force is appears when the angle is the biggest, the landing position of 55° will cause the greatest force, while when b is parallel to the platform the force on the tactile landing sensor is as expected the smallest.

$$\tau_{max} \geq F_{sens} \cdot a_{eff}^* \quad (61)$$

$$\tau_{max} \geq 1N \cdot 0.231 \text{ m} \quad (62)$$

With this control setting it can be ensured that when the motors keep the torque up to $\tau_{max} = 0.23 \text{ Nm}$ then the contact forces at the landing legs during the landing sequence will be greater then 1 N.

4.2.4 Reaction Torque on the Rotorcraft during Adaptive Landing

In this Section the reaction torque on the rotorcraft caused by the interfacing of the adaptive landing gear and uneven ground is investigated. As previously described when the system is in landing mode the motors are set to maintain the landing position of the landing legs at 55° while limiting the maximum torque to τ_{max} . The theory of this control design is discussed in the following paragraph.

For the adaptive landing it is necessary to consider both the flight control of rotorcraft and manipulander as a combined system. When the rotorcraft is lowering to the ground the flight controller balances a horizontal flight position of the system while the landing legs mechanically adapt to the landing surface. The adaption to the landing surface is caused by the mechanical height adjustment of each landing leg which causes disturbance of the rotorcraft. The adaptive landing sequence ends when all legs are in contact to the surface. A vertical force at each leg end is generated when the landing legs are starting to get in contact to the ground. Each of these forces F_1, F_2 causes a torque on the base platform τ_1, τ_2 . This process requires the rotorcraft flight controller to counter all forces F_{res} and torques τ_{res} on the platform to ensure a horizontal landing shown in Figure 32. To understand how the mechanical design and the motor control co-function to ensure a confined force and torque level at the system we need to look at the extreme situation for the landing gear system. To investigate the greatest reaction forces and therefore the most difficult situation for the rotorcraft to stabilize its position, the instance when two landing legs are in contact to the ground to be most critical. This situation is the most critical since forces from both legs introduce torques into the system. The instance when all three leg are in contact to the ground is not interesting since the rotorcraft then has reached a stable landing position. If only one leg has ground contact, there is only one leg generating force and torque destabilizing the rotorcraft. Therefore, the following paragraph always relates to the instance of two legs in full contact to the

ground while the third one is still in midair. For a better understanding, the following paragraph separately analyzes the impact of torque and force.

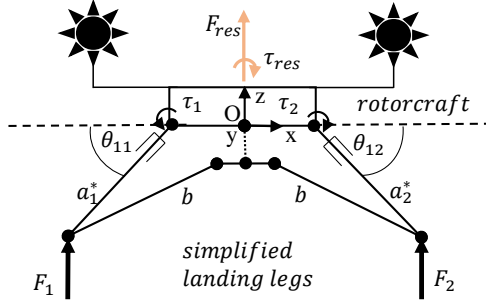


Figure 32: Resulting forces on rotorcraft during touchdown of the first two landing legs.

Force:

Since during the adaptive landing the torque on the motors is limited, the maximum reaction force F_1, F_2 of each contact point can be easily calculated using the forward kinematics for the landing mode. The highest possible reaction force is therefore when the landing leg is in its default landing position at 55° which results in a total vertical force F_{res} at the platform of $2x2N$. When the legs rotate during the landing further upwards the reaction force decreases with increasing θ_i since limb a_i extends and the motor torques generate a lower reaction force. For the controller of the rotorcraft a pure vertical force on the platform is easy to balance since it is generated by the weight of the lowering rotorcraft. To increase the downwards force, the flight controller simply needs to reduce thrust. The impact of pure forces introduced into the rotorcraft can be summarized in the following statements:

- Pure vertical forces are easy to compensate for the system.
- Each leg causes a reaction force depending on θ_i .

Torque:

A more critical disturbance of the horizontal position of the rotorcraft is the generated torque from the reaction forces of the extended landing legs. As previously discussed, we only investigate the

worst-case situations since these are crucial for the flight controller. Figure 33 shows the maximum

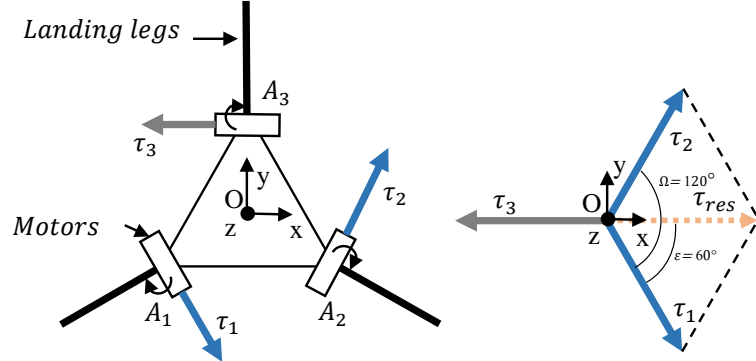


Figure 33: Torques on rotorcraft platform during adaptive landing. On the left side is a spatial overview of the motors on the platform while the right side shows the torque-vector summation.

torque on the system when two legs are in contact to the ground. The blue arrows indicate torque generated from the motors while the grey arrow is just a place holder for the torque capabilities of this motor. In this example leg 1 and leg 2 are in contact to the ground. Since the motor torque is limited to τ_{max} the torque during the instance of two legs in contact to the ground can only range between 0 and τ_{max} depending on the deflecting of the landing legs. To allow for the best adaptive landing performance of the system, it is important to reduce the torque input on the platform. While one leg exerts up to τ_{max} into the landing platform, the landing gear geometry is chosen to compensate for the torque generated by the second leg in contact to the ground. This is achieved by using a geometry that arranges the torque vectors in a way that adding two torque vectors never exceeds the magnitude of the torque limit of each landing leg τ_{max} . This can be proven with the formula below, describing the addition of two equal torque vectors with an angel between them and is also shown in Figure 33.

$$\tau_{res} = \sqrt{\tau_i^2 + \tau_i^2 + 2\tau_i\tau_i \cos \frac{\theta}{2}} \quad (63)$$

We can simplify this common vector addition to the following, while we make the restriction that the resulting vector should be the same as each individual vector $\tau_i = \tau_{res}$. Using this formula, we

can search for the angle between equal vectors so their addition will be equal their own magnitude.

$$\tau_{res} = 2\tau_i \cos \frac{\theta}{2} \quad (64)$$

$$\Omega = 2 \arccos \frac{1}{2} = 120^\circ \quad (65)$$

The resulting spacing between the torque vectors of $\Omega = 120^\circ$ represents the same geometry of the delta robot platform which describes an equilateral triangle. Therefore, the geometry of the Manipulander allows for a landing gear which regulates the resulting torque on the system to the maximum torque of each individual torque vector. Not just the magnitude of the torque is an important factor for the rotorcraft controller also the shifting in direction of the torque vector should be minimized. Since the torque on the platform is only generated by the motors of the landing legs, a shift in direction occurs when two legs are in contact to the ground. Between two legs are always 120° hence, one would assume the torque can shift between this range. In practice it is unlikely for the torque to shift more than 60° . As soon as the first leg is in contact to the ground and the rotorcraft lowers further it will exert the maximum torque and use its backdrivability to adapt to the surface. When the next leg now gets in contact it is only possible to exert a torque smaller or equal to the torque of the first leg. When the second leg exerts not the maximum torque on the platform, the torque only shifts to the center of both vectors which is equivalent to a shift of $\epsilon = 60^\circ$. An example of this situation can be seen in Figure 33. When the second leg exerts a smaller torque the shift in direction would be smaller than $\epsilon = 60^\circ$. However, a shift of the resulting torque greater than 60° is theoretically possible if during a rough landing the first leg in contact would slip into e.g. a hole. In this scenario the torque would now only be generated by the second leg shifting the resulting torque about 120° . This describes a rather unusual but possible scenario and is important to mention but will not be primarily investigated in this paper. The investigation

around the platform torque during the adaptive landing can be summarized in the following statements:

- The maximum torque on the platform is equal to the torque limit τ_{max} set to the motor.
- During landing the torque vector direction would only shift up to $\epsilon = 60^\circ$, with some unusual exceptions.

4.2.5 Energy absorption during rough landing

An additional advantage of an adaptive landing gear is the ability of absorbing impact energy. Rough landings cause vibrations and structural loads which are recognized as the significant factors causing fatigue damage and damage in the electrical components [53] on a rotorcraft. The adaptive landing gear prevents this since the main motors are set during the landing to exert a constant torque to the landing legs allowing them to absorb and convert impact energy into electric energy. As a simple investigation we follow the example from Section 18 and assume a rough landing as a free fall from 0.4 m. The following calculations will show how much of the kinetic energy caused by the free fall can be converted into electricity and which part will be absorbed by the structure of the landing gear. The main motors at θ_{1i} are set to exert a constant torque of 0.23 Nm. Since torque (Nm) is equivalent to energy (J) the exerted torque on the motors is the energy absorb by the motors when the landing gear hits the ground. Therefore, we can calculate the part of the kinetic energy which will be converted into electricity while the rest reaches the landing gear structure where it is converted into heat and deformation.

$$E_{pot} = 14.13 \text{ J}; \tau_{max} = 0.23 \text{ Nm}$$

$$3 \cdot \tau_{max} = 3 \cdot 0.23 \text{ Nm} = 0.69 \text{ Nm} = 0.69 \text{ J} \quad (66)$$

$$\frac{E_{motor}}{E_{pot}} = \frac{0.69 \text{ J}}{14.13 \text{ J}} = 4.9\% \quad (67)$$

The calculation shows that 4.9% of the energy from the impacts converted into electric energy. However, this does not seem to be a significant amount but contributes to a more resilient structure since not all energy needs to get converted by the structure of the mechanism. Further it should be noted at this point that the introduction of dampening elements like air shocks into the prismatic joint at a would allow for a far better dispersion of the impact energy which would prevent the rotorcrafts from damage.

4.2.6 Conclusion on Adaptive Landing

The developed adaptive control allows for a safe and reliable Self-Leveled Landing on uneven terrain with slopes of up to 23° or similar the landing with one leg on a 225 mm high object. The physical interaction to the ground allows to continuously monitors the landing incline and reliable detection whether the landing gear has reached a safe landing position. The proposed control scheme benefits from the landing gear geometry minimizing the reaction torque on the rotorcraft. This integration of motor control and geometry of the landing gear offers an efficient reaction torque control on the rotorcraft and allows for an easy integration into various rotorcraft types. In the event of a rough landing, the adaptive control of the legs has the additional effect of absorbing impact energy during landing. A proposed design with air shocks at limb a could significantly improve the impact durability.

5 Prototype Development and Construction

This Section will describe the construction of a physical prototype. At first the electrical hardware and then interesting mechanical components of the design are described. Majority of the structural elements are 3D printed, except for the four-bar parallel mechanism which connects the first limb and the moving platform. This element is built of IGUBAL rod end bearings and steel rods. The main motors at the first limb of the mechanism are low cost Dynamixel AX-12 while the looking mechanism and the centre winch is driven by micro gear DC motors. The tactile sensing elements at the end of each leg are composed of a 3D printed structure and an off-the-shelf sliding joystick as sensing element. The computation and control run on a Teensy 3.2 microcontroller. Via a Bluetooth connection the prototype is remote controlled and can operate independent from any physical connection.

5.1 Electrical Components and Circuit Design

For the electrical design, the setup consists out of a LIPO 1300 mAh battery which generates between 11.1V and 12.6V. This voltage is then stabilized to a 5V and 10V connection using voltage regulators. The 10V line is used to power the Dynamixel AX-12A motors while the 5V is used to power the micro-controller bluetooth module, motor drive and logic level converter. The 12V micro gear motors take their energy directly from the batteries which reduces the load on the voltage regulators. Figure 34 shows the an overview of the hardware and the bus interfaces. The two main components the microcontroller and the main actuator are briefly introduced in the following.

5.1.1 Teensy 3.2 microcontroller

The Teensy 3.2 is a USB Development Board with a Cortex-M4 is a 32 bit ARM processor. It has a small form factor while offering high processing power and memory. It is fully compatible with

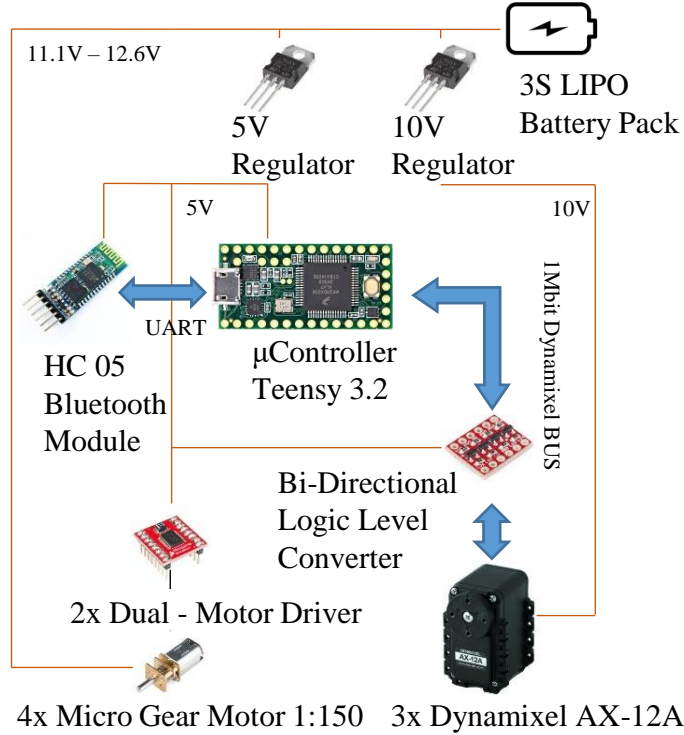


Figure 34: Electrical Hardware Architecture and Bus interfaces.

Arduino Software and Libraries which makes it easy to migrate code when a project matures from the arduino board. [54]

5.1.2 Dynamixel AX 12A Motor

The Dynamixel AX 12 A motor is used for the main actuation at joint θ_{i1} . It is an integrated modular actuator that incorporates a gear reducer of 1/254, the maximum stall torque is 1.5Nm and the encoder can pick up to a resolution of 0.29°. The maximum speed of the motor is at 59 rpm. A precision DC motor and a control circuitry allows to position control the motor position using a PID control. The Controller allows a several of settings including limiting the motor torque which is used in this setup.[55]

5.1.3 Circuitry design

The PCB layout was done using the open source software KiCad. The board is measures 65mm by 70mm and facilitates all components to drive the system. It has 4 layers and connects to the components via 32 standard pin-outs. This layout can be easily manufactured by PCB suppliers and allows for a grate range of flexibility to changes while achieving industry standard build quality. The Teensy micro-controller is soldered on a socket which allows to swap the micro-controller in case of a malfunction. Even-thou the micro-controller is integrated into the PCB board the on board micro-usb port remains functional and can be used for flashing or debugging of the software. The illustration shows a 3D rendering of the finished PCB layout. The two holes on the lower left

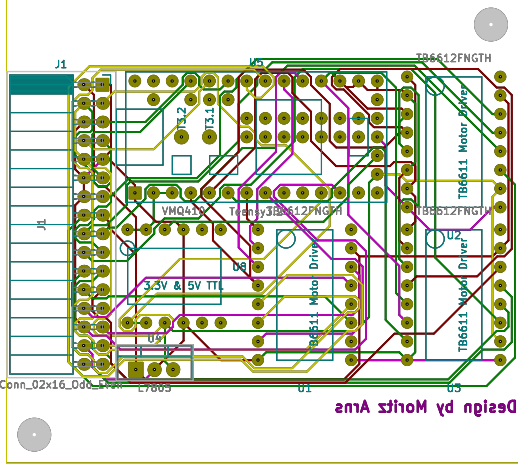


Figure 35: Electric circuitry on PCB Board

side and the upper right are for the attachment on the prototype. The schematics diagram of the electrical hardware can be found in the Appendix A.1.

5.2 Mechanical Components

This section will describe first describe all meaning full components of the design and allow for a detailed reconstruction of the mechanism. At first the introduced tactile sensors at the end of each landing leg are shown. Then the telescopic arm with its locking mechanism is illustrated as well as

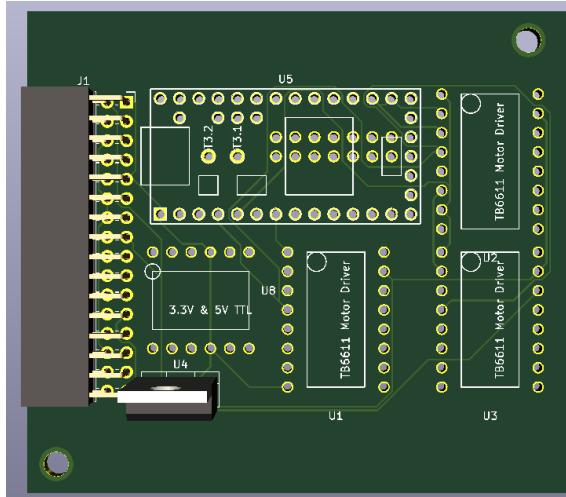


Figure 36: 3D rendering of PCB board

the centre locking mechanism to hold the design in place when in compact mode. It is shown how the mechanism is attached to the DJI Matrice 100 drone and finally an overview of the complete design is given. Additionally, to the core design of the Manipulander is an example for a functional extension of the Mechanism given.

5.2.1 Tactile Sensors

There are three tactile sensors in the Manipulander system, they are connected to each leg end and only used when the system is in Landing-Mode. To reach a stable landing position all three-landing foot need to be in contact to the ground. Hence, for the adaption to the landing surface, the information whether a leg has contact to the ground is necessary for the control system. Due to the uncertainty of the ground conditions there are several requirements to the sensing element. The most important are listed below:

- Adjustable response-force to neutralize soft or brittle surfaces
- Sensitive to forces from multiple directions
- Withstanding high impact forces

To satisfy the requirements a tactile sensor was designed. It is composed of a simple 2 axis sliding joystick which is in the centre of the inner drum of the sensor and used for the position feedback. Connecting to the control button of the sliding joystick is a tactile element which is hinged on a rotary axis. The rotary axis is spring loaded which centres the sliding joystick in its default position. Due to the circular shape of the tactile element every radial force during landing on the sensor is transferred to a transverse motion at the centered sensing element.

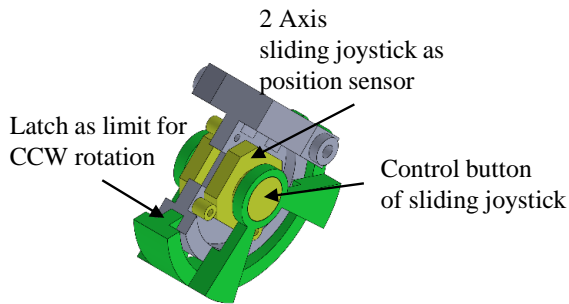


Figure 37: Tactile overview

To ensure that the ground is a solid landing surface a tactile landing mechanism is designed. A tactile sensor has the advantage that the sensor is physically in touch with the surface. This allows to get a rough estimate of the consistence of the surface. For instance, if the rotorcraft would land on a grassy field, the landing foot would compress the grass until it gives a basic resistance to the tactile sensor. This ensures that the landing leg has a firm ground to land on. A capacitor or optical landing sensor would feed back a stable landing position as soon as the landing gear becomes in contact to the ground. The tactile sensor of each leg is composed of a tactile element which is in contact to the landing surface. In the centre of the contact sensor is a 2 Axis sliding joystick which functions as position feedback. It is firmly attached to the inner drum of the textile sensor which is attached to the end of the Manipulander leg. Contact to the ground allows to exert a radial force from any positing of the half circle sensing element. The adjustable rotary is set to exert roughly 1N of force when a radial force is applied to the middle of the tactile element.

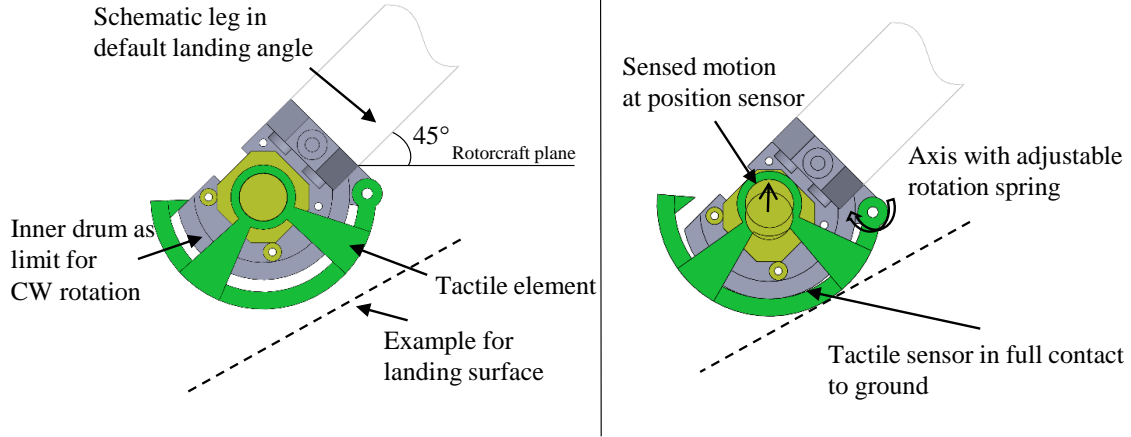


Figure 38: Tactile before and after landing

5.2.2 Prismatic Arms

A core element for the reconfiguration of the delta robot

are the telescopic arms. The telescopic elements are prismatic joints which allow to extend and retract limb

a. During the conversion from Compact Flight Mode to Landing mode, the actuation is driven by the main motors at θ_{1i} . Therefore the telescopic arm only needs to lock and unlock this motion and no linear unit to drive this motion is required. Further requirement to the telescopic mechanism are:

- Self-locking to reduce energy consumption
- Light weight
- Fast actuation
- High structural strength

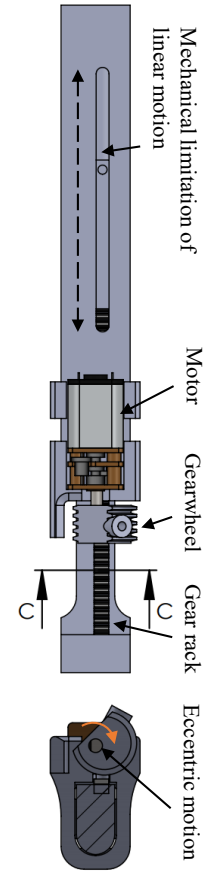


Figure 39: Locking mechanism of Prismatic legs

The figure on the right shows the developed mechanism.

The mechanism consists out of the following components. The telescopic unit which consists out of an outer part which stays fixed and an inner part. The inner sliding component of the mechanism has a gear rack on its top surface. The locking mechanism attached to the outer part, is a micro-gear motor with an eccentrically mounted gearwheel. This configuration allows for a locking of the linear motion in any given position. To ensure low energy consumption the locking of the motion needs to be self-locking such that the mechanism only requires energy during the locking and unlocking but not for keeping the system in a stationary position. To lock and unlock, the gearwheel has an eccentric shape which allows it to slide sideways into the gear rack geometrically locking the linear motion. This causes the gearwheel to be pushed into the gear rack which ensure that the teeth of the gearwheel slide into a position where teeth are interlocked. Further allows this motion for a clamping of the gearwheel into the gear rack which leads to a self-locking of the mechanism.

5.2.3 Centre Locking Mechanism

A crucial component of the mechanism is the centre locking mechanism. It is used to transfer the system from manipulation mode to compact flight mode. As a secondary function this mechanism locks the moving platform below which allows to keep the mechanism in this position without draining power from the energy supply. Figure 40 shows the mechanism before the moving platform is locked into the centre position. The system is composed of a winch located on the base platform, a locking frame below the base platform and a cone on the moving platform. When the system is in its manipulation mode, the cable length connecting moving platform and base platform is chosen to be long enough that the mechanism can reach any position without constraining its 3DOF. When the mechanism transforms from manipulation mode to compact mode, the moving platform is brought to a enteric position while the winch is activated and supports the mechanism to reach the centre position. The support of the winch is not necessary but can become very useful when

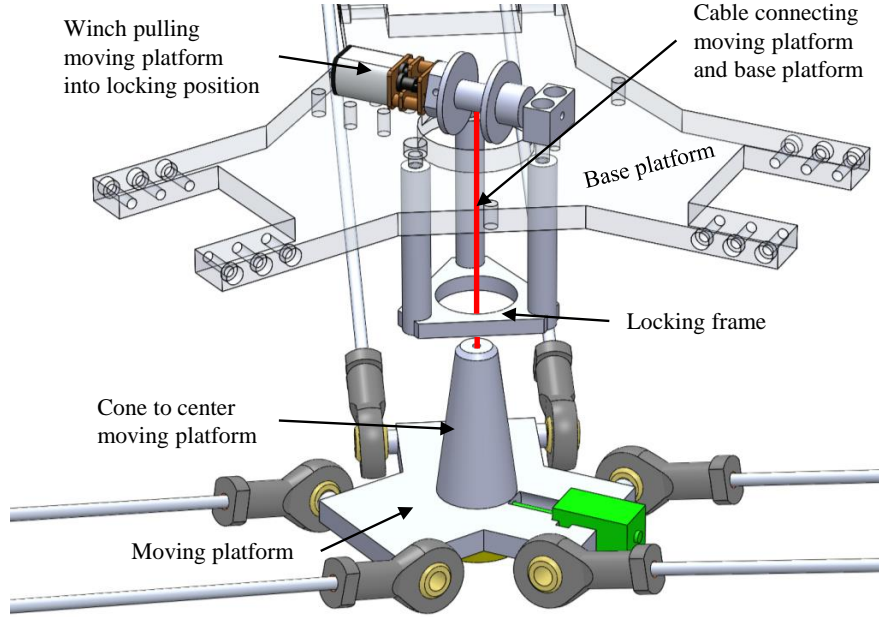


Figure 40: Centre locking mechanism to secure moving platform in Compact mode.

the mechanism is bringing heavy objects into the compact flight position since it is an operation close to the end of the workspace and a singularity. When the moving platform reaches the upper position, the cone in combination to the circular hole in the locking frame helps to centre the moving platform. The workspace calculations shown in Figure 10 are used to determine the height of the locking frame such that the moving platform never leaves the reachable workspace when in it is in the locked position. It is shown that for this specific mechanism the locking mechanism should be a minimum of -60 mm from the base plane. The interlocking of the cone with the locking frame secures the moving platform starting around -120 mm since the cone itself has 60 mm height and the interlocking starts therefore earlier. This makes the design compact while providing extra guidance for the moving platform in the close to singularity area. The moving platform has reached the centre locking position when the bottom of the locking frame is coincident with the moving platform. The winch now keeps the cable under tension which prevents a slipping out from this locked position. In this position the moving platform loses all of its 3DOF. The xy translational freedom is locked due to the concentric position of the cone and the hole. Motions in z directions are constrained by

the cable under tension which forces the moving platform in contact to the locking frame. To keep the system under tension the winch needs to have a gearbox with a sufficient reduction to prevent backdriveability. Alternatively, the winch can also stay under low power to make unwinding harder keeping the cable always under tension.

5.2.4 Completed design integrated into rotorcraft

A complete assembly of the DJI Matrice 100 drone and the Manipulander mechanism is shown in this section.



Figure 41: Mechanism in Compact flight mode transporting package.

The Manipulander mechanism is placed centrally below the rotorcraft and weights including battery and control 900 g and therefore allows to pick up payloads of up to 300 g (total payload 1200 g). Since this seems to be a big margin of the total payload capacity, it is important to mention that no weight optimization on the prototype have been done. As an obvious example are the links b of the four-bar parallel mechanism still made of stainless-steel rods. A simple switch in used materials like carbon fiber or aluminum would be a great significant improvement. Therefore, the total weight is not a meaningful criteria at this rate and since further weight improvements mainly described in the finite element investigation Section 3.7 need to be investigated.

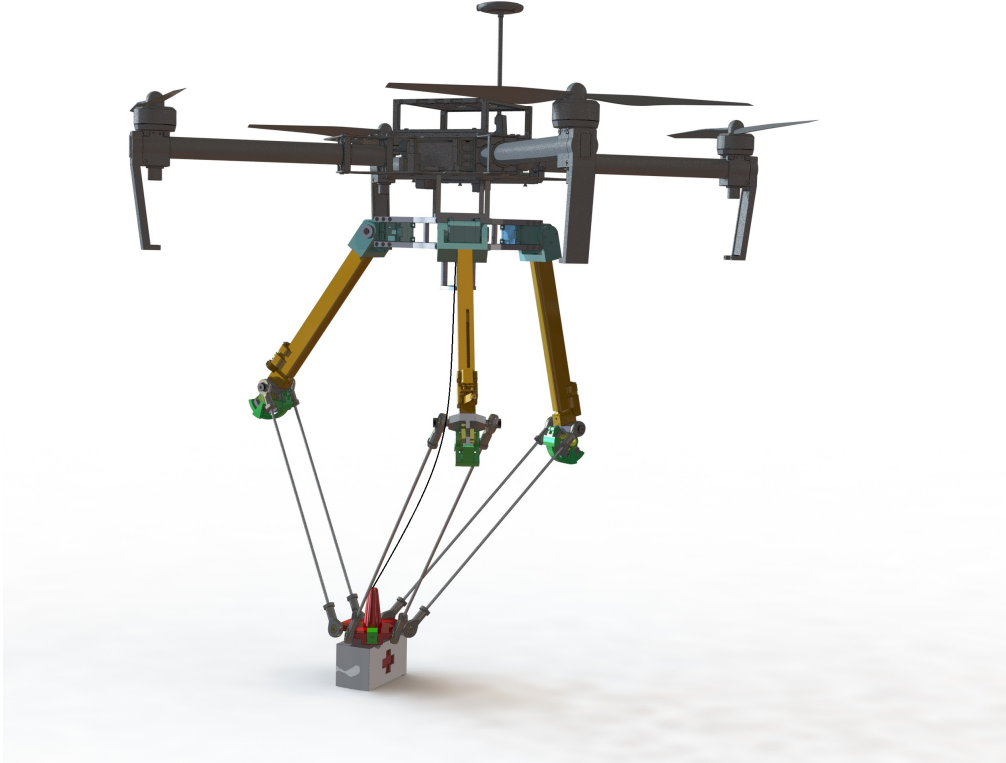


Figure 42: Mechanism in Manipulation mode picking up package.

When the mechanism was integrated into the DJI Matrice 100 drone it was not possible to attach it right below the main body since vertical extensions below each rotor would interfere with the ground. Therefore, the mechanism is offset by about 40 mm such that the landing gear, even when adopting to extremely uneven ground, always prevent damage to the delicate antenna components. Figure 41 shows a rendering of the complete system in the compact flight mode. In this configuration the legs are completely retracted, while the moving platform is fixed centrally below the base platform. Due to the mechanically locked mechanism it is possible to transport cargo, in this case a medical kit, for long distances without draining energy. The size of the rotorcraft system is not significantly larger compared to the UAV itself, which demonstrates how well the systems complement each other.

The circular shaped green ends at the end of each leg are the tactile ground sensors shown in Section 5.2.1. The motors for the actuation of the system are turquoise green and located at the



Figure 43: Landing on even ground with cargo attached to moving platform.

edges of the base platform. For the connection of the four-bar mechanism of link b and link a are stainless steel bars used, which connect over a IGUBAL® rod end bearings which represent the universal joints. The next rendering in Figure 42 shows the Manipulander in Manipulation mode where it is about to pick up a medical kit from the ground. It is using the 3DOF of the robotic gripper to maneuver the moving platform close to the medical kit to pick it up. The gripping mechanism to pick up the package is not designed since a gripping mechanism would need its own detailed investigation and is not part of this research. The robotic arm allows with its 3DOF maneuverability to compensate for the unstable and inaccurate positioning of the rotorcraft. This enables to pick up objects during flight. It is worth noticing that even-though the moving platform is almost at the end of its workspace the cable connecting base platform and moving platform has some slack, allowing the mechanism to reach any position in the workspace without getting constrained by cable tension. The next rendering in Figure 43 shows the Manipulander in its landing configuration.

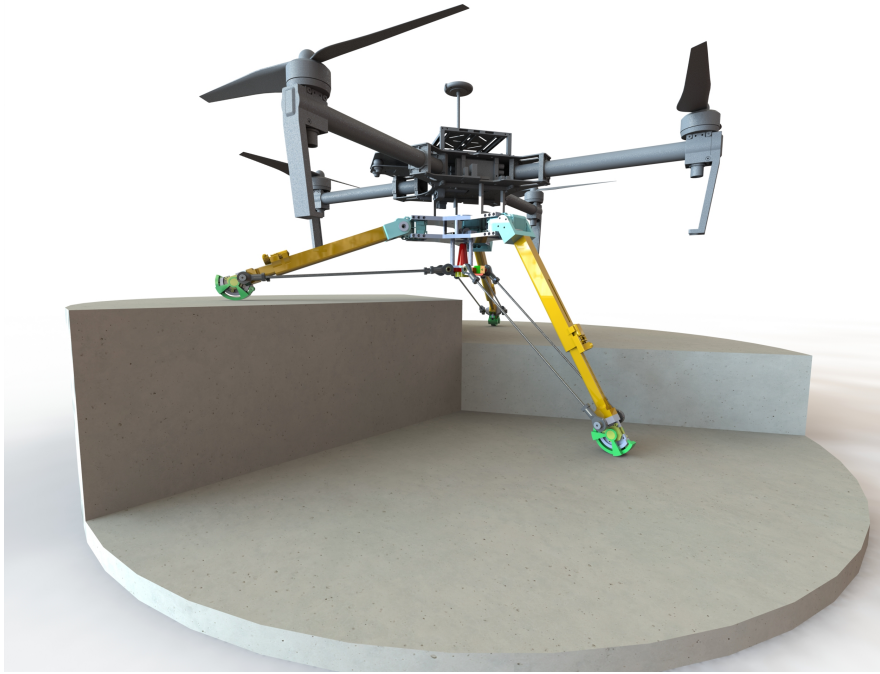


Figure 44: Mechanism landing on uneven ground.

The landing legs are rotated downwards, and the mechanism has come to a landing positng on a flat surface. When landing on a flat surface all legs are getting in contact to the ground almost at the same time and the mechanism does not need to adapt to the surface. Hence, the mechanism maintains most of its clearance below the base platform which allows to land on flat surfaces while transporting cargo. When the landing position is reached the sliding mechanism on each landing leg are locked and all active components of the system are turned off to prevent power drainage. Figure 44 shows the system in a second landing scene adapting to an extremely uneven surface. The uneven landing surface is simulated by a stair configuration with three different heights. In this final landing configuration, each landing leg has a different height. This demonstrates how the mechanism adapts to uneven surfaces while maintaining a horizontal position for the rotorcraft main body. The mechanism is able to adapt to slopes of up to 23° which is equivalent to objects of 225 mm height. A downside of a landing on uneven ground is that the clearance below the landing gear decreases which does not leave room to carry cargo.

5.2.5 Functional extension of Prototype

To illustrate some possible abilities and the versatility of the system, a functional extension was designed. For rotorcrafts it is often too time intensive or dangerous to land in order to pick up or drop-off cargo. Some companies in the delivery sector have found a way to avoid coming close to the ground with their rotorcrafts. Some of them use parachutes attached to their packages to drop off their cargo in mid-flight [56], other hover over the destination and use a cable to deploy the delivery without landing [57]. Since the current Manipulander design already includes a winch and cable to support the conversion between the different operation modes, it is logical to use this mechanism to deploy or pick up objects by tether. The result was the mechanism shown in Figure 45 on the right. When the mechanism is in its manipulation mode, a probe below the moving platform can be deployed. This would allow to pick up or deploy objects during flight without bringing the drone near the ground and enable a range of advantages.

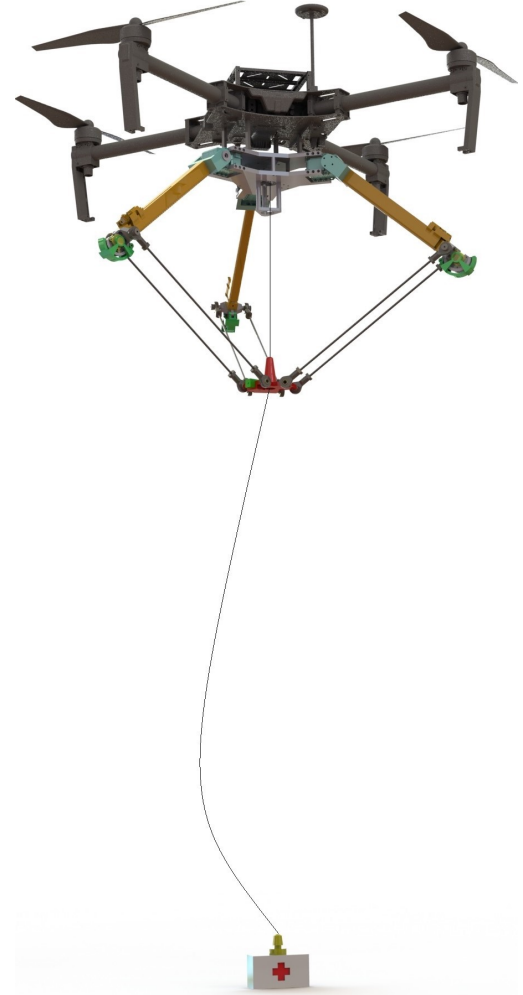


Figure 45: Functional extension allows to use cable and winch for transforming the mechanism to pick up and deliver cargo without landing.

- Faster pick up and drop off without landing
- Increase safety since rotorcraft does not get close to possible contact
- Access of areas where rotorcraft cannot get close to. (Forest fire...)

- Noise reduction due to higher flight position of rotorcraft during pick up and drop off

The developed mechanism is efficiently integrated into the moving platform. In this examples it only consist out of a cone attached to a cable which could potentially hold a gripping mechanism shown in Figure 46. When the mechanism is in manipulation mode and the probe gets deployed,

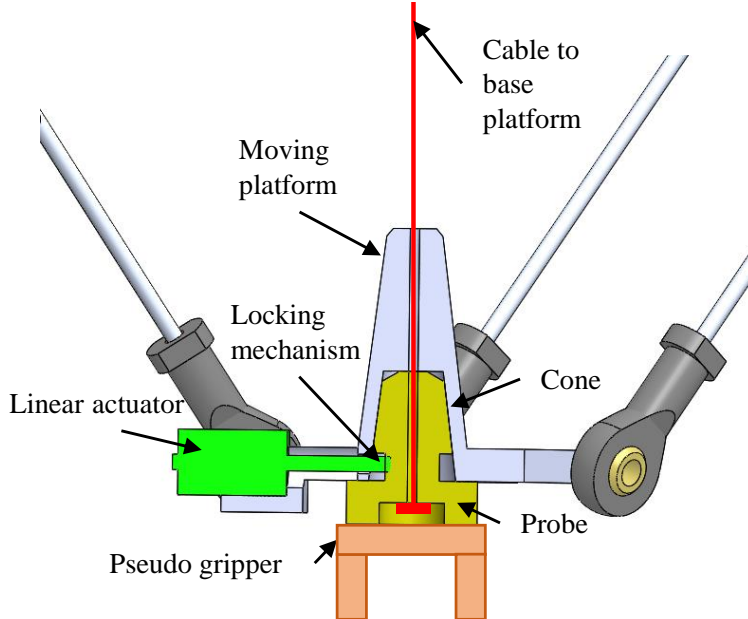


Figure 46: Detailed view of probe deploy and locking mechanism.

the linear actuator pulls the locking mechanism back. Then the winch at the base platform releases cable which lowers the probe downwards. As soon as the probe has left the docking position the linear actuator can be deactivated bringing it back into its spring-loaded closed position. When the probe is collected again the winch winds the cable until the probe reaches the moving platform. When the probe gets pulled inside the docking position its cone shape self-centres the mechanism and slips into the spring-loaded locking mechanism. This passive system allows to only use the linear actuator when the probe is released while the collecting of the probe does not require any actuation. When the probe is back in its locking mechanism the system is equal to the standard Manipulander system. This additional functionality can as shown be realised with minimal changes on the system which makes it a simple and interesting addition to the system.

5.2.6 Conclusion Extension of System

As described can this functional extension be realised with only minimal changes to the original system. However further investigations are needed to make this system practical. There is no solution presented on how the gripper at the probe would be supplied with power. Further, it is necessary to control the gripper position, which is at this point impossible since the probe can rotate and swing freely when deployed.

6 Platform Evaluation

In order to validate the functionality of the models a physical model is built to test the practicality and reliable of the system. At first a test stand is used to determine the interaction between the mechanism and the rotorcraft during landing. Then the mechanism was attached to a DJI matrice 100 drone to perform free flight experiments which tested the functionality and robustness of the system.

6.1 Interaction Forces during Adaptive Landing

In this section the developed control for the adaptive landing is evaluated. The key objective of the control design 4.2 is to minimize the reaction torque on the rotorcraft platform. To validate the effectiveness a test setup is built to simulate a landing on uneven terrain while all reaction torques between Manipulander and rotorcraft are recorded. The test stand uses a six-axis Force Torque sensor form Robotous (RFT44-SB01) which connects the Manipulander to the lower parts of the forklift. The forklift is then used to lower the Mechanism with a constant speed of 0.325m/s towards the ground. Solid blocks of different height are used to simulate the incline of rough terrain. This allowed to quickly change the ground conditions for each landing point. The ability to construct and control all factors of a landing allows to validate the effectiveness of the system in the field. For the test are four different landing setups chosen which proof the concept of the landing mode control. The setup is shown in Figure 47.

- Trail 1: Only leg 1 has contact to the ground.
- Trail 2: Only leg 2 has contact to the ground.
- Trail 3: Initial contact with leg 1 8cm delayed contact with leg 2.
- Trail 4: Leg 1 and leg 2 have simultaneously contact to the ground.

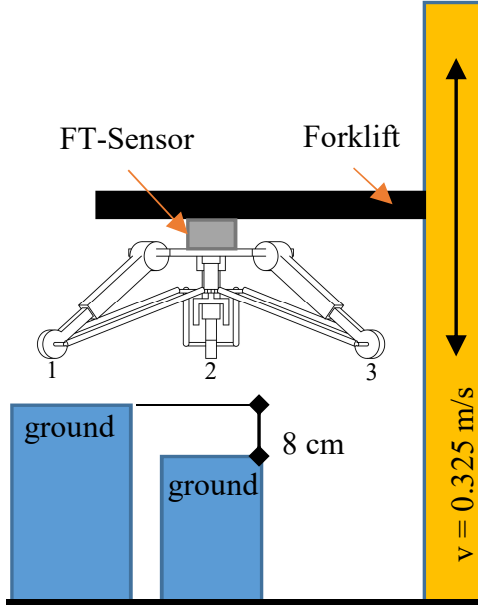


Figure 47: Manipulander attached to Forklift, illustrating setup for Trail 3 with two different heights.

It is important to mention that the third leg is never in ground contact. This is necessary since this investigation tries to capture the reaction torque on the platform during the landing process. As soon as the third leg would touch the ground the adaptive landing stops and the landing gear is locked in position. Hence, the third leg will always remain without ground contact and the reaction torque between landing gear and rotorcraft after a completed landing process is excluded in this test. During the test the torque in x and y axis and the force in the z axis were recorded. Out of those data sets were three values generated. The torque values in x and y axis where used to calculate the resulting torque magnitude on the platform. The resulting torque magnitude is calculated by $\sqrt{(\tau_x^2 + \tau_y^2)}$ and represents the magnitude of the torque vector on the rotorcraft platform. Further was the direction angle of the total torque vector on the rotorcraft is calculated with $\epsilon = \arctan\left(\frac{\tau_y}{\tau_x}\right)$. The angle describes the position of the resulting torque vector in the xy-plane. Additionally, is the force in z recorded to get a complete picture of the interaction between rotorcraft and Mainpulander.

Total Torque & Torque Angle:

Figure 48 shows the results of the four different test trails. Tail 1 and Trail 2 show the interaction

of a single leg with the ground. The resulting torque is in both cases almost identical with 1.7Nm as a peak. The predefined limit τ_{max} of the motor controller was set for this prototype to 2 Nm where inaccuracy of the used motor controller explains the error of 0.3 Nm. The torque angle ϵ on the other side shifts about 120° which is equivalent to the physical spacing between the legs shown in Figure 33. In Trial 3 the Total Torque on the platform is similar to the cases with only one leg in contact to the ground. Interesting is to observe the behaviour of the torque angle after the 2nd leg gets in contact to the ground. The ϵ shifts from roughly -55° to 5° as soon as the second leg is in contact to the ground. The last trial shows the instance of leg 1 and leg 2 getting in contact at the same time. The Total Torque peaks again at 1.7Nm while the torque angle is around 5° similar to the angle measurements after the second leg had contact to the ground in Trial 3. The data from

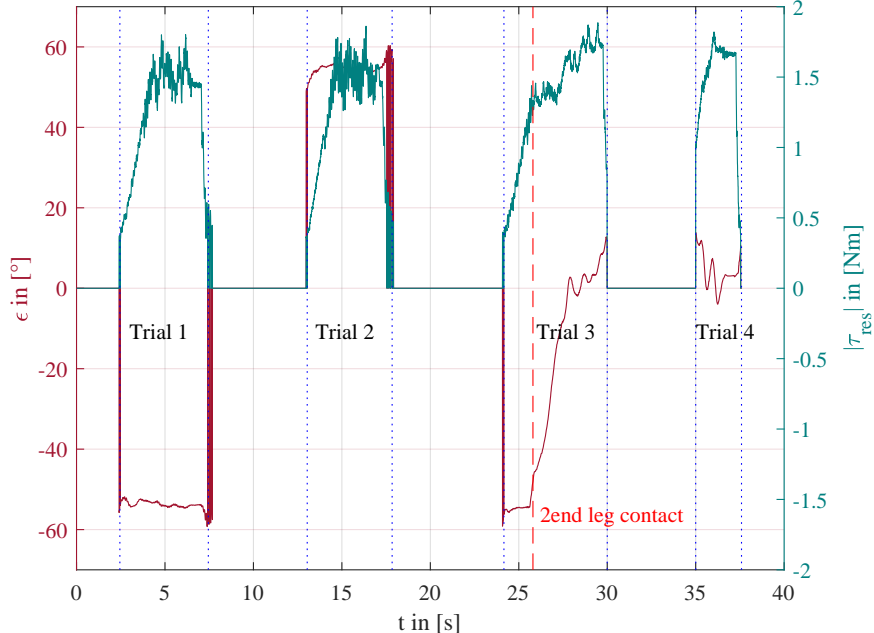


Figure 48: Experimental Results of Direction of Torque on Platform and Total Torque on Platform during four different landing trials.

the Total Torque and the Torque Angle suggests that the magnitude of the torque is not bigger whether there are 1 or 2 legs in contact to the ground. Further it has been shown that the Torque Angle on the platform shifts about 60° when the legs get in ground contact at different moments

Force Z-Axis & Total Torque:

The data for Figure 49 is from the same trails as shown in Figure 48 but shows the forces in the Z-Axis while the $|\tau_{res}|$ on the platform is shown again as visual reference. Trail 1 and Trail 2 show an almost identical behaviour. The Force in Z-Axis reaches about 6 N in both cases. Trail 3 shows a different behaviour, before the second leg is in contact the force reaches again 6N, but as soon as the second leg is in contact the Force in Z doubles to about 12N. A similar behaviour is seen in Trail 4 where the force reaches almost immediately 12N. The measured data shows that while the

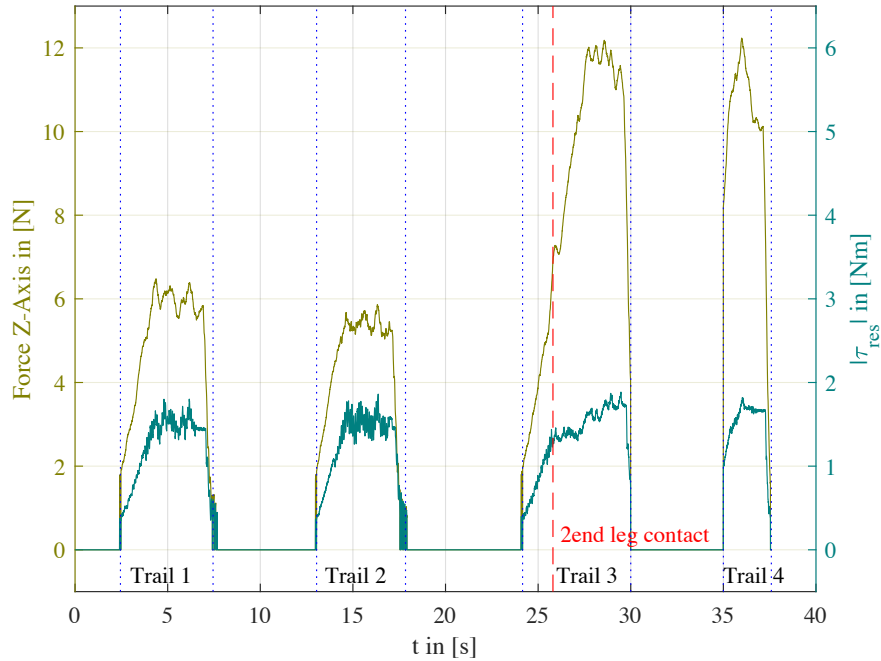


Figure 49: Experimental Results of Force in Z-Axis on Platform and Direction of Torque on Platform during four different landing trails.

total torque on the platform stays constant in all scenarios the force in z increases when more than 1 leg is in contact to the ground.

6.1.1 Conclusion Adaptive Landing Control on test-stand

The results from experimental validation of the self-leveled landing control show that the control concept deliverers the expected results. The maximum torque on the platform is limited by the

torque limit of the individual leg while the force to push the landing onto the ground increases with every leg in contact to the ground. This simple relationship between maximum torque on the rotorcraft platform and torque limit on each motor allows for an easy adaptation to different rotorcraft models.

6.2 Free Flight Experiments

The prototype is tested on the DJI Matrice 100 drone and all operation modes, Compact retracted mode, Landing Mode and Manipulation mode, where successfully demonstrated. To protect the drone from damage the original landing gear studs (located below each rotor) were not removed from the drone. In case of a malfunction of the system they would have prevented damage to the system. In Picture *a*) the mechanism is in its compact mode which would be used during cruise of the rotorcraft. Due to the mechanically locked position of the mechanism all motors are deactivated, and the power consumption of the system is only caused by the microcontroller and the Bluetooth connection. In *b*) the mechanism is in its manipulation mode which performs equivalent to a well-established delta robot. Since the main motors are required for the control of the moving platform this mode is energy intensive even without manipulating payload. In *c*) the mechanism is preparing for landing. The legs are fully extended, and the motor generates a minimum torque to dampen the landing. Due to the constant feedback and the generated torque to dampen the landing this mode requires a moderate amount of energy. In *d*) the mechanism has adapted to the landing surface of 22° while all locks on the legs are locked. Similar to *a*) this mode requires a minimum amount of energy. It is worth noticing the level on top of the drone illustrating the horizontal positing of the drone main body. From this position the drone is able to start with ease. The best impression offers the accompanying video “Delta Manipulander - 3DOF Manipulation and Adaptive Landing in One System” which can be found in the Appendix A.2.



a) Retracted during flight



b) Manipulation Mode



c) Landing Mode



d) Surface Adaption on 22° slope

Figure 50: Prototype demonstrating different operation modes

6.3 Conclusion of Free Flight Experiments

With this prototype the dual-functioning rotorcraft undercarriage as a re-configurable delta robot was fully rendered. All operation modes were repeatably successfully reached and the functionality of the system was demonstrated. The system was reliable and the pickup of objects without the use of advanced control mechanism was possible. Additionally was the adaption to uneven surfaces successfully demonstrated. Even-though the system was able to confidently demonstrate its abilities, it was noticed that the dual-functioning of the system has a major drawback. The operation modes of the systems are interconnected which leads to the problem that a failure of one system triggers the failure of the second function. This drastically reduces the reliability of the system. Since a failure of the Manipulander would affect the landing gear as a critical component a detailed investigation

of this problem in future research is recommended. Further areas of improvement were identified and described below:

Manipulation Mode

There are a number of limitations that need to be noted. In this stage of the development the control of the Manipulation mode functions via input of xyz coordinates. This makes it very difficult to dynamically control the gripper or to pick up objects during flight. A control using a joystick as input would be recommended for future research. Additional to this control would it be useful to have an automatized camera guided gripping system where a camera guides the gripper to the object location. Furthermore, since the Manipulator control and the drone control operate independently, fast motion of the moving platform can destabilize the drone flight. Therefore, a feed-forward controller combining moving platform motion and drone flight would need to be developed.

Landing Mode

When the mechanism lands on a very steep surface the space below the landing gear gets limited and collision of the object and the ground becomes possible. The size of the cargo below the platform limits the adaption capabilities of the landing gear which is a problem since it is hard to estimate how much space is needed to adopt to the surface. Therefore, landing on uneven surfaces with cargo is not recommended since it is in the current version impossible to predict how much clearance will remain after landing on an uneven ground. A new version optimized for landing with cargo on uneven surfaces could interesting to develop.

6.4 Comprehensive comparison of State-of-the-Art Systems and Manipulander

Since the system is a state-of-the-art system, it is important to compare it to existing solutions. The Manipulander combines a 3DOF robotic manipulator with an adaptive landing gear. Since the literature review has not found any system combining these two capabilities this section will first compare the system with pure Aerial Manipulators and then compare it to pure adaptive landing systems. A decision matrix is used to rate and compare the systems against each other. Since it is not possible to get detailed information about the systems specifications the categories are chosen to be relatively broad and a justification is only made based on best knowledge of the author.

6.4.1 Aerial Manipulators

Three prominent examples of aerial manipulation are chosen to be compared to the Manipulander system where each of them covers a different approach to perform aerial manipulation. All systems are shown in Figure 51. System b) is the Manipulander, System a) is a delta robot attached to a drone from [34] which is representing a parallel robotic solution. System c) represents a novel idea of using a gripper attached to an origami arm from [29] to control objects in great depth. System d) is a 7DOF KUKA robot attached to a helicopter from [26] representing a classic serial robot approach. Six criteria are introduced to rate each system's overall performance. The first criterion is weight, which evaluates the number of actuators and the complexity of the structural design. The importance factor for the weight category is with 5/5 the maximum since a heavy actuator has many drawbacks for aerial applications. The second factor is the reliability of the system. It has a relative high rating since malfunctions of the manipulation system can lead to a crash of the entire system. However, since not every failure of the manipulator leads to a crash it does not get the absolute highest rating with 4/5. The next criteria is the DOF or degrees of freedom of the manipulator. A higher degree of freedom allows for greater versatility in the

actuation and a possible broader range of applicants. The importance factor is set to be 3/5, since it is highly depending on the application. The workspace is rated by volume where a greater volume achieves a higher rating. It has the importance of 3/5 similar to the DOF. Another criterion rates the ability of the manipulator to disturb the rotorcrafts flight behaviour. This criterion is given a middle importance of 3/5 since it is hard to compare, and different control methods cannot be evaluated. At last, the energy consumption of the system is rated. A low energy consumption of the manipulator allows for longer operation times. Since the manipulator is most likely only in use for very short periods this category gets a fairly low rating with 2/5. Figure 51 shows an overview of the systems and their rating in each category. In following are the given ratings explained and justified. Starting with the least important criteria the energy consumption, the serial arm picture

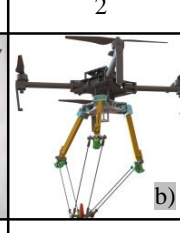
Criteria	Importance Factor (1-5)	1	2	3	4
		 a)	 b)	 c)	 d)
Weight	5	5	4	4	2
Reliability	4	3	2	3	2
DOF	3	3	3	2	5
Workspace	3	3	3	4	4
Disturbance of Rotorcraft	3	3	3	3	2
Energy Consumption	2	3	3	4	1
Sum	Max (100)	73/100 73%	64/100 64%	61/100 61%	53/100 53%

Figure 51: Comparison between different aerial manipulation solutions.

d) is rated with 1 the lowest, while the other solutions perform higher. To keep the manipulator under control during flight it is necessary to control the motion of the arm. Therefore, has the serial arm with seven actuators by far the highest energy consumption even when it is not actively used.

In contrast allows the origami gripper with only one main actuator to deactivate the motor at any time which keeps the energy use to a minimum. Another category where solution d) performs the worst is the disturbance of the rotorcrafts flight. Since the actuators are along the serial arm, the great moving masses of the serial arm can easily disturb the rotorcraft flight. Solution c) performs with its robotic arm going straight down in a much better manner since the masses are always below the centre of gravity of the rotorcraft. Solution a) and b) perform also better since parallel systems have their actuators on the base platform which keeps the masses close to the centre of the rotorcraft. A different situation can be seen when it comes to workspace of the system. The serial arm outperforms the other solutions, only the origami arm c) can perform equally well. Beside the workspace is also the DOF of the robotic arm important. The serial arm clearly preforms here the best and gets a perfect mark while the origami gripper shows its big disadvantage of only being able to grip right below the rotorcraft. Besides those mechanical characteristic's reliability is extremely relevant in aeronautics since a malfunction can cause a crash landing of the rotorcraft. Therefore, systems that are redundant or have less components which can fail have an advantage over complex systems. This shows a disadvantage of the Manipulander system. The dual-functioning as a landing gear and manipulator makes the mechanism more complex and allows more chances to fail. This gives the system the lowest score in its class in terms of reliability. The most important criteria for a robotic arm for aerial manipulation is the weight and is therefore weighted with 5 out of 5 in the importance scalar. The serial arm is here with its many actuated joints the bottom of the list while the simple delta robot reaches the highest score since it uses less actuator and can rely on a light weight structure. Calculating the weight result of every solution the serial arm scores the worst with 53%. The best solution for aerial manipulation is the delta robot which reaches 73%. The Manipulander is closely followed by the origami gripper the second place since it lost mostly in the reliability section.

6.4.2 Adaptive Landing Gears

After the literature review did not unveil a mechanism that can perform as adaptive landing gear and aerial manipulation in one device, this section compares the mechanism to the systems performing as pure adaptive landing gears. Figure 52 shows a decision matrix with the adaptive landing systems. System e) shows a tripod landing gear system developed from NASA. It was proposed for lunar coring explorations but has never been in service [58]. Figure f) shows the Manipulander landing on a slope while Figure g) shows the DARPA landing gear [5]. The last system h) is developed by the ETH University which is designed to help rescue helicopter to land in rough terrain [21]. To evaluate the ability of the different systems 4 criteria are introduced. The first criterion is the energy consumption, which is rated with 3/5 importance for the system. Next in the list is the ability to compensate for angles in the terrain. Since this is the core premise of the system it is also rated with 3/5 since it is very specific for the application. A criterion that is important for all different scenarios is reliability. Since the system is fundamental to the function of the rotorcraft malfunctions cannot be accepted and is rated with 5/5. The last criterion is the weight which is also very important for any aerial application and is again rated with 5/5. In the following are the found ratings of each system justified.

At first, we refer to the energy consumption criteria. Here the worst in its class are the solutions from DARPA g) and ETH h) where the motors are constantly powered to keep the landing legs in position even during cruise. The best rating has system e) 5/5 since it is passive and does not require any energy. In the next category “Angle of Compensation” all four systems perform relatively similar, even-though the tripod solution e), f) tends to be more suitable to adapt to uneven ground since they can easier find a stable landing position. A three-leg design compared to a four-leg design will never have a leg not in contact to the ground and will therefore never be in a shaky position, this can be imagined to be similar to a three-legged table. More important is again

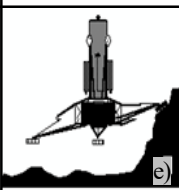
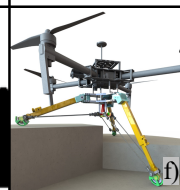
	Importance Factor (1-5)	1	2	3	4
Criteria					
Weight	5	4	3	2	1
Reliability	5	3	2	3	3
Angle of Compensation	3	5	5	4	4
Energy Consumption	3	5	4	2	1
Sum	Max (80)	65/80 81%	52/80 70%	43/80 57%	35/80 47%

Figure 52: Comparison between different adaptive landing gear solutions.

the reliability of the system. The weakest system is here the Manipulander f) since it dual-functions as manipulator and landing gear. As soon as one system would fail the other system would not be available anymore. This gives the system a rating of 2/5. The highest reliability has the passive system e) which eliminates the failure of actuators or sensors. The last an also important criteria is the weight of the system. The heaviest system is system h) which is caused by the heavy ball-screw mechanism followed by system g) which has a complex and heavy structure. The tripod structures in e) and f) are relatively light weight and perform well even-though the dual-functioning of the Manipulander adds additional weight compared to version e).

6.4.3 Conclusion of Comprehensive Comparison

After comparing the Manipulander to state-of-the-art aerial manipulation systems and adaptive landing gears, it is shown that the developed Manipulander performance relatively well in both of its configurations. The comprehensive comparison with a decision matrix shows that the Manipulander scores second place in aerial manipulation solutions. The same result is shown when comparing it

against state-of-the-art adaptive landing gear solutions. The system scores here again second place where the best solution was a passive tripod adaptive landing gear. This comparison gives a very interesting insights about the systems capabilities. The best performing systems for landing was a tripod solution and for manipulation a delta robot. One has to notice that when the Manipulander is in any of its mods, it resembles a tripod landing gear or a delta manipulator. Each system on its own was found to be the best system available for the task. Now the question arises why the Manipulander performers worse than the best solution even-though it practically represents the same approach? For aerial application in general weight, reliability, and energy consumption are the most important factors. Since a dual-functioning system necessarily increases the complexity, weight, reliability and energy consumption are impaired. This is the main reason why the dual(multi)-functioning system is outperformed by a single purpose approach. Nevertheless, this investigation also shows that the dual-functioning system uses the correct architectures and confirms that it closes a gap which has been left out by current research. The system is currently state of the art since it is the only system that combines adaptive landing and manipulation and is the best choice for applications where both functionalities are required.

7 Application

In the following are several possible applications for the Manipulander system presented. The goal is to identify possible application which could help future research to continue this project. Applications are selected which require the both functionalities Manipulation and Adaptive landing which can be summarized as:

- 3DOF Manipulation and transport of objects
- Reliable landing in any terrain

7.1 Search and Rescue

After natural disaster, the Manipulander can be used to support rescue forces. In the event of a crisis like earthquakes, floods or big forest fire, transportation of goods in need is mostly limited due to the inaccessibility of roads. Unmanned aerial vehicles can help in a number of ways to support first responders. Additionally to being helpful in giving an visual assessment of the situation they can supply them with medications, vaccines, blood derivatives [59], tools or other equipment. As an example, the Manipulander can autonomously pick up supplies from a storage centre and delivery them precisely to the impacted area. The adaptive landing gear allows the system to operate even if there are no prepared landing sites available which greatly increases the flexibility of the UAV system.

A second scenario for the use of the Manipulander in a natural disaster would be to deploy sensors and communication systems in the impacted area. Natural disaster not just destroy buildings and bridges it also wipes out the entire telecommunication in the area which is crucial for an efficient search and rescue operation and helps people to organize themselves. To establish these crustal infrastructure as fast as possible mobile sensors stations and telecommunication systems need to be

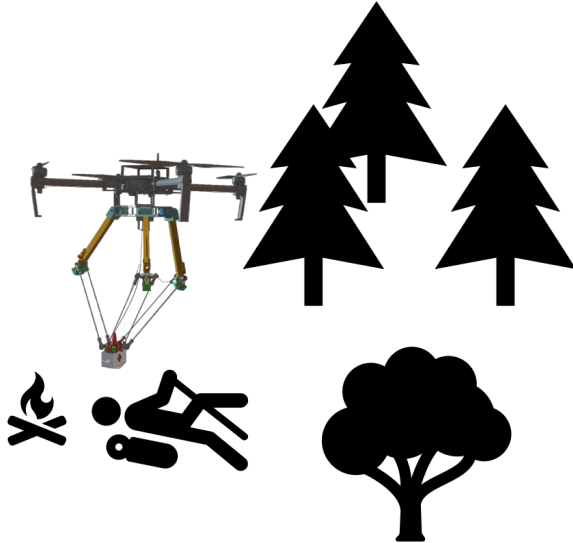


Figure 53: Manipulander providing medical kit to insured hiker.

temporarily deployed in the area [60]. The Manipulander can bring, with its robotic arm system, telecommunication systems to the impacted area and precisely position them. Once the original telecommunication is recovered the system can pick up the deployed system and shift them to a new area.

7.2 Military and Law Enforcement

In the military drones are used for decades to conduct intelligence about conflict areas. The first unmanned aerial vehicle was invented in 1916, the military started to exploit its use for intelligence after the Vietnam war. They equipped with video camera which transmitted the signal to a base camp [61]. From here, development quickly picked up and UAVs nowadays core part of many military operations. The Manipulander could be used as a universal supply drone. In combat, the Manipulander could be used to supply troops directly on the front-line with ammunition or medical equipment. Further it would be possible to use the gripper to disarm mines or bomb traps. Some attempts have been shown here [38]. Since the system can land on any terrain, it would allow to position the drone for example on rooftops to be used as "sleeping" surveillance drone. This

approach has been tested before which can be seen in several patent filings [62, 63].

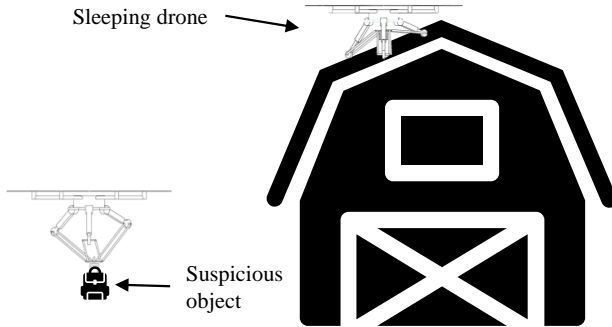


Figure 54: Sleeping drone collecting surveillance information, and disarming suspicious objects.

7.3 Mining

The mining industry is operating mostly in inaccessible areas with many hazards for workers.

Environmental standards are additionally becoming more important especially in open pit mines.

For example water samples around and within the mining area have to be constantly collected [64]. The robotic gripper of the Manipulator could be used to collect precisely those samples and bring them back to the base station and would avoid humans to get into dangerous areas. The adaptive landing gear allows the system to land within the mining area and making its operation more flexible.

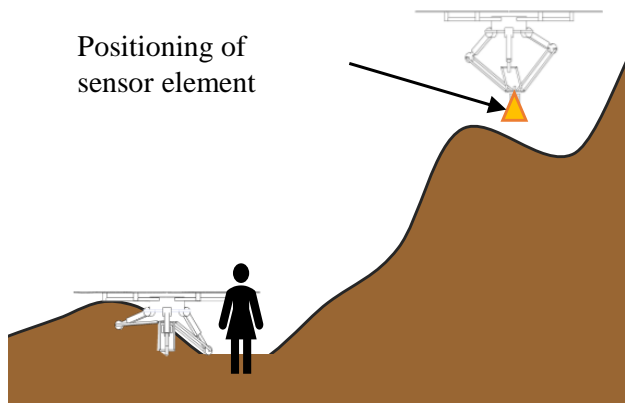


Figure 55: Manipulander deploys sensor elements in mining pit, and can land for change of equipment in the mining field.

7.4 Space

The Manipulander could also be interesting for space exploration. Probes on the moon, mars, or on asteroids could use the attachment to explore and safely land similar to the example shown in [65]. NASA announced in May 2018 that a “robocraft” helicopter would be used in the Mars 2020 mission to find out whether there has ever been life on Mars.



Figure 56: Artist’s conception of the autonomous, drone-like Mars Helicopter, which will be sent to Mars along with the 2020 rover. (from [3])

The rotorcraft will serve as a scout for the rover, gathering data about the planet’s terrain and surveying areas the rover cannot reach. In future missions a space probe equipped with the manipulander can use its gripping mechanism to pick up samples in otherwise unreachable areas. Since the terrain is not predictable the mission would need an adaptive landing gear to allow for safe landing. The Manipulander would therefore be the ideal system since it integrates an adaptive landing gear and provides a robotic arm solution which presents a lightweight dual-functioning system.

7.5 Delivery

Big retailers explore the option to use drone for their delivery services. Amazon is having proposed a delivery solution back in 2015 but a serious roll out is up to this date pending. More serious

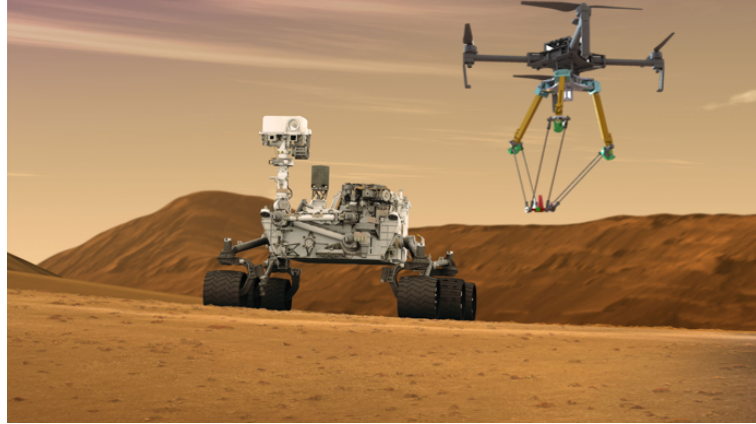


Figure 57: Mock image illustrating Manipulander in fictional Mars mission. (changed from [4])

is the use to deliver health care goods in developing continuities or areas with less density like northern Canada. Currently delivery services avoid the landing but deploy their delivery on a cable or use little para-shoots on the package to softly deliver the package at the destination. This kind of drone delivery services are very efficient when it comes to deliver but they are unable to pick parcels up in order to do return shipments. Examples for this type of delivery are the German company Wingcopter and the American company Zipline [66]. The Manipulander could here be used to enable return flights. The robotic gripper is ideal to pick up packages and transport them to a location. The adaptive landing gear also enables greater flexibility since the system can land reliably on uneven ground.

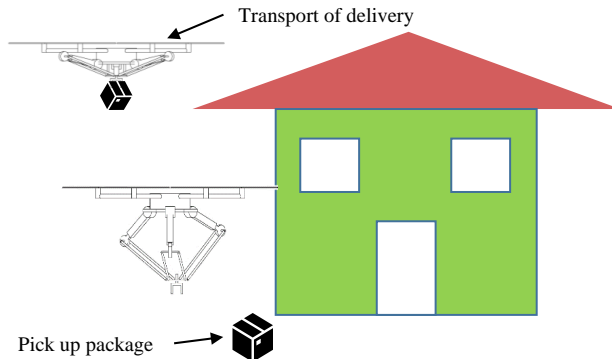


Figure 58: Manipulander delivers package to the doorstep.

8 Conclusion

The presented work shows a novel hybrid landing gear for rotorcrafts which can pick up, transport, and manipulate objects as well as perform adaptive landings on uneven terrain.

The derived design guideline allow to easily fit the Manipulander mechanism to any given rotorcraft dimension. In this paper the mechanism was integrated into a DJI Matrice 100 rotorcraft, where the following performance characteristics were achieved: Since the used UAV has about 1.2kg of payload capacity the Manipulander had a total weight of 0.9kg allowing to the pickup and transport of objects of at least 300g. Further the manipulator demonstrated an accuracy of about 1cm with a velocity of 30cm/s, enabling fast and precise pick up and manipulation of objects. When the mechanism is in landing gear configuration it absorbs impacts from free falls of up to 0.4m and compensates inclines of up to 23°.

System Characteristics:	
Overall:	
Safe conversion between Manipulator & Landing Gear	✓
Low energy consumption	✓
Weight of Manipulander	0.9Kg
Manipulator:	
Three degrees-of-free-dome	✓
Absolute accuracy	1cm
Velocity of moving platform	30cm/s
Adaptive Landing Gear:	
Landing Gear retractable	✓
Adoption to uneven terrain	23°
Withstanding of free fall	0.4m

This thesis presents a complete study of the inverse and forward kinematics where the singularities are presented. From the resulting workspace calculations, a straight forward guideline is derived which allows to replicate the Manipulander design for any rotorcraft dimension. This method ensures that the mechanism can operate without reaching singularities when converting between the operation modes. For the actuation of the mechanism, two control strategies are developed, con-

trolling the adaptive landing and 3DOF motions of the manipulation mode. For the manipulation was a 3th order smooth trajectory implemented. A control which limits the torque on the rotorcraft during the landing was developed and can be easily integrated into various rotorcraft types. Following the development and simulation of a control strategy, a structural finite element analysis was conducted approving the systems robustness and accrediting weight improvement potential. During the prototype construction of the Manipulander, all system hardware components were identified, and a custom PCB circuit board was developed. During the physical prototype construction, a tactile ground contact sensor was developed, as well as a centre locking mechanism which enables efficient reconfiguration of the mechanism. After design and testing of the circuitry, the control was successfully deployed on a M4-Cortex Microprocessor written in C++. Following this, tests to evaluate the platform were conducted. A test-stand which allowed to measure the interaction between the landing gear and the rotorcraft showed the effectiveness of the designed adaptive landing gear control. Free Flight Experiments additionally demonstrated the systems full functionality. All operation modes were demonstrated as well as the pick-up and transport of an object. The adaptive landing repeatably demonstrated compensations to slopes of up to 23°. Nonetheless concerns about the reliability of the system arose since a failure in one system causes a domino-effect, disabling both landing and manipulation. This was identified as the most critical drawback of the system.

8.1 Research Contributions:

The newly defined mechanism combines a delta manipulator with an adaptive tripod landing gear which can convert into three operation modes. Each operation mode holds its specific advantages for aerial applications. The Adaptive Landing Gear Configuration allows to land on uneven surfaces with a stable tripod geometry. When converted to the Manipulation configuration the system shows a large uninterrupted workspace with high velocities and at the same time low moving masses

reducing the disturbance of the rotor-craft flight behaviour. During cruise the mechanism folds up, reducing the aerodynamic drag and allows to hold payload without further energy consumption. The thesis presents a design guideline which can be used to quickly develop new systems on different rotorcraft types. An analysis of state-of-the-art systems for both aerial manipulation and adaptive landing was conducted, and the results compared to the Manipulander. This analysis showed that the dual-functioning system is a competitive system for either of its core functionality. Its versatility offering a better feature-to-complexity ratio which makes it the best choice on the market when adaptive landing and aerial manipulation is needed. This proved that the system could enable UAV technology to a new range of applications. Several possible applications were identified while the main focus of further research should be on the reliability of the system.

9 Future Work

This section will indicate possible areas for future research on this integrated system.

9.1 Reliability

The reliability of the system is a curricula factor of any aerial system and has therefore highest priority. Even-though the system is deployed on an unmanned vehicle failures critical errors could potentially harm third parties. Since the integrated system has the function of manipulation and adaptive landing, a failure in one system causes the failure of all systems. A future research should conduct a failure analysis outlining the main weak-points of the system. Failure Modes Effects Analysis (FMEA) or Fault Tree Analysis (FTA) [67] are a good starting point for this task. Derived from this analysis, design changes which lead to an improved reliability of the system should be implemented or suggested.

9.2 Dynamic Control of Manipulation Mode

The proposed motion control of the mechanism only allows for position control of the moving platform. The motion control of the manipulator is in this independent from the rotorcraft controller. To further minimize the disturbance of the rotorcraft a dynamic control would need to be introduced. The controller would predict occurring torques due to the moving platform motion and feed them to the rotorcraft flight controller. A good base for this work could be found in [68] where a feed forward controller for a Delta-robot attached to a drone is presented.

9.3 Development of a standard Adaptive Landing Control benchmark

To develop a functioning system, it is always important to define a benchmark which allows to compare the incremental progress between versions or even between different models. Many areas

of development have standardized tests which define the functionality of a device. Until now, there is no standardised method presented to validate the effectiveness of an adaptive landing gear system for rotorcrafts. A detailed description of a test setup would allow to compare different systems approaches efficiently. This would help to identify and rate adaptive landing systems, leading to a more efficient innovation process. Form the experience of the development on the presented adaptive landing gear a standard benchmark would need to include at least the following objectives:

- Torques on rotor-craft during landing
- Maximum possible angle of surface adoption
- Angle error after adaptive landing
- Vertical and horizontal speed of landing

Future research could use these specifications as inspiration for a detailed adaptive landing gear standard test.

9.4 Dynamic control of Adaptive Landing

A simple adaptive landing gear control is presented in this paper. To further enhance the capabilities of the system it would be necessary to design a dynamic landing gear control. In this paper the landing controller operates independent from the rotorcraft controller. A development of a new dynamic landing gear controller could feed the occurring torques during the landing sequence into the rotorcraft controller. This could help to stabilize the horizontal positing since the torques could be better compensated by the flight controller. Further would it be interesting to develop an adaptive landing gear which would allow to stabilize the landing for moving landing surfaces like rocking boats on rough sea.

9.5 Weight optimization and scaling

Since the highest structural loads to the Manipulander occur during the adaptive landing phase a new version could be designed as light as a regular adaptive landing gear. This could be the motivation to develop a new weight optimized prototype. After development a comprehensive weight comparison to current system could be presented. Further to this design study, the scalability of the system could be investigated. A large and a small version could be designed, identifying for which size of rotorcraft this dual-functioning system would be most practical.

References

- [1] “DJI matrice 100: The quadcopter for developers.” <http://www.dji.com/matrice100>, note = Accessed: 2018-03-19.
- [2] L.-W. Tsai, *Robot analysis: the mechanics of serial and parallel manipulators*. John Wiley & Sons, 1999.
- [3] NASA/JPL-Caltech, “Flying in martian skies: Nasa’s 2020 rover mission will include tiny helicopter,” May 2018.
- [4] NASA/JPL-Caltech, “Mars rover curiosity in artist’s concept, wide – nasa’s mars exploration program,” 2011.
- [5] “Robotic landing gear could enable future helicopters to take off and land almost anywhere.”
- [6] E. Petritoli, F. Leccese, and L. Ciani, “Reliability and maintenance analysis of unmanned aerial vehicles,” *Sensors*, vol. 18, no. 9, p. 3171, 2018.
- [7] D. W. Felder, “Slope landing compensator system,” Dec. 13 1977. US Patent 4,062,507.
- [8] A. Abdilla, A. Richards, and S. Burrow, “Power and endurance modelling of battery-powered rotorcraft,” in *Intelligent Robots and Systems (IROS), 2015 IEEE/RSJ International Conference on*, pp. 675–680, IEEE, 2015.
- [9] N. Tardella, “Earthbound robots today need to take flight,” Feb 2016.
- [10] G. Hunt, F. Mitzalis, T. Alhinai, P. A. Hooper, and M. Kovac, “3d printing with flying robots,” in *Robotics and Automation (ICRA), 2014 IEEE International Conference on*, pp. 4493–4499, IEEE, 2014.

- [11] “MBZIRC UAV challenge uav challenge for aerial manipulation.” <http://www.mbzirc.com/challenge/2020>, note = Accessed: 2018-03-19.
- [12] J. Stoff, *Aviation Firsts: 336 Questions and Answers*. Dover Transportation, Dover Publications, 2012. p. 20.
- [13] G. A. Mantych and E. R. Goossen, “Landing gear for a hovercraft,” July 6 2010. US Patent 7,748,486.
- [14] S. Baker, D. Soccoll, A. Postula, and M. V. Srinivasan, “Passive landing gear using coupled mechanical design,” in *Proceedings of Australasian Conference on Robotics and Automation*, pp. 1–8, 2013.
- [15] V. Manivannan, J. P. Langley, M. Costello, and M. Ruzzene, “Rotorcraft slope landings with articulated landing gear,” in *AIAA Atmospheric Flight Mechanics (AFM) Conference*, p. 5160, 2013.
- [16] D. M. Boix, K. Goh, J. McWhinnie, and D. M. Boix, “Modelling and control of helicopter robotic landing gear for uneven ground conditions,” in *Research, Education and Development of Unmanned Aerial Systems (RED-UAS), 2017 Workshop on*, pp. 60–65, IEEE, 2017.
- [17] Y. S. Sarkisov, G. A. Yashin, E. V. Tsykunov, and D. Tsetserukou, “Dronegear: A novel robotic landing gear with embedded optical torque sensors for safe multicopter landing on an uneven surface,” *IEEE Robotics and Automation Letters*, vol. 3, no. 3, pp. 1912–1917, 2018.
- [18] J. Kiefer, M. Ward, and M. Costello, “Rotorcraft hard landing mitigation using robotic landing gear,” *Journal of Dynamic Systems, Measurement, and Control*, vol. 138, no. 3, p. 031003, 2016.
- [19] H. G. Nguyen and A. B. Burmeister, “Vertical take-off-and-landing unmanned aerial vehicle system capable of landing on uneven or sloped terrain,” June 12 2018. US Patent 9,994,307.

- [20] N. K. Gentry, “Adjustable landing gear assembly for unmanned aerial vehicles,” Mar. 14 2017. US Patent 9,592,908.
- [21] L. Mühlebach, “Athlas - all-terrain helicopter landing system.” <http://athlas.ethz.ch>.
- [22] B. Stolz, T. Brödermann, E. Castiello, G. Englberger, D. Erne, J. Gasser, E. Hayoz, S. Müller, L. Muhlebach, T. Löw, *et al.*, “An adaptive landing gear for extending the operational range of helicopters,” in *2018 IEEE/RSJ International Conference on Intelligent Robots and Systems (IROS)*, pp. 1757–1763, IEEE, 2018.
- [23] X. Ding, P. Guo, K. Xu, and Y. Yu, “A review of aerial manipulation of small-scale rotorcraft unmanned robotic systems,” *Chinese Journal of Aeronautics*, 2018.
- [24] S. Kim, S. Choi, and H. J. Kim, “Aerial manipulation using a quadrotor with a two dof robotic arm,” in *Intelligent Robots and Systems (IROS), 2013 IEEE/RSJ International Conference on*, pp. 4990–4995, IEEE, 2013.
- [25] A. Jimenez-Cano, J. Martin, G. Heredia, A. Ollero, and R. Cano, “Control of an aerial robot with multi-link arm for assembly tasks,” in *2013 IEEE International Conference on Robotics and Automation*, pp. 4916–4921, IEEE, 2013.
- [26] K. Kondak, F. Huber, M. Schwarzbach, M. Laiacker, D. Sommer, M. Béjar, and A. Ollero, “Aerial manipulation robot composed of an autonomous helicopter and a 7 degrees of freedom industrial manipulator,” in *Robotics and Automation (ICRA), 2014 IEEE International Conference on*, pp. 2107–2112, IEEE, 2014.
- [27] A. Suarez, A. E. Jimenez-Cano, V. M. Vega, G. Heredia, A. Rodriguez-Castaño, and A. Ollero, “Design of a lightweight dual arm system for aerial manipulation,” *Mechatronics*, vol. 50, pp. 30–44, 2018.

- [28] C. E. Doyle, J. J. Bird, T. A. Isom, J. C. Kallman, D. F. Bareiss, D. J. Dunlop, R. J. King, J. J. Abbott, and M. A. Minor, “An avian-inspired passive mechanism for quadrotor perching,” *IEEE/ASME Transactions on Mechatronics*, vol. 18, no. 2, pp. 506–517, 2013.
- [29] S.-J. Kim, D.-Y. Lee, G.-P. Jung, and K.-J. Cho, “An origami-inspired, self-locking robotic arm that can be folded flat,” *Science Robotics*, vol. 3, no. 16, p. eaar2915, 2018.
- [30] P. E. Pounds, D. R. Bersak, and A. M. Dollar, “Grasping from the air: Hovering capture and load stability,” in *Robotics and Automation (ICRA), 2011 IEEE International Conference on*, pp. 2491–2498, IEEE, 2011.
- [31] S. Latscha, M. Kofron, A. Stroffolino, L. Davis, G. Merritt, M. Piccoli, and M. Yim, “Design of a hybrid exploration robot for air and land deployment (herald) for urban search and rescue applications,” in *Intelligent Robots and Systems (IROS 2014), 2014 IEEE/RSJ International Conference on*, pp. 1868–1873, IEEE, 2014.
- [32] J.-P. Merlet and C. Gosselin, “Parallel mechanisms and robots,” in *Springer Handbook of Robotics*, pp. 269–285, Springer, 2008.
- [33] M. Kamel, K. Alexis, and R. Siegwart, “Design and modeling of dexterous aerial manipulator,” in *Intelligent Robots and Systems (IROS), 2016 IEEE/RSJ International Conference on*, pp. 4870–4876, IEEE, 2016.
- [34] R. M. Jones, D. Sun, G. Barsi Haberfeld, A. Lakshmanan, T. Marinho, and N. Hovakimyan, “Design and control of a small aerial manipulator for indoor environments,” in *AIAA Information Systems-AIAA Infotech@ Aerospace*, p. 1374, ARC, 2017.

- [35] K. Gkountas, G. Ntekoumes, and A. Tzes, “Dynamics and control of an unmanned aerial vehicle employing a delta-manipulator,” in *Control and Automation (MED), 2017 25th Mediterranean Conference on*, pp. 1207–1212, IEEE, 2017.
- [36] J. Hodgins, *H-Delta: design and applications of a novel 5 degree of freedom parallel robot*. PhD thesis, UIT, 2018.
- [37] T. W. Danko, K. P. Chaney, and P. Y. Oh, “A parallel manipulator for mobile manipulating uavs,” in *Technologies for Practical Robot Applications (TePRA), 2015 IEEE International Conference on*, pp. 1–6, IEEE, 2015.
- [38] “Minekafon disarming mines with aerial manipulator.” <http://minekafon.org/>, note = Accessed: 2018-03-19.
- [39] Z. Pandilov and V. Dukovski, “Comparison of the characteristics between serial and parallel robots.,” *Acta Technica Corvininessis-Bulletin of Engineering*, vol. 7, no. 1, 2014.
- [40] M. Maya, E. Castillo, A. Lomelí, E. González-Galván, and A. Cárdenas, “Workspace and payload-capacity of a new reconfigurable delta parallel robot,” *International Journal of Advanced Robotic Systems*, vol. 10, no. 1, p. 56, 2013.
- [41] D. Zhang, *Parallel robotic machine tools*. Springer Science & Business Media, 2009.
- [42] S. B. Park, H. S. Kim, C. Song, and K. Kim, “Dynamics modeling of a delta-type parallel robot (isr 2013),” in *Robotics (ISR), 2013 44th International Symposium on*, pp. 1–5, IEEE, 2013.
- [43] C. Gosselin and J. Angeles, “Singularity analysis of closed-loop kinematic chains,” *IEEE transactions on robotics and automation*, vol. 6, no. 3, pp. 281–290, 1990.

- [44] Y. Cao, K. Lu, X. Li, and Y. Zang, “Accurate numerical methods for computing 2d and 3d robot workspace,” *International Journal of Advanced Robotic Systems*, vol. 8, no. 6, p. 76, 2011.
- [45] J.-P. Merlet, *Parallel robots*, vol. 128. Springer Science & Business Media, 2006.
- [46] G. Pagis, N. Bouton, S. Briot, and P. Martinet, “Enlarging parallel robot workspace through type-2 singularity crossing,” *Control Engineering Practice*, vol. 39, pp. 1–11, 2015.
- [47] “Friction between materials.” https://www.engineeringtoolbox.com/friction-coefficients-d_778.html. Accessed: 2018-04-19.
- [48] R. M. Jones, *Deformation theory of plasticity*. Bull Ridge Corporation, 2009.
- [49] J. J. Craig, *Introduction to robotics: mechanics and control*, vol. 3. Pearson/Prentice Hall Upper Saddle River, NJ, USA:, 2005.
- [50] A. Gasparetto and V. Zanotto, “A new method for smooth trajectory planning of robot manipulators,” *Mechanism and machine theory*, vol. 42, no. 4, pp. 455–471, 2007.
- [51] J. Du and Y. Lou, “Simplified dynamic model for real-time control of the delta parallel robot,” in *Information and Automation (ICIA), 2016 IEEE International Conference on*, pp. 1647–1652, IEEE, 2016.
- [52] Z. Shareef, *Path Planning and Trajectory Optimization of Delta Parallel Robot*. PhD thesis, Universitätsbibliothek, 2015.
- [53] L. Son, M. Bur, and M. Rusli, “A new concept for uav landing gear shock vibration control using pre-straining spring momentum exchange impact damper,” *Journal of Vibration and Control*, vol. 24, no. 8, pp. 1455–1468, 2018.

- [54] “PJRC teensy 3.2 microcontroller discription.” <https://www.pjrc.com/store/teensy32.html>. Accessed: 2018-03-19.
- [55] “Dynamixel ax12 motor discription.” [https://www.trossenrobotics.com/images/productdownloads/AX-12\(English\).pdf](https://www.trossenrobotics.com/images/productdownloads/AX-12(English).pdf). Accessed: 2018-03-19.
- [56] “Zipline.inc lifesaving deliveries by drone.” <http://www.flyzipline.com/>, note = Accessed: 2018-03-19.
- [57] “Google Project Wing google wing delivery drone.” <http://www.wing.com/>, note = Accessed: 2018-03-19.
- [58] D. Angell, D. Bealmear, P. Benarroche, A. Henry, R. Hudson, T. Rivellini, and A. Tolmachoff, “Lunar polar coring lander,” 1990.
- [59] C. A. Thiels, J. M. Aho, S. P. Zietlow, and D. H. Jenkins, “Use of unmanned aerial vehicles for medical product transport,” *Air medical journal*, vol. 34, no. 2, pp. 104–108, 2015.
- [60] G. Tuna, B. Nefzi, and G. Conte, “Unmanned aerial vehicle-aided communications system for disaster recovery,” *Journal of Network and Computer Applications*, vol. 41, pp. 27–36, 2014.
- [61] K. Nonami, “Prospect and recent research & development for civil use autonomous unmanned aircraft as uav and mav,” *Journal of system Design and Dynamics*, vol. 1, no. 2, pp. 120–128, 2007.
- [62] G. A. Mantych and E. R. Goossen, “Landing gear for a hovercraft,” July 6 2010. US Patent 7,748,486.
- [63] H. G. Nguyen and A. B. Burmeister, “Vertical take-off-and-landing unmanned aerial vehicle system capable of landing on uneven or sloped terrain,” June 12 2018. US Patent 9,994,307.

- [64] L. Shevenell, K. A. Connors, and C. D. Henry, “Controls on pit lake water quality at sixteen open-pit mines in nevada,” *Applied Geochemistry*, vol. 14, no. 5, pp. 669–687, 1999.
- [65] M. Huang, H. Nie, M. Zhang, X. Wei, and S. Yue, “Design of mission adaptive landing gear for near space travel lander..,” *Journal of Vibroengineering*, vol. 18, no. 8, 2016.
- [66] J. Scott and C. Scott, “Drone delivery models for healthcare,” 2017.
- [67] J. Glancey, “Failure analysis methods-what, why and how,” 2006.
- [68] G. B. Haberfeld, D. Sun, and N. Hovakimyan, “Stabilization and optimal trajectory generation for a compact aerial manipulation system with a delta-type parallel robot,” in *2018 International Conference on Unmanned Aircraft Systems (ICUAS)*, pp. 1091–1100, June 2018.

A Appendices

A.1 Schematics of Circuitry

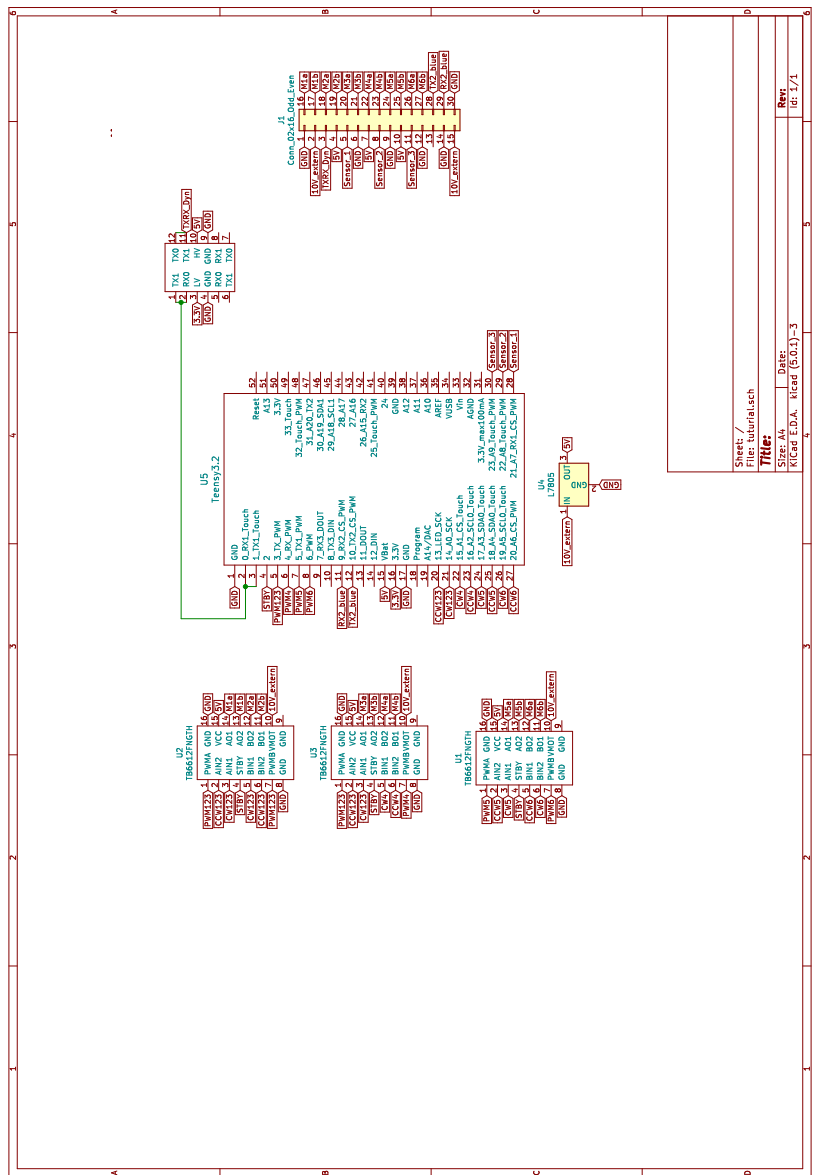


Figure 59: Electrical Hardware Architecture and Bus interfaces.

A.2 QR code to video demo of free-flight experiments



Figure 60: QR code to address of free-flight demo video “Delta Manipulander - 3DOF Manipulation and Adaptive Landing in One System” : <https://youtu.be/aWPetaxtEIE>